UNIVERSIDAD NACIONAL DE COLOMBIA

Forward volumetric modeling framework for realistic head models towards accurate EEG source localization

Ernesto Cuartas Morales

Universidad Nacional de Colombia
Facultad de Ingeniería y Arquitectura, Departamento de Ingeniería
Eléctrica, Electrónica y Computación
Manizales, Colombia

2018

Forward volumetric modeling framework for realistic head models towards accurate EEG source localization

Ghost-filling Finite Difference Anisotropic Reciprocity Method

GFDARM

Author:
Ernesto Cuartas Morales

Thesis presented as partial requirement for the degree of:
Doctor of Engineering - Automatics

Supervisor:
(Ph.D.) César Germán Castellanos Domínguez

Thesis committee:

Pedro Valdés Sosa, PhD
Cuban Neurosciences Center

María de la Iglesia Vaya, PhD
Science Director of CEIB

Dante Mantini, PhD
KU-Leuven

Research Group:
Signal processing and Recognition

Universidad Nacional de Colombia
Facultad de Ingeniería y Arquitectura, Departamento de Ingeniería Eléctrica, Electrónica y Computación
Manizales, Colombia
2018

Marco de modelado volumétrico directo para modelos de cabeza realistas enfocado hacia la localización precisa de fuentes de activacion empleando EEG

Método de Diferencias Finitas Empleando Llenado-fantasma, Reciprocidad y Anisotropía.

Author:
Ernesto Cuartas Morales

Tesis presentada como requisito parcial para optar al título de:
Doctor en Ingeniería - Automática

Tutor:
(Ph.D.) César Germán Castellanos Domínguez

Jurados:

Pedro Valdés Sosa, PhD
Centro de Neurociencias, Cuba

María de la Iglesia Vaya, PhD
Directora Científica CEIB

Dante Mantini, PhD
KU-Leuven

Grupo de Investigación:
Grupo de procesamiento digital de señales

Universidad Nacional de Colombia
Facultad de Ingeniería y Arquitectura, Departamento de Ingeniería Eléctrica, Electrónica y Computación
Manizales, Colombia

2018

A la vida, que ha permitido recorrer el camino de la ingeniería.
A Juan Pablo, que me enseñó lo que significa luchar.
A Amanda, por enseñarme el significado de la palabra amistad.
A mi padre, por ser mi maestro de vida.
A mi madre, por ser mi luz en medio de toda esta oscuridad.
A Juan Alejandro, porque sin el no habría razones para seguir escribiendo el camino.

En las orillas del tiempo buscamos los indefinido, deseamos lo perdido, añoramos lo q no hemos vivido, y lo extraño es q rara vez prestamos atención a los sutiles regalos del destino, a los amigos, a los días efímeros, a los nuevos comienzos y a las promesas ocultas q reaparecen en nuestro sendero y nos brindan las verdaderas razones para seguir recorriendo el camino...

Abstract

Synergetic effects connecting spatial and functional neuroimaging techniques allows reduction of the weakness for single method analysis. Specifically, Electroencephalographic (EEG) Source Imaging (ESI) relating structural head models and distributed source localization techniques improves the time and spatial resolution of single MRI or EEG analysis. The construction of more accurate forward models for ESI solutions, holding better precision and less computational burden is an important task for investigative purposes, but also for surgery planning and disorder treatments. In this regard, we present a novel finite-difference EEG forward problem solution that we called ghost-filling finite difference anisotropic reciprocity method (GFDARM). First, we introduce a finite difference numerical solution for the conservative form of the Poisson equation, using an asymmetric volumetric stencil, together with the transition layer technique to formulate finite differences that properly deal with the considered Newman and Dirichlet boundary conditions. Later, we formulate a solution for an irregular free-form boundary domain, based on a second-order accuracy ghost-filling approximation for the homogeneous Newman flux condition, allowing us to solve the discretized finite differences volume only for the significant potential unknowns. Then we analyze the linear equation system solution and the considerations for a reciprocity solution over the electrodes space. Further, we test our method using a multilayer spherical head model that can include anisotropy and can admit an analytical solution of the Poisson equation. Finally, we analyze a noisy linear equation system to study the numerical stability of the technique in the presence of perturbations. Our results show stability and super-linear convergence. Moreover, validation against an analytical solution shows high correspondence in the potential distribution for a wide range of dipole positions and orientations. As a final stage, we introduce a realistic patient-specific EEG forward modeling pipeline, including anisotropy in the skull and the white matter; MRI segmentation; electrode co-register; voxelwise conductivity

definitions; reciprocity space solution; and GFDARM numeric EEG forward solver. Our results using Bayesian model selection for group studies in a random fixed effect analysis show strong evidence in favor of more complex head models, including anisotropic skull and white matter modeling.

Keywords: EEG forward problem, finite differences, ghost-filling, head modeling, anisotropy, tissue conductivities, EEG source imaging (ESI), Bayesian model selection for group studies, volumetric priors.

Resumen

Los efectos conjuntos conectando técnicas espaciales y funcionales de neuro-imágen permiten el mejoramiento de las características de un solo método. Específicamente, la generación de imágenes de fuentes de activación (ESI) mediante electroencefalografía (EEG) que relaciona modelos estructurales de conductividad y técnicas de localización de fuentes distribuidas, permite un mejoramiento en la resolución espacial, conservando la resolución temporal del EEG. La construcción de modelos de conductividad más precisos, con una mayor precisión y menos carga computacional es una tarea importante para soluciones que emplean ESI, así como para fines de investigación, planificación de cirugía y/o los tratamientos de trastornos neurológicos en general. En este trabajo presentamos una nueva solución del problema directo empleando diferencias finitas, a la que llamamos método de diferencias finitas empleando llenado-fantasma, reciprocidad y anisotropía (GFDARM). Primero, nosotros presentamos una solución numérica de diferencias finitas para la forma conservativa de la ecuación de Poisson, utilizando una plantilla volumétrica asimétrica, junto con la técnica de transición de capas, para formular diferencias finitas que aborden adecuadamente las condiciones de contorno de Newman y Dirichlet. Más adelante, formulamos la solución para una frontera irregular y de forma libre basada en una aproximación de segundo orden de llenado-fantasma que permite cumplir la condición de flujo homogéneo de Newman, lo que nos permite resolver el volumen discretizado solo para las incógnitas de potencial diferentes de cero (significativas). Posteriormente se analiza la solución del sistema de ecuaciones lineales y las consideraciones para una solución de reciprocidad sobre el espacio de los electrodos. Además, realizamos pruebas utilizando un modelo de cabeza esférico multicapa que puede incluir anisotropía y del cual se puede obtener una solución analítica. Finalmente, se analiza la solución del sistema lineal de ecuaciones en presencia de ruido estudiando la estabilidad numérica de la técnica. Nuestros resultados muestran estabilidad y convergencia súper lineal y una alta correspondencia en la distribución de potenciales

para una amplia gama de posiciones y orientaciones de dipolos comparando contra una solución analítica esférica. Finalmente se una metodología para el modelado directo de EEG empleando modelos realistas y paciente-específicos, que incluye anisotropía en el cráneo y la materia blanca; segmentación de MRI; co-registro de electrodos; definiciones de conductividad voxel a voxel; solución de espacio de reciprocidad; y solución numérica del problema directo en EEG empleando GFDARM. El desempeño de la técnica y la influencia de los modelos directos realísticos son analizados empleando selección de modelos para estudios de grupos en un marco Bayesiano, los cuales muestran fuerte evidencia a favor de modelos de conductividad más complejos, que incluyan modelado anisótropo del cráneo y la materia blanca.

Palabras clave: Problema directo en EEG, diferencias finitas, llenado fantasma, modelado de la cabeza, anisotropía, conductividad de tejidos, imagenología de fuentes EEG, selección de modelos Bayesiana para estudios de grupo, priors de volúmen.

Acknowledgments

I would like to express my gratitude to the Signal Processing and Recognition Group (SPRG) at the Universidad Nacional de Colombia (Manizales) and to my thesis director German Castellanos.

Special thanks to Juan David Martinez, the knowledge about how to be a human been is priceless, and I learned a lot about this topic with him. Yohan Cespedes, who always stayed on the boat, even when the water tried to sink it. Diego Gonzales, AKA Keko, because real friendship is the most important and difficult thing to find in life. To my family and Verónica, thanks for always been there.

Furthermore, thanks to all the members of the Medical Image Analysis and Biometry Lab, Universidad Rey Juan Carlos, Madrid, Spain. Movement Control & Neuroplasticity Research Group, KU-Leuven, Belgium. Institute for Biomagnetism and Biosignalanalysis (IBB), University of Munster, Germany. Computer Science Technology TC, Bruges Campus.

This research is supported by *Desarrollo de un sistema de soporte diagnóstico y detección temprana de la enfermedad de alzheimer basado en medidas de conectividad funcional a partir de registros electroencefalográficos en estado de reposo*, Proyecto de investigación para la convocatoria 744. Ciencia, Tecnología e Innovación y su contribución a los retos del país - 2016.

This work was carried out under grants: *Programa Nacional de Formación de Investigadores Generación del Bicentenario, 2012*, Convocatoria 528.

Contents

List of Figures

List of Tables

Notation

Variables and Functions

ϕ	Potential
$\boldsymbol{J}$	Current density
$\boldsymbol{\iota}$	Current dipole source
I_m	Dipole current magnitud
$\mathbf{d}$	Dipole moment
r^+	Dipole source position
r^-	Dipole sink position
Ω	Head volume
$\tilde{\Omega}$	Fictitious domain
$\partial\Omega$	Head volume boundary
Γ	Head tissue interface
$\boldsymbol{\Sigma}$	Conductivity tensor
σ	Conductivity tensor entry
$\boldsymbol{r}$	Spatial position
S_j	FDM Stencil
$\boldsymbol{A}$	System or Coefficient matrix
$\boldsymbol{L}$	Leadfield matrix
R	Eingenvectors
λ	Eingenvalue
α	FDM coefficient
h	Discretization step size
ε	Minimum relative residual
C	Conditional number
η	Noise power

ξ	Uniform distribution noise
s_j	DTI to conductivity map scaling factor
$\boldsymbol{D}$	DTI tensor
$\boldsymbol{Y}$	EEG dataset
$\boldsymbol{\Xi}$	Covariance matrix
$\boldsymbol{Q}$	Prior information matrix

Mathematical Operators

$\delta(\cdot)$	Dirac function
$\|\cdot\|$	Norm

Abbreviations

AMG	Algebraic Multigrid
AR	Anisotropy ratio
BEM	Boundary Finite Elements
BiCG-Stab	biconjugate gradient stabilized solver
BMS	Bayesian model selection
CG	Conjugate Gradient
CSF	Cerebrum Spinal Fluid
CT	Computed Tomography
DLE	Dipole localization error
DOE	Dipole orientation error
DTI	Diffusion tensor imaging
DWI	Diffusion Weighted Imaging
EA	Ensemble averaging
EBB	Empirical Bayesian Beamformer
EPSP	Excitatory Post-Synaptic Potentials
ERP	Event related potentials
EEG	Electro EncephaloGraphy
ESI	EEG Source Imaging

FA	Fractional anisotropy
FD	Fictitious domain
FDM	Finite Difference Method
FEM	Finite Elements Method
FJ	Furier-Jacoby Matrix
fMRI	Functional Magnetic Resonance Imaging
GFD	Ghost filling domain
GFDARM	*Ghost-filling* finite difference anisotropic reciprocity mehtod
GM	Grey Matter
hdEEG	High density EEG
iLU	incomplete iLU factorization
IPSP	Inhibitory Post-Synaptic Potentials
LES	Linear Equation Systems
LOR	Loreta
LU	LU factorization
MAG	Magnitude measure
MEG	Magneto EncephaloGraphy
MRI	Magnetic resonance imaging
MSP	Multiple sparse priors
NCS	Numerical solver combinations
NYM	New York head model
PET	Positron Emission Tomography
RDM	Relative difference measure
RHM	Realisitc head model
RRE	Relative residual error
SOR	Successive Over Relaxation
SPECT	Single Photon Emission Tomography
WM	White Matter

Chapter 1

Preliminaries

1.1 Introduction

The human brain mapping is described today as the new frontier of knowledge for the mankind [Brain Initiative Working Group, 2014]. There are several methodologies for analyzing and monitoring the human brain structure and function at a higher level of detail in every new generation of devices [Ramon et al., 2011, Lantz et al., 2011, Wendel et al., 2009]. These details allow better results in medical treatment, surgery planning or, more generally, brain research. The brain structural image techniques improve from the energy invasive computed tomography (CT) to non-invasive analysis like magnetic resonance imaging (MRI). Moreover, functional analysis techniques such ElectroEncephaloGraphy (EEG), MagnetoEncephaloGraphy (MEG), Positron Emission Tomography (PET), Single Photon Emission Tomography (SPECT), or functional Magnetic Resonance Imaging (fMRI) provide information about the activation zones of the brain in time sequences. Single structural-based analysis of brain functionality (fMRI) has a good spatial resolution but poor time analysis windows. The synergetic effects connecting spatial and functional analysis techniques allows reduction of the weakness for single technique analysis [Grech et al., 2008]. Specifically, EEG Source Imaging (ESI) connecting structural head models and distributed source localization techniques improves the time and spatial resolution of single MRI or EEG analysis [Michel et al., 2004]. ESI information is used for diagnosis and preoperative stages of brain surgery being, in most cases, the only suitable analysis tools because of the high risk of surgical interventions [Martinez et al., 2017, Voges et al., 2011, Titto et al., 2004, Waberski et al., 2000].

The electroencephalography (EEG) measures the electrode potentials at the scalp of the human head over a period of time. Those potentials are generated by electrical activity inside the brain. One neuron generates a small amount of electrical activity in the order of femtom Ampere. This small amount of energy cannot be measured by electrodes placed on the scalp surface, however, when a large group of neurons (approximately 1e6) is simultaneously active, the electrical activity is large enough to be picked up by the electrodes at the scalp generating a meaningful EEG signal [Herculano, 2009]. The electrical activity of a group of neurons can be modeled as a current dipole that is the precursor a potential field inside the volume conductor human head [Hallez et al., 2007b].

The potentials over the scalp surface, the dipole sources, and the conductivity volume involve the solution of two different problems: *i*) The forward problem calculates the potential of the electrodes on the scalp for a given source configuration [Hallez et al., 2007b]. *ii*) The inverse problem, estimates the source parameters from the potential of the electrodes [Grech et al., 2008]. The solution of the inverse problem or source localization of neuronal activity from EEG/MEG is a useful tool in both pathology identification and brain surgery planning, providing crucial information for patients who suffer neuronal disorders such as Parkinson's or epilepsy [Shackleton D et al., 2003]. Distributed source localization techniques require not only the EEG data but also detailed information about geometry and physical properties of the head tissues that are interposed between the sources and the sensors, namely, the solution of the forward problem. There are several methodologies that solve the forward problem, each one having its own advantages and weaknesses depending on the necessities of the considered task. The most used methodologies are: spherical models [De Munck et al., 1993], Boundary Finite Elements (BEM) [Hallez et al., 2007b], Finite Elements Method (FEM) [Wolters, 2003], and Finite Difference Method (FDM) [Hallez, 2009].

The solution of the forward problem in EEG source analysis involves the solution of Poisson's equation for a multilayer conductor volume, taking into account proper boundary conditions [Haueisen et al., 1997, Lin et al., 2006]. The Neumann condition (or flux condition) states that all charges leaving one compartment through a boundary interface must enter the other compartment. In particular, no current can be injected into the air outside the human head due to the very low conductivity of the air, this meaning that the current flux outside the head is null (Neumann homogeneous condition). The Dirichlet boundary condition states that the potential cannot have

discontinuities when crossing a boundary. This condition only holds for interfaces not connected with air [Hallez et al., 2007b].

The spherical head model is the simplest approach to solve the propagation Poisson equation [De Munck et al., 1993]. For this model, the different tissues conforming the head are modeled as concentric spheres, where every tissue (scalp, skull, gray matter, white matter among others) has its own conductivity value, being the scalp the outer sphere that contains the EEG electrodes. The high symmetry of this type of models allows analytical solutions [De Munck et al., 1993], however, several authors shows that the simplifying spherical head model induces source localization errors bigger than $30mm$ due to the strong simplification of the realistic and irregular shape of the human head [Hallez et al., 2008, Henson et al., 2009]. The spherical head modeling is a useful tool for general analysis, but, when the accuracy is an important factor (like in surgery planing) more realistic approaches are needed [Pai et al., 2005, Wang et al., 2008, Palagan et al., 2011, Vorwerk et al., 2014].

The solution of the Poisson equation for realistic free-form head volumes is only possible using numerical approximations [Irimia et al., 2013]. A realistic head volume can be obtained from neuroimages such MRI or CT containing a large number of slices in a series of two-dimensional images. Every slice must be registered in the same coordinate system in order to obtain a coherent three-dimensional volume [Vallagh et al., 2007]. After the registration stage, the volume contains the information of the head with different tissues codified in intensity values [Whalen et al., 2008]. The tissues can be segmented from this kind of data. In particular, the scalp (where the EEG electrodes are placed), the skull, the cerebrum spinal fluid, the gray matter and the white matter, are the most commonly considered tissues in forward modeling. However, several tissues like eyes, fat, muscle, hard bone and soft bone (among others) can be considered for the segmentation stage in order to obtain more realistic/accurate head models [Irimia et al., 2013]. Denoising and post-preprocessing stages are commonly needed for good segmentation results. Nowadays there are a set of open-use toolboxes that handle the image processing and segmentation stages with very good results (SPM [Karl et al., 2007], FSL [Jenkinson et al., 2012], FreeSurfer [Laboratory for Computational Neuroimaging and technology, 2013]) [Vorwerk et al., 2014].

After segmentation, the volume data contains labeled information about the different tissues. This data is used to construct the realistic head model using knowing conductivity parameters for each tissue [Michel et al., 2016]. The most simplify numeric

solution from structural real data is the BEM method [Ferguson et al., 1997]. This solution can be obtained calculating the potentials for self-contained tesselated surface shells representing the interfaces between two different tissues, induced by a given dipole source. BEM method is widely used because of its low computational needs, however, most solutions only consider three surface boundaries (scalp, skull, and brain), and is restricted only to isotropic conductivities. Nevertheless, several works analyze the influence of neglecting the human head anisotropy tissues in the ESI solutions [Cuartas et al., 2017b, Montes et al., 2016, Ziegler et al., 2014, Wendel et al., 2009, Wolters et al., 2006]. Specific works like [Hallez et al., 2005] found dipole localization errors larger than $20mm$ for spherical head models solved with numerical techniques that neglects the anisotropy of white matter and skull conductivities. Also in [Wolters et al., 2006] found that the influence of anisotropic skull is very strong even in cortical sources for ESI solutions, showing also that anisotropic white matter influence is very strong in deep source analysis. Other works conclude that the influence of cerebrum spinal fluid (CSF) in the conduction of the potential from the pyramidal cells to the scalp is crucial (due to the high conductivity factor of this fluid), and only the realistic volumetric techniques can properly model the CSF tissue propagation influence [Strobbe et al., 2014a, Lanfer et al., 2012, Dannhauer et al., 2011]. Particularly there are two decisive factors that expose the need for volumetric and realistic forward models, the first one is the strong anisotropic behaviour of the skull and white matter (among others tissues like the thalamic areas) due to the direct impact on EEG source localization accuracy, and, the patient-specific analysis with multiple tissues definition that drastically reduce the errors of using spherical approximations or general atlas [Vorwerk et al., 2014, Vallagh et al., 2007].

There are two main methodologies that can handle anisotropic conductivity and realistic patient-specific analysis, the Finite Element Method (FEM) [Wolters et al., 2002, Liu et al., 2005], and the Finite Difference Method (FDM) [Vanrumste et al., 2001b, Hallez, 2009]. The main practical problem of FEM and FDM in comparison with BEM is the computational burden. BEM solutions are calculated on the boundaries between homogeneous isotropic compartments while in FEM and FDM the solution of the forward problem is calculated in the entire volume [Vanrumste et al., 1998]. With BEM technique, the solution leads to a linear system that generally can be solved using direct matrix inversion without taking into account a system excitation (source), due to this, only a matrix calculation is needed to obtain the scalp potentials. In FEM and FDM the solution leads also to linear systems,

but the coefficient matrix is typically sparse and has a large number of unknowns in comparison with BEM. Thus, a direct matrix inversion is not the best way to solve the problem using volumetric techniques, this due to the dimension of the coefficient matrix [Petersen et al., 2012]. This large coefficient matrix systems can be resolved for a given right-hand side term (source excitation) leading to linear equation systems (LES) that can be solved using iterative solutions such as the successive over-relaxation method (SOR), the conjugate gradient methods (CG), or algebraic multigrid methods (AMG) [Wolters et al., 2006, Mohr et al., 2003].

Significant progress has been made in the EEG forward solution FEM-based techniques in order to reduce the computational time and improve the accuracy of the models. Such techniques are the subtraction, partial integration, or the Venant approaches, being the last, one of the most computational efficient FEM methodologies [Dannhauer et al., 2011]. This approach uses hexahedral deformable elements instead of the commonly tetrahedral voxels. For the LES, they used the incomplete-Cholesky preconditioned conjugate gradient in a reciprocity approach. This setup allows fast forward calculations, but, in comparison with BEM, the computational time is still a major issue.

The main difference between FDM and FEM techniques is that FEM uses an adaptative grid with arbitrary/adjustable node positions, in this way, FEM solutions are very versatile, and in theory, one can adjust their reconstruction accuracy and computational demands by varying the mesh resolution locally. In contrast, FDM's partition the volume into a uniform voxel grid and this seems like a big disadvantage, especially for complex boundaries morphologies, however, the developing in neuroimaging techniques such MRI have reached a point where higher spatial resolutions are possible. Thus, nowadays, $0.5mm^3$ or even more detailed voxel resolutions are possible. In this sense, a fundamental advantage of FDM's as compared to FEM's is its straightforward integration with structural imaging data (CT/MR), which are always acquired in regular tri-dimensional grids [Huang et al., 2016]. This makes FDM's intrinsically suitable for modeling across voxels differences in conductivity and anisotropy, without the need of defining tissue compartments with homogenous physical properties. On the other hand, FEM commonly needs a tesselation stage to build the nonregular grid, and also complex and more expensive numerical approximations due to its non-regular grid nature. However, in comparison with FEM, there is not a significant effort in the bibliography to improve the computational time and accuracy of the EEG forward solution FDM-based techniques. [Mohr et al., 2003]

analyses four different solvers (SOR, CG, AMG and a variation of CG) and conclude that the best solution yields with the algebraic multigrid solver, nevertheless, most solutions use the stationary SOR solver algorithm [Hallez, 2009], suggesting that fast and stable FDM solutions are still an open issue [Salman et al., 2016].

Solving the EEG forward problem with volumetric solvers (FEM and FDM) involves the calculation of the potentials for a high number of unknowns, as a consequence, for a $1mm^3$ voxel resolution in a realistic head model, the squared coefficient matrix can holds more than 8 million of rows. The coefficient matrix must be solved for a single source position/orientation in a linear equation system (LES), however, for an ESI solution, several source positions must be considered (typically, more than 1 thousand [Huang et al., 2016]). Thus, for the simplest ESI distributed estimation, at least 1 thousand LES forward calculations are needed. Indeed, this is not a practical scenario, because of the time spent to calculate a large number of forward approximations. Nevertheless, considering that the distributed ESI solutions requires only the potentials in the EEG scalp electrodes (not in the entire volume) produced by every single dipole current source under consideration (*lead-field* matrix), and taking into account that the number of electrodes is in general small compared with the number of sources, a current to potentials transformation for the electrode space can be applied, exchanging the number of forward calculations over the number of electrodes instead of the number of sources. This is called, the reciprocity approach, where a current/potential transformation is used allowing to induce a current dipole in one pair of electrodes [Rush et al., 1969]. Thus, for an EEG with N_E electrode positions over the scalp, there is $N_E - 1$ electrode pairs that can be found with linear independent potential differences (*lead-pairs*). Therefore, only N_E-1 forward calculations are needed to find the potentials in the electrode-scalp positions for every given arbitrary source position/orientation contained inside the volume conductor medium. Lastly, the N_E-1 electrode pairs are transformed in N_E average referenced potentials at the electrodes positions [Vanrumste et al., 2001b]. The reciprocity has been widely used solving the forward problem [Hallez et al., 2007b, Malmivuo et al., 1995]. The electrode pairs are called *lead-pairs* and the relationship matrix between the electrodes and a set of given source positions is called the *lead-field* matrix $L \in \mathbb{R}^{N_E \times N_D}$, where N_D is the number of considered dipoles [Grech et al., 2008]. Furthermore, a pre-computed *lead-pair* space allows the direct calculation of the EEG potentials produced for every current dipole position/orientation speeding up the calculation of the *lead-field* matrix.

The reciprocal approaches have been widely used in BEM, FEM and FDM

techniques [Ziegler et al., 2014, Vanrumste et al., 2001b, Duraiswami et al., 1998], but, the complexity and the solution involving large sparse matrices in FEM and FDM techniques in comparison with the direct solution of BEM is an important practical issue, this due to the amount of computational time required for the complex volumetric solvers.

The real advantage of the volumetric techniques (FEM and FDM) resides not only in the accuracy of the model, but also that the holistic techniques nowadays commonly include anisotropic conductivities [Hallez et al., 2009]. In an isotropic conductivity medium, the measures are equal in every direction, but, for an anisotropic medium, this is not the case. The isotropic conductivity values of the human head can be represented as a positive scalar, but, for an anisotropic medium, a tensor definition is introduced. One of the best ways to describe the anisotropic behavior of a conductivity medium is using an ellipsoid. Thus, when the shape is a sphere, the medium has equal conductivity in all directions (isotropic), but, when the semi-axial distances are different, the shape differs from a sphere an becomes an ellipsoid where the conductivity measure depends on the direction. The anisotropic behavior can be modeled using a 3D symmetric tensor representing an eigenspace that holds a eigenvalues matrix representing the deformation magnitude for the principal orthogonal axes, and the eigenvectors matrix representing a local rotational transformation. Therefore, using conductivity tensors, it is possible to include the anisotropic conductivity behavior of the head tissues, where the largest eigenvalue represents the magnitude of the principal anisotropic direction of the medium, given by its correspondence eigenvector [Hallez et al., 2007b].

There are two highly anisotropic tissues in the human head: the skull and the white matter [Wolters et al., 2006]. The human skull is not a single layer compartment, there are at least two types tissues in it, a hard bone tissue with low conductivity and a spongy bone tissue with a larger conductivity factor [Montes et al., 2016, Marin et al., 1998, Pohlmeier et al., 1997]. Recent works show that the skull is anisotropic when is modeled as a single compartment, but, if the spongy and hard bone areas are correctly segmented from neuroimages, the three-layered isotropic skull has a similar potential propagation behavior compared against a single anisotropic layer skull [Dannhauer et al., 2011, Cuartas et al., 2014b]. Nowadays, there are two main different approaches for the realistic definition of the human skull and the influence in the source localization problem, the three shells skull with hard and spongy bone defined as single isotropic mediums [Vorwerk et al., 2014], and, the one layered skull representation with strong anisotropic behavior [Bashar et al., 2008b]. The first approach requires

high-quality segmentations or prior knowledge of the skull geometry in order to successfully segment the two different skull tissues. The second approach requires less effort in the segmentation stage, defining the skull as single layered anisotropic tissue, being the tangential direction to the skull surface the principal eigenvector with the largest eigenvalue of the conductivity tensor. The last works in the area show that both approaches generate similar dipole localization errors, but, conclude that the commonly used skull anisotropic *tangential:radial* ratio $1:10$ [Marin et al., 1998] is to big and propose lower ratios ($1:1.82$) [Lanfer et al., 2012, Montes et al., 2013]. The impact of the anisotropic skull variations with the FDM technique applied to ESI solutions is still an open issue [Lanfer et al., 2012].

Furthermore, the white matter (WM) has a strong anisotropic behavior, but, in contrast with the skull, the principal conductivity eigenvectors in the WM are not oriented among the tissue morphology. The anisotropic distribution of the WM is generated for the tract fibers composing the tissue. Early tests show that the conductivity along the tract direction can be 9 times larger compared with a perpendicular direction [Geddes et al., 1967, Nicholson, 1965]. Therefore, assuming that the diffusion weighted imaging (DWI) that measures the mobility of the water molecules in the soft tissues share eigenvectors with the anisotropic conductivity in the WM [Basser et al., 1994], the WM anisotropy can be estimated from DWI registers [Bashar et al., 2008a, Bashar et al., 2008c]. After denoising and registration stages, the DWI data contains the direction of the nerve fibers in the brain, this data is used to define constant ratios of anisotropy in the WM tissue. The variational ratio of anisotropy in the white matter was studied in [Hallez et al., 2007a], but the impact in the ESI solutions using FDM techniques is not clearly studied, thus, further analysis are necessary to conclude about the best definition for the anisotropic conductivity in the WM tissue [Vorwerk et al., 2014, Hallez et al., 2007a, Wolters et al., 2006].

Moreover, ESI influence of volumetric techniques with diverse tissue definition is an open issue nowadays [Vallagh et al., 2007]. In [Irimia et al., 2012, Irimia et al., 2013] they model a brain injury with 25 different tissue conductivities and analyze the impact in the EEG source localization problem for a single patient study. Similarly, in [Fiederer et al., 2016] analyze the role of blood vessels in the EEG volume conductor head modeling.

The construction of more accurate forward models with better precision, and less computational burden is an important task for investigative purposes, but also for surgery planing and disorder treatments [Martinez et al., 2017, Huang et al., 2016,

Salman et al., 2016, Vorwerk et al., 2014, Ramon et al., 2011].

This work is devoted to the development of an efficient and numerical stable FDM volumetric framework to solve the EEG forward problem in realistic head data from neuroimages that can handle voxelwise anisotropic definitions, aiming to improve the ESI accuracy but also reducing the computational burden of the technique.

1.2 Objectives

1.2.1 General Objective

To develop an efficient and numerical stable FDM volumetric framework to solve the EEG forward problem in realistic head data from neuroimages, that can handle voxelwise anisotropic definitions, aiming to improve the EEG source localization accuracy.

1.2.2 Specific Objectives

- To develop a suitable EEG forward solution framework, taking into account stability, and convergence, of the sparse linear system applied in a reciprocal solution aiming towards computational time reduction, while preserving model accuracy.
- To develop a conductivity head model framework extracted from neuroimages, taking into account the anisotropic behaviour of concrete tissues (namely, skull and white matter) employing finite difference volumetric techniques.
- To develop a framework to analyze the influence of the forward modelling in the EEG source localization task, taking into account the anisotropic behaviour of concrete tissues (namely, skull and white matter).

1.3 Outline

The present work can be read as follows: In Chapter 2 an overview of the EEG forward problem is presented, including the most widely used forward solution techniques. Chapter 3 is devoted to the formulation, and testing of the proposed GFDARM to solve the EEG forward problem. Chapter 4 show the forward volumetric modeling

considerations for realistic head data. Finally, in Chapter 5, a framework to analyze the influence of the forward modelling in the EEG source localization task is presented, considering anisotropy and patient dependent structural data.

In Chapter 2, we discuss the precursors of the EEG, from the brain function to the cellular potential generators level, showing the pyramidal cells activation, and its regular oriented distribution respect to the cortex surface, generating significant potentials when present synchronous activations. From the physiological overview, we pass to the mathematical Poisson formulation of the forward problem including the important boundary conditions. Then, we analyze the macroscopic dipole current and its mathematical formulation. Later, we explained the anisotropic behaviour defining the conductivity tensor. Next, we introduce the generalized inhomogeneous anisotropic medium Poisson equation in the conservative form, moving to the available forward solutions. namely, the analytical spherical multi-layer solution, and the numerical solutions for realistic head models, including the boundary element method (BEM), and the finite element method (FEM). Additionally, we perform a comparison between the proposed GFDARM numerical solution and the available BEM and FEM solutions, against analytical spherical multilayer head models, including similarity metrics and computational considerations.

In Chapter 3, we present a novel finite difference EEG forward problem solution that we called ghost-filling finite difference anisotropic reciprocity method (GFDARM). First, we present the finite difference numerical solution for the conservative form of the Poisson equation, using an asymmetric volumetric stencil, together with the transition layer technique to formulate finite differences that properly deal with the considered Newman and Dirichlet boundary conditions. Later, we introduce the FDM discrete mathematical current dipole and formulate the solution for an irregular free-form boundary based on a second-order accuracy ghost-filling approximation for the homogeneous Newman flux condition, allowing us to solve the discretized volume only for the significant potential unknowns. Then we discuss the linear equation system solution and the considerations for a reciprocity solution over the electrodes space. Further, we test our method using a multilayer spherical head model that can include anisotropy. Finally, we analyze a noisy linear equation system to study the numerical stability of the technique in presence of perturbations. Our results show stability and superlinear convergence, moreover, validation against an analytical solution show high correspondence in the potential distribution for a wide range of dipole positions and orientations.

In Chapter 4, we present a framework to perform forward volumetric modeling using the GFDARM technique, in realistic patient-specific head data from neuroimages, including anisotropy for the skull and white matter. First, we describe how to obtain realistic forward head models from neuroimages, considering tissue conductivities, MRI and DWI acquisition and registration, and interpolation to $1mm^3$ cubic voxels space. Then, we describe the considered segmentation using existing tools. Further, we detailed describe the anisotropic modeling for the skull, based in the normals estimation form the skull compartment meshing, and a following iterative propagation process to obtain eigenvectors in every single voxel for the skull tissue. Also, we describe the WM anisotropy modeling based in DWI to DTI registers, where we use a tensor scaling, taking into account both, the eigenvectors and eigenvalues from the DTI local tensors. Later, we briefly explain the electrodes space registration based on fiducial markers and introduce the parametric inverse solution to compared two forward model in the source space. We also illustrate the realistic patient-specific EEG Forward modeling pipeline, including anisotropy in the skull and the white matter; MRI segmentation; electrode coregister; voxelwise conductivity definitions; reciprocity space solution; and GFDARM numeric EEG forward solver. Our results show a significant impact on the potentials propagation and dipole source estimation using parametric inverse solution for anisotropic realistic head models.

Chapter 5 is devoted to introducing a Bayesian framework to measure the forward modeling influence in the EEG source imaging (ESI)task. First, we present an overview of the ESI approach, and the benefits of the improved spatial resolution using structural head data, and high temporal resolution of the EEG signals. We also show an overview of event-related potentials (ERP) and the importance of the source space in the ESI task. Furthermore, we introduce our own volumetric source space and priors, based in the techniques reported in the literature. For our solution, we used normals from GM and Wm meshes to estimate the normal cortex directions in the GM, that are needed to estimate the dipole moments in the source priors, in addition, we calculate the spatial relation of the considered source space for a volumetric regular grid. This information can be used to estimate volumetric source priors spaces, that are needed to distributed ESI solutions. Later, we present the three used ESI techniques in the Bayesian approach and introduce the verisimilitude free energy cost function, that can be used to perform Bayesian model selection for group studies and random effect analysis, allowing us to estimate the best forward model for a specific group of signals/patients. Our results show solid evidence in favor of more complex head models, including anisotropic skull

and white matter modeling. As a final test, we analyze the influence of the forward models in a demographic group, using generic data, population-dependent atlas, and patient-specific structural head data. Results show substantial evidence in favor of patient-specific head data, and population dependent atlas. As a final remark, we show volumetric activation maps for specific ERP's experiments. This maps are possible due to the volumetric priors approach, and can directly compare against functional neuroimage technique such as fMRI.

Finally, general conclusions and main contributions of this research work are presented in Chapter 6.

Chapter 2

The EEG forward problem

Forward modelling is an essential task for source localization techniques employing electro-encephalography (EEG) [Phillips et al., 2002]. The goal of the forward modelling is to build conductivity volumes of the human head that can be used to estimate the propagation of electric neural activity from the brain cortex. General brain study, disorder diagnosis and treatment, and especially surgery planning in disorders such as Epilepsy or Parkinson, expose the necessity of highly accurate source localization techniques that employ patient specific forward models [Martinez et al., 2017, Cuartas et al., 2017a, Vorwerk et al., 2014].

2.1 The human brain

The human brain is contained inside the human head within several tissue layers as an encapsulated medium. In general, the scalp is the outmost region of the head, and we can usually find fat, muscle, and the skull (among others minor tissues) surrounding the brain. Inside the skull, we find the dura matter, the cerebrospinal fluid (CSF) and the main tissues conforming the brain. Furthermore, the human brain can be divided into three differentiable tissues: grey matter (GM), white matter (WM), and ventricles.

Figure 2.1 show the different layers conforming the human head, where the outmost layer of the brain is the cerebral cortex (grey matter). Particularly, this tissue has a folded structure increasing the surface area and allowing complex connections. Likewise, the white matter that is contained and surrounded by gray matter mainly consists of tract fibers allowing the information transfer between separated areas in the brain. An example connection contained in the white matter is the corpus callosum which

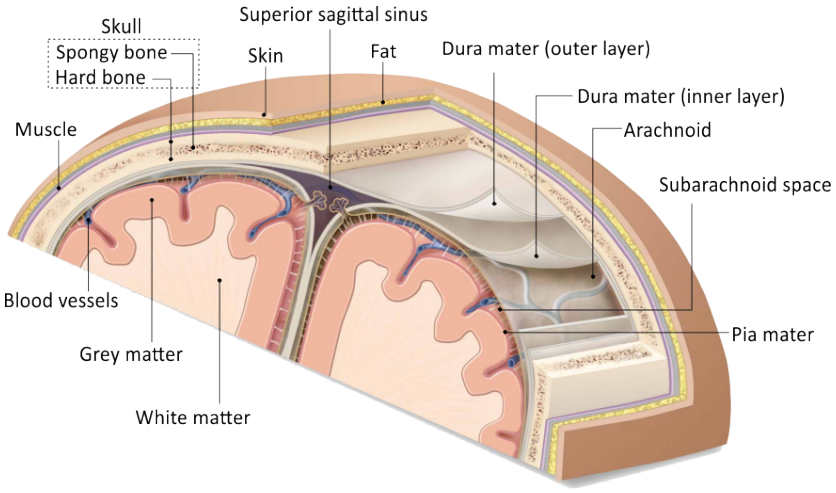

Figure 2.1: Distribution of layered-tissues conforming the human head.

connects both hemispheres of the brain. Cerebral cortex or grey matter represents over 80% of brain mass, containing 10^{10} neurons and 10 times more glial cells (10^{11}) [Herculano, 2009].

The main brain function is the information processing and transfer between different parts of the human body or between regions of the same brain. This communication mechanism takes place mainly in the gray matter tissue that contains neurons or nerve cells biological designed to process and transmit signals from other neurons or tissues (muscles or organs) generating small amounts of electro-chemical activity in the process [Baillet et al., 2001].

The brain can be divided into specific zones that are specialized to process information or cause responses for a specific function. Furthermore, there are large clusters of neurons working closely together to control particular functions of the human body. Figure 2.2 show a sagittal view with the main regions of the human brain highlighted in colors, these areas are the frontal lobe, temporal lobe, parietal lobe, occipital lobe, and the cerebellum, that is in charge of the coordination function. Figure 2.2 also show functional areas where the brain process the smells, sounds, touch, taste, and vision, with other zones specialized to process functions associated to face recognition, spatial awareness, motor control, speech, and planning or solving problems [Stevenson et al., 2014]. However, nowadays we know that in case losing the functionality of an area (due to a cerebrovascular accident, or some other incident), the brain is capable of changing or adopting separate zones for different functions. This

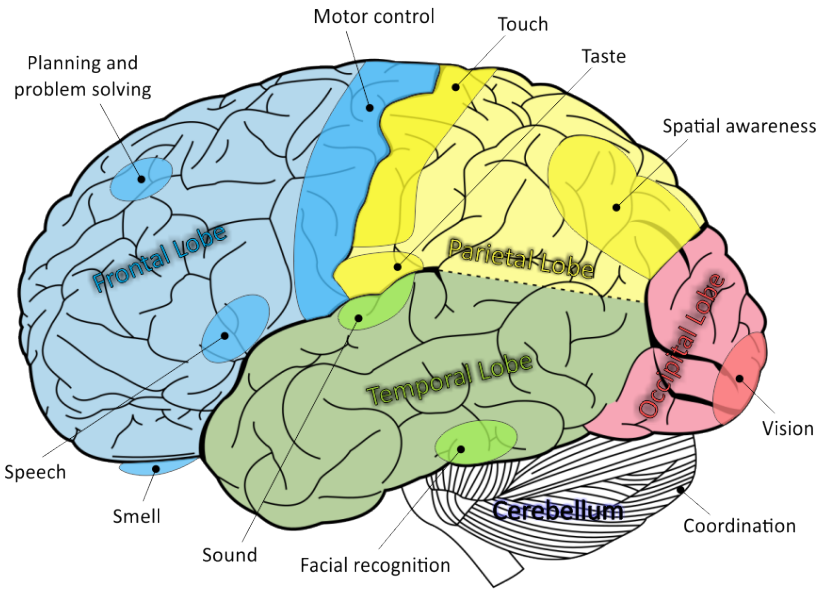

Figure 2.2: Brain structures and function areas. Figure adapted from [Henry et al., 1918] public licensee.

process is known as plasticity and is not fully understood today [Liu et al., 2017].

2.1.1 From neural activity to electrical potentials on the scalp

Neuronal intracellular environment is polarized with a resting potential around -70 mV compared with the extracellular region. From this rest state, a neuron can receive two types of signals: excitatory or inhibitory. Excitatory post-synaptic potentials (EPSP) depolarize the neuron decreasing the potential difference needed to activate the neuron. In a similar way, a neuron can receive inhibitory postsynaptic potentials (IPSP) hyperpolarizing the neuron and increasing the potential difference needed for activation. Several EPSP or IPSP signals come together to a receptor neuron at the same time (temporal summation) or in the same region (spatial summation), generating a proportional potential difference that can trigger the activation of the neuron. Neurons excited by an activation potential will secrete a chemical substance called a neurotransmitter, at the synaptic side. Furthermore, the transmission of information signals is generated by those chemical reactions producing an electrical response.

Figure 2.3 shows a typical pyramidal neuron activation, including cell's parts where

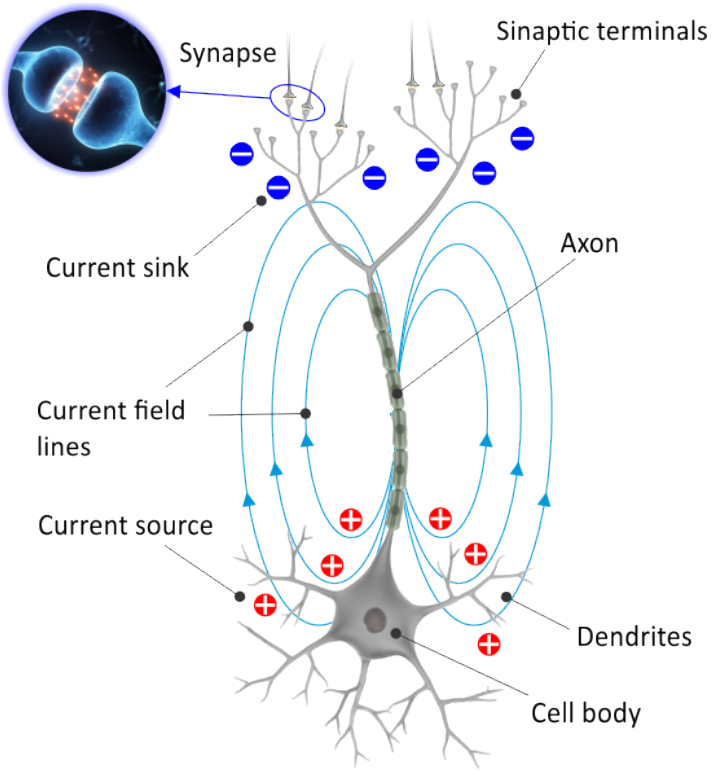

Figure 2.3: The neuron. Synapse electro-quimical signals are sent through the dendrites towards the cell body causing an activation potential that is transmitted through the axons to other neurons or to muscles.

the cell nucleus side of the neuron has positive charges, while the post axion side of the cell including the synaptic terminals has negative charges. This potential difference acts as a tiny current dipole, with a source (positive side) and a sink (negative side) current generators, thus, a current dipole oriented from the cell nucleus towards the post axion part of the cell generate an electric potential field with equipotential lines surrounding the dipole current. One neuron generates a small amount of current activity with magnitudes in the order of Femtoamperes ($10^{-15} Amp$). However, this small amount of energy cannot be picked up by electrodes placed on the scalp surface. Nevertheless, when a large group of neurons (around 10^6) is simultaneously active, the electrical field generated by this significant number of synchronous neuron activations is large enough to be picked up by the electrodes at the head scalp surface, thus generating a significant electric signal [Hallez et al., 2007b, Michel et al., 2004].

Brain function electrical signals origins in the brain cortex, where large clusters

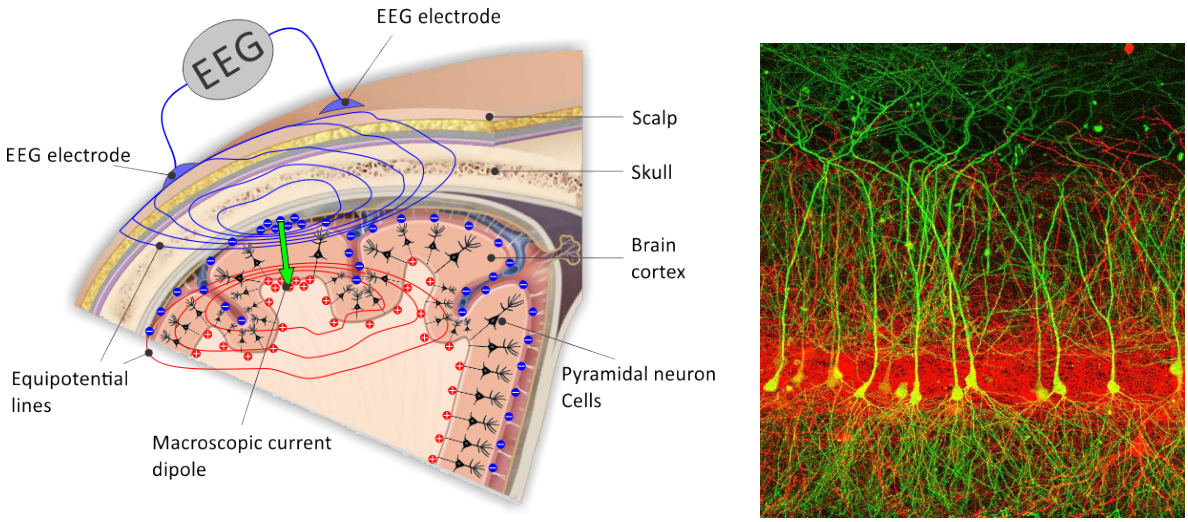

(a) (b)

Figure 2.4: Pyramidal cells array. Figure 2.4(a) ilustrate a macroscopic dipole current with normal orientation respect to the cortex surface. Current dipole direction is shown with a green arrow, and equipotential lines are shown with blue lines. Figure 2.4(b) show a mouse pyramidal neurons cluster in the hippocampal area CA1 acquired using large volume array tomography. Figure adapted from [Bloss et al., 2016] public licensee $(CC - BY - 2.5)$.

of pyramidal neuron cells are regularly oriented in the normal direction of the gray matter surface producing an additive effect of the extracellular potential fields. The electric field generated by a large cluster of pyramidal neurons can be represented as the potential induced by an equivalent macroscopic current dipole. Figure, 2.4(a) show a macroscopic dipole current with equipotential lines propagating from the dipole through the different tissues of the head, reaching the scalp where the EEG electrodes are placed. In this figure, we represent the equipotential lines deformations due to the conductivity medium, thus, the energy propagation from the dipole to the scalp generating the EEG signal is greatly influenced by the properties of the tissue conductivities in the human head. Moreover, we also show a cut-off of the potential field in the scalp-air boundary representing the very low conductivity of the air. Figure 2.4(b) show a hippocampus CA1 zone image of a mouse brain acquired using large volume array tomography and a transmission electron microscopy with a quenched native fluorescence preparation. The figure shows a cluster of parallel pyramidal neuron cells oriented perpendicular to the

cortical surface.

Electroencephalography (EEG)

First findings of electrical phenomena of exposed cerebral hemispheres of rabbits and monkeys were presented in 1875, and first human EEG recording was obtained by Hans Berger back in 1924 [Malmivuo et al., 1995, Berger, 1934]. EEG technology evolves from this primary findings until becoming in one of the most used neuro-analysis techniques in both, clinical and research scenarios. A typical EEG montage is shown in Figure 2.5 using the so-called $10-20$ system use from 21 to 32 electrodes placed as single units over the scalp surface (Figure 2.5(a)). However, nowadays, hdEEG can contain more than 250 electrodes commonly distributed in a silicon helmet that can be adapted to most of the human heads (Figure 2.5(b)) [Liu et al., 2017, Marino et al., 2016].

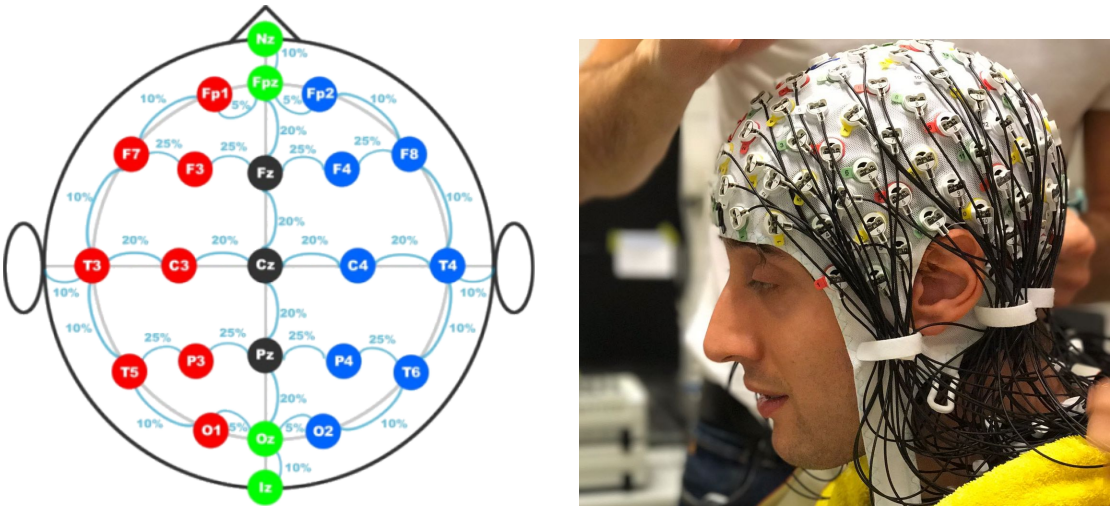

(a) $10-20$ EEG system

(b) hdEEG cap

Figure 2.5: EEG arrays. Figure 2.5(a) show a typical $10-20$ EEG system electrode distribution, adapted from [Trans Cranial Technologies Ltd., 2012] public license. Figure 2.5(b) show a hdEEG helmet with 128 electrodes, the image was adquired in the Laboratory of Movement Control and Neuroplasticity, Department of Movement Sciences, KU Leuven, Belgium.

Advanced signal processing methods for denoising, filtering, and bad channel correction or interpolation allows the use of hdEEG improving not only the signal to noise ratio but the discrimination of information from a large number of electrodes

[Storti et al., 2012]. However, single EEG analysis cannot find specific activation zones in the brain cortex, thus, multi-modal analysis including structural information of the human head can allow improving the spatial capabilities of EEG [Michel et al., 2012].

2.2 The forward problem

Most of the MRI or CT based brain function technologies (fMRI, PET, SPECT) have a good spatial resolution, but poor temporal analysis windows (more than 2s) (see section 5.1, Figure 5.1). Moreover, CT based imaging techniques are considered energy invasive due to the amount of energy used to impulse the X-ray particles (from $12 - 50$keV) [Juan et al., 2015]. In contrast, EEG has a good temporal resolution (around 1ms) but lacks spatial discrimination. Nevertheless, the synergetic effects connecting spatial MRI and functional EEG analysis techniques allows reduction of the weakness for single technique analysis [Grech et al., 2008]. Thus, EEG Source Imaging (ESI) connecting structural head models and distributed source localization techniques improves the time and spatial resolution of single MRI or EEG analysis [Michel et al., 2004] (see section 5.1). ESI information is used for diagnosis and preoperative stages of brain surgery being, in most cases, the only suitable analysis tools because of the high risk of surgical interventions [Martinez et al., 2017, Voges et al., 2011, Titto et al., 2004, Waberski et al., 2000]. In most of these applications, the goal is to reconstruct the active electrical sources in the brain, which underlie the measured EEG signal [Michel et al., 2012]. This source localization step requires not only the EEG data themselves, but also detailed information about geometry and physical properties of the head tissues that are interposed between the sources and the sensors. In particular, a *lead-field* matrix relating current sources in the brain to the electric potentials measured on the scalp is required by any distributed source localization algorithm [Sarvas, 1987, Tadel et al., 2011, Baillet et al., 2001, Vatta et al., 2010, Akalin Acar et al., 2016, Vorwerk et al., 2014] (see section 5.3). The *lead-field* matrix can be obtained by solving the quasi-static approximation of Maxwell's equations for any given current density distribution [Clark et al., 1968, Sarvas, 1987].

2.2.1 Poisson equation and boundary conditions

The EEG forward problem entails the calculation of potentials $\phi(\boldsymbol{r})$ induced by a primary current density $\boldsymbol{J}(\boldsymbol{r})$ in a head volume $\Omega \in \mathbb{R}^3$ with $\partial\Omega \in \mathbb{R}^2$

boundary, holding inhomogeneous and anisotropic conductivity $\boldsymbol{\Sigma}(\boldsymbol{r})$. In most of practicals task, the relevant frequencies of EEG spectra are considered between 0.1 and 100 *Hz*[Hallez et al., 2007b]. Therefore, a quasi-static approximation of Maxwell's equations can be formulated, leading to the Poisson's equation as follows [Rahmouni et al., 2017]:

$$\nabla\cdot(\boldsymbol{\Sigma}(\boldsymbol{r})\nabla\boldsymbol{\phi}(\boldsymbol{r})) = -\nabla\cdot\boldsymbol{J}(\boldsymbol{r}),\ \ \forall\boldsymbol{r}\in\Omega \tag{2.1}$$

$$\boldsymbol{\phi}(\boldsymbol{r})|^{+}_{\Gamma_l} = \boldsymbol{\phi}(\boldsymbol{r})|^{-}_{\Gamma_l}\ \ \text{on}\,\Gamma_l,\ \ \forall l=1,\ldots,N \tag{2.2}$$

$$(\boldsymbol{\Sigma}(\boldsymbol{r})\nabla\boldsymbol{\phi}(\boldsymbol{r}))\cdot\hat{\boldsymbol{n}}(\boldsymbol{r})|^{+}_{\Gamma_l} = (\boldsymbol{\Sigma}(\boldsymbol{r})\nabla\boldsymbol{\phi}(\boldsymbol{r}))\cdot\hat{\boldsymbol{n}}(\boldsymbol{r})|^{-}_{\Gamma_l},\ \ \text{on}\,\Gamma_l \tag{2.3}$$

$$(\boldsymbol{\Sigma}(\boldsymbol{r})\nabla\boldsymbol{\phi}(\boldsymbol{r}))\cdot\hat{\boldsymbol{n}}(\boldsymbol{r})|_{\partial\Omega} = 0,\ \ \text{on boundary}\,\partial\Omega \tag{2.4}$$

where $\boldsymbol{\Sigma}(\boldsymbol{r})\in\mathbb{R}^{3\times3}$ is a conductivity tensor spatially varying through $\boldsymbol{r}$, N is the number of interfaces Γ_l (i.e., head layers), $\hat{\boldsymbol{n}}(\boldsymbol{r})\in\mathbb{R}^3$ is a unit vector normal to Γ_l at $\boldsymbol{r}$, and $g(\boldsymbol{r})|^{\pm}_{\Gamma_l}$ stands for the trace of function $g(\boldsymbol{r})$ from both sides of the l-th interface Γ_l. Furthermore, the solution of 2.1 requires setting propper boundary conditions between each pair of neighboring compartments. Thus 2.2, and 2.3 stands for the Dirichlet and Neumann flux conditions respectively, while 2.4 (or non-flux homogeneous Neumann condition) implies that no current can flow out through the human head interface $\partial\Omega$ into the air [Stenroos et al., 2012, Sarvas, 1987].

Figure 2.6 shows an irregular head domain Ω enclosed in a rectangular box $\tilde{\Omega}$ including the surrounding air (left). We also show the tissue conductivities $\boldsymbol{\Sigma}_l$ and the interfaces between tissue compartments Γ_l, including the Ω boundary $\partial\Omega$, that is the limit with the air where the homogeneous Newman flux condition (Eq 2.4) must be achieved. Furthermore, the additional region $\tilde{\Omega}$ (known as *fictitious domain*) is commonly introduced to fulfill the Eq 2.4 in finite difference numerical solutions [Turovets et al., 2014, Ramière et al., 2007]. Additionally, we include a graphic description (right) of the boundary conditions between different compartments, where $\hat{\boldsymbol{n}}$ is a normal vector to the interface surfaces Γ_l.

2.2.2 The current dipole

The current source density in Eq 2.1 can be defined as a function $\boldsymbol{\iota}(r)=-\nabla\boldsymbol{J}(\boldsymbol{r})$, representing a current dipole that can be defined as two single monopoles inducing

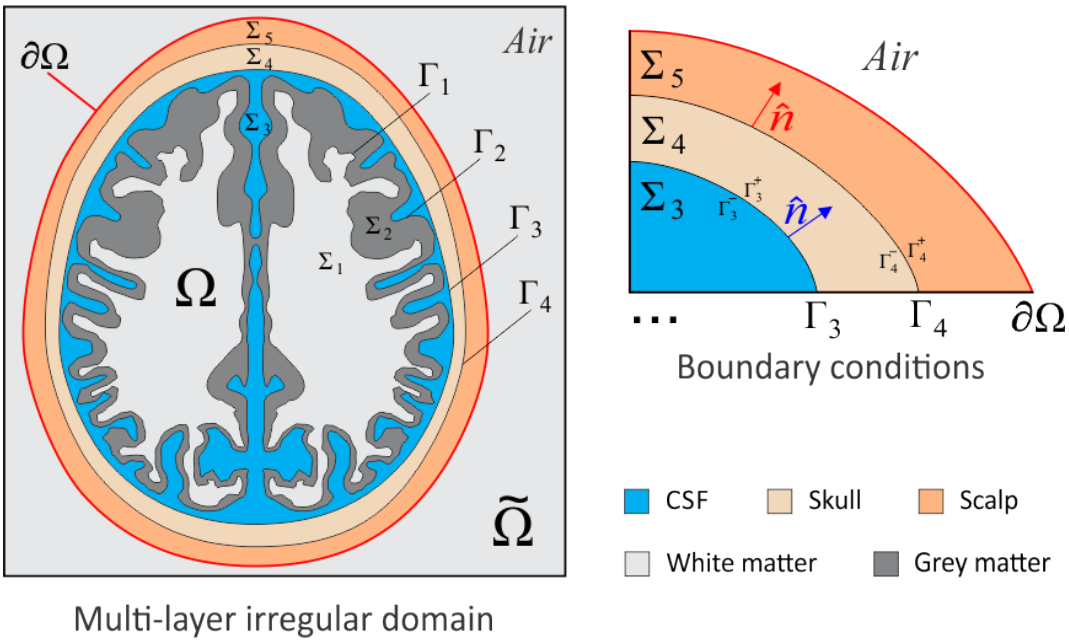

Figure 2.6: Head volume domain Ω and boundary conditions for a multiple layer conductor.

a current source I_m and a current sink $-I_m$, and separated by a distance d as follows:

$$\iota(r)=\lim_{d\to 0} I_m \left[\delta(r-r^+)-\delta(r-r^-)\right] \tag{2.5}$$

Where r^+ and r^- represent the current source and sink positions respectively, d is the distance between r^+ and r^-, I_m is the current magnitude, and r is the relative dipole position. Additionally, $\delta(\cdot)$ stands for the Dirac function [Li and Yan, 2009].

Figure 2.7 show the equipotential lines in a realistic head model volume with 5-layers isotropic conductivity compartments. A single dipole was placed in the grey matter compartment, with r^+ source and r^- sink, separated for a d distance and a I_m magnitude. The electrical source and sink generates the dipole current vector $\overrightarrow{d} = \overrightarrow{r^- r^+}$ with a position r estimated in the middle point between r^+ and r^-. Further, we can define the dipole moment in the r position as:

$$\mathbf{d}(\boldsymbol{r}) = I_m \overrightarrow{d} \tag{2.6}$$

The current dipole moment at position $\boldsymbol{r}$ represents an active pyramidal cell's cluster at macroscopic level.

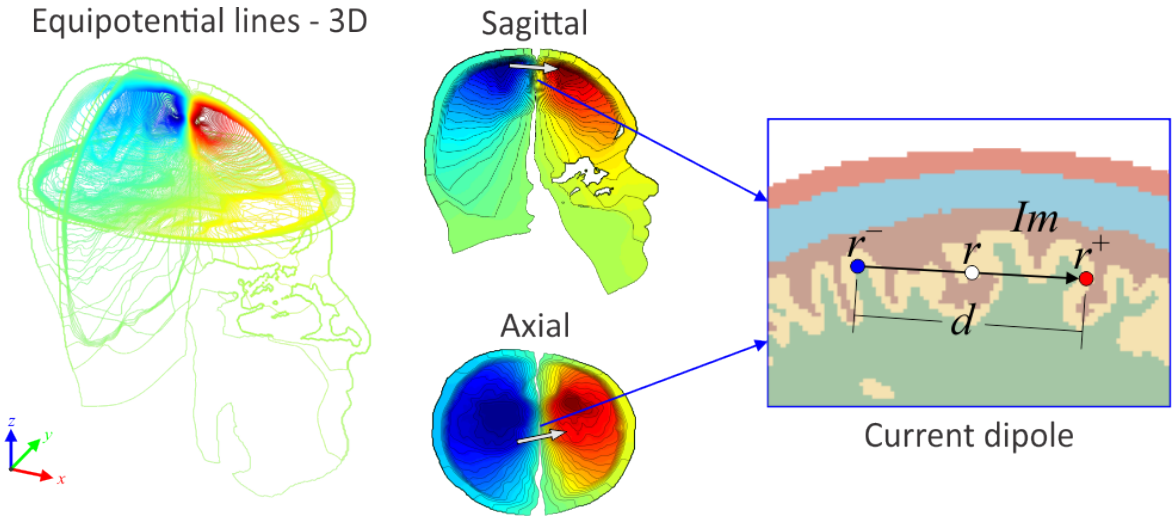

Figure 2.7: Equipotential lines for a single current dipole oriented in the X direction (Sagittal plane).

2.2.3 Anisotropic conductivity tensor

The conductivity measures the ability to propagate an electric current for a considered material, depending entirely on the nature of the material, the state of aggregation of its parts and its temperature. [Maxwell, 1873]. Moreover, some materials can have anisotropic conductivity behaviors. Thus, in an isotropic medium, the conductivity measures are equal in every direction, but, in an anisotropic medium, this is not the case. Isotropic conductivity quantities can be represented as a positive scalar, but, for an anisotropic medium, a tensor definition is introduced. One of the best ways to describe the anisotropic behavior of a conductivity medium is using an ellipsoid. Thus, when the ellipsoid shape is a sphere, the medium conductivity represented by the sphere radius has an equal magnitude in all directions (isotropic), but, when the principal semi-axial distances are different, the shape differs from a sphere and becomes an irregular ellipsoid where the conductivity measure represented by the distance between the center of the ellipsoid and its surface depends on the direction. The anisotropic behavior can be modeled using a 3D symmetric eigenspace tensor that holds a eigenvalues matrix expressing the deformation magnitude for the principal orthogonal axes, and the eigenvectors matrix describing a local rotational transformation. Therefore, using conductivity tensors, it is possible to include the anisotropic conductivity behavior of the head tissues, where the largest eigenvalue signifies the magnitude of the principal

anisotropic direction of the medium, given by its correspondence direction (eigenvector) [Wolters et al., 2006].

Anisotropy is important in conductivity head modeling and even more in ESI solutions, in this regard, several works deal with anisotropic of the skull [Montes et al., 2016, Lanfer et al., 2012, Cuartas et al., 2014b] and the white matter [Wolters et al., 2006, Cuartas et al., 2014a, Hallez et al., 2008], being the most known anisotropic behavior tissues in the human head. Anisotropic conductivity symmetric tensor can be defined as:

$$\boldsymbol{\Sigma}(\boldsymbol{r}) = \boldsymbol{T}(\boldsymbol{r})\boldsymbol{D}(\boldsymbol{r})\boldsymbol{T}(\boldsymbol{r})^T, \qquad \boldsymbol{\Sigma} = \begin{bmatrix} \sigma_{11} & \sigma_{12} & \sigma_{13} \\ \sigma_{12} & \sigma_{22} & \sigma_{23} \\ \sigma_{13} & \sigma_{23} & \sigma_{33} \end{bmatrix} \tag{2.7}$$

where $\boldsymbol{\Sigma}(\boldsymbol{r})\in\mathbb{R}^{3\times3}$ is the eigenspace tensor symmetric matrix for the $\boldsymbol{r}$ position, $\boldsymbol{T}(\boldsymbol{r})\in\mathbb{R}^{3\times3}$ is a rotation local transfer matrix to the global coordinate system (eigenvectors), $\boldsymbol{D}(\boldsymbol{r})\in\mathbb{R}^{3\times3}$, $\boldsymbol{D}(\boldsymbol{r})$=diag$(\sigma_{lon}^{(\boldsymbol{r})}, \sigma_{trv}^{(\boldsymbol{r})}, \sigma_{trv}^{(\boldsymbol{r})})$ is a diagonal matrix holding the local conductivity values in the transversal $\sigma_{trv}^{(\boldsymbol{r})}\in\mathbb{R}^+$, and longitudinal $\sigma_{lon}^{(\boldsymbol{r})}\in\mathbb{R}+$ directions (eigenvalues), respectively.

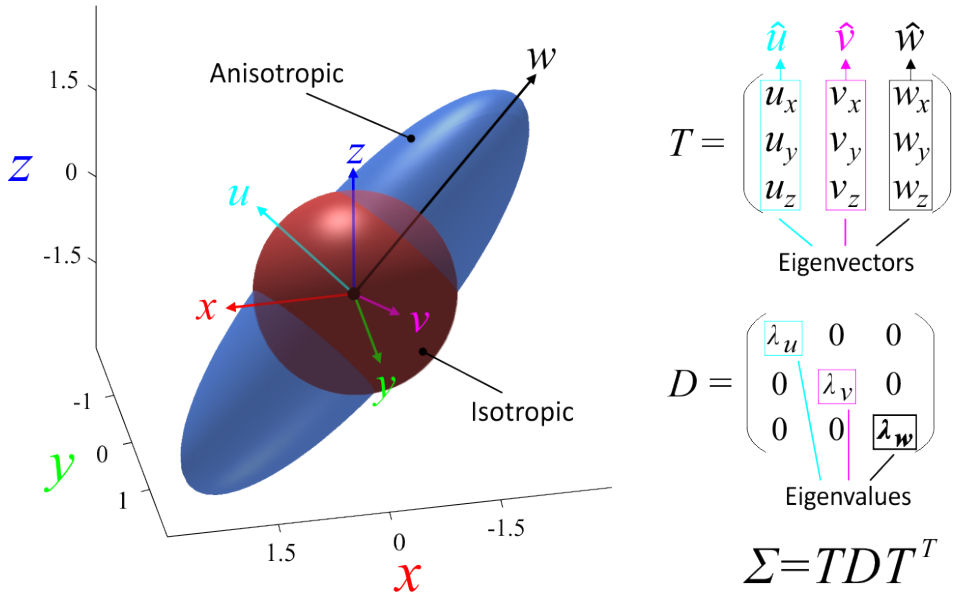

Figure 2.8: Anisotropic eigenspace conductivity tensor.

Figure 2.8 shows a conductivity tensor $\boldsymbol{\Sigma}$ including the eigenvectors matrix $\boldsymbol{T}$ and the eigenvalues matrix $\boldsymbol{D}$. The $\boldsymbol{T}$ matrix holds the column vector directions for the

rotated universe (u, v, w), also, the $\boldsymbol{D}$ diagonal matrix contains the eigenvalues λ_{uvw} that acts as scaling factors for the eigenvector axis $(\hat{u}, \hat{v}, \hat{w})$. The figure shows an isotropic sphere (in red) and an anisotropic ellipsoid (in blue) with $\hat{w}$ as the principal eigenvector, corresponding to the mayor eigenvalue, thus $\lambda_w > \lambda_u, \lambda_v$.

2.3 Solving the forward problem

The solution of the forward problem in EEG source analysis involves the solution of Poisson's equation (Eq 2.1) for a multilayer conductor volume, taking into account proper boundary conditions (Eq 2.2, 2.3 and 2.4) [Haueisen et al., 1997, Ramière et al., 2007]. The Dirichlet condition Eq 2.2, only holds for interfaces not connected with air, and states that the potential cannot have discontinuities crossing a boundary [Hallez et al., 2007b]. Similarly, Neumann condition (or flux condition) Eq 2.3 states that all charges leaving one compartment through a boundary interface Γ must enter the other compartment. Besides, as a particular case, no current can be injected outside the human head volume due to the very low conductivity of the air, this meaning that the current flux outside the head is null, this is known as the Neumann homogeneous condition represented by Eq 2.4 [Wolters et al., 2007b].

2.3.1 Generalized inhomogeneous anisotropic medium Poisson equation

For the $\boldsymbol{\iota}(r)$ current source (Eq 2.5) and the symmetric conductivity tensor $\boldsymbol{\Sigma}$ (Eq 2.7), we can define the conservative form of Eq 2.1 as follows:

$$\frac{\partial}{\partial x}\left(\sigma_{11}\frac{\partial \phi}{\partial x}+\sigma_{12}\frac{\partial \phi}{\partial y}+\sigma_{13}\frac{\partial \phi}{\partial z}\right)+\frac{\partial}{\partial y}\left(\sigma_{12}\frac{\partial \phi}{\partial x}+\sigma_{22}\frac{\partial \phi}{\partial y}+\sigma_{23}\frac{\partial \phi}{\partial z}\right)+\frac{\partial}{\partial z}\left(\sigma_{13}\frac{\partial \phi}{\partial x}+\sigma_{23}\frac{\partial \phi}{\partial y}+\sigma_{33}\frac{\partial \phi}{\partial z}\right)=\boldsymbol{\iota}(r) \quad (2.8)$$

where $\sigma_{ij} \in \mathbb{R}$ are the entries of the conductivity matrix tensor $\boldsymbol{\Sigma}$ 2.7.

The solution of the Poisson equation 2.1 (or the conservative form 2.8) for realistic free-form head volumes is only possible using numerical approximations [Irimia et al., 2013, Volkov et al., 2009]. However, symmetrical mediums can lead to analytical solutions [De Munck et al., 1993].

2.3.2 Spherical head model

The spherical head model is the simplest approach to solve the propagation Poisson equation [De Munck et al., 1993]. For this model, the different tissues conforming the head are modeled as concentric spheres, where every tissue (scalp, skull, gray matter, white matter among others) has its own conductivity value, being the scalp the outer sphere that contains the EEG electrodes. The high symmetry of this type of models allows analytical solutions [De Munck et al., 1993], however, several authors shows that the simplifying spherical head model induces source localization errors bigger than $30mm$ due to the strong simplification of the realistic and irregular shape of the human head [Hallez et al., 2008, Henson et al., 2009]. Nonetheless, the spherical head model provides an analytical solution allowing comparisons against numerical approximations, being in most cases, the only way to validate a numerical solution [Vanrumste et al., 2001b, Vanrumste et al., 2001a].

DeMunk analytical solution

There are several analytical solutions for spherical head volumes, in this work we use the analytical solution in a layered anisotropic spheroidal volume according to De Munck [De Munck, 1988]. The solution is formulated for concentric spheres with radii $r_1 < r_2 < \ldots < r_N$, including anisotropic layers S_i for $i = 1, \ldots, N$ as the regions between the boundaries.

Figure 2.9 show the generalized concentric multi-sphere layered for anisotropic mediums [De Munck et al., 1993]. where $\boldsymbol{r}_e$ is a point in the outermost surface $\partial\Omega$ (corresponding to layer radii r_N), $\boldsymbol{r}_{dip}$ is a dipole position contained in a layer S_i for $i = 1, \ldots, N-1$, holding moment $\mathbf{d}$. Thus, Eq 2.9 allows the analytical calculation of the potential $V(\boldsymbol{r}_{dip}, \mathbf{d}, \boldsymbol{r}_e)$ for an arbitrary position in the $\partial\Omega$ boundary $\boldsymbol{r}_e \in \partial\Omega$, generated by a current dipole with $\boldsymbol{r}_{dip}$ position and $\mathbf{d}$ moment. Moreover, each layer S_i contains radial ξ_i and tangential η_i conductivities that can be adjusted to set up an anisotropy medium in an arbitrary layer S_i. Eq 2.9 depends on the Legendre P_n and the associated Legendre polynomials P_n^1, functions f_η and g_η depending on the ξ_i and η_i conductivities, and other constants that can be deeply analyzed in [De Munck, 1988, De Munck et al., 1993]. DeMunck formulation allows the calculation of scalp potentials for a spherical configuration, including also anisotropic behaviors. Although the solution is not realistic, the analytical formulation becomes an important way to validate numerical solutions of the EEG forward problem

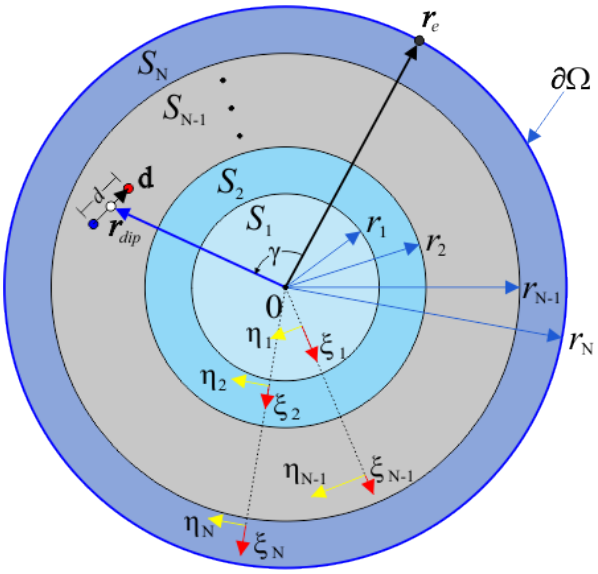

$$V(\boldsymbol{r}_{dip}, \mathbf{d}, \boldsymbol{r}_e) = \frac{d}{4\pi\xi_N \boldsymbol{r}_e^2} \sum_{n=1}^{N} \frac{2n+1}{n} \left(\frac{\boldsymbol{r}_{dip}}{\boldsymbol{r}_e}\right)^{n-1} \left(f_\eta n \cos\alpha P_n(\cos\gamma) + g_\eta \cos\beta \sin\alpha P_n^1(\cos\gamma)\right) \tag{2.9}$$

Figure 2.9: Layered anisotropic spherical volume conductor

[Volkov et al., 2009, Turovets et al., 2014, Wolters, 2003, Hallez, 2009].

2.3.3 Realistic head models: Numerical solutions

The spherical head modeling is a useful tool for general analysis, but, when the accuracy is an important factor (like in surgery planing) more realistic approaches are needed [Pai et al., 2005, Wang et al., 2008, Palagan et al., 2011, Vorwerk et al., 2014]. The solution of the Poisson equation for realistic free-form head volumes is only possible using numerical approximations [Irimia et al., 2013]. A realistic head volume can be obtained from neuroimages such MRI or CT that contains a large number of slices in a series of two-dimensional images.

The most simplistic numerical solution from neuroimaging structural real data is the boundary element method (BEM) [Ferguson et al., 1997]. BEM is widely used because of its low computational needs, however, most solutions only consider three surface boundaries (scalp, skull, and brain), and is restricted to isotropic conductivities. There are two main methodologies that can handle anisotropic conductivity and realistic multi-layered patient-specific forward solutions, Finite Element Method (FEM) [Wolters et al., 2002, Liu et al., 2005], and the Finite Difference Method (FDM) [Vanrumste et al., 2001b, Hallez, 2009].

In this section, we briefly introduce the BEM and FEM numerical solutions, while chapter 3 is devoted to the proposed FDM solution (GFDARM).

2.3.4 The Boundary element method - BEM

The BEM numerical technique is restricted only to isotropic conductivity mediums, nonetheless, it is still widely used because of its low computational needs. BEM method provides a forward solution by calculating the potential at the volumetric boundary interfaces for a given dipole current source. Thus, a head model is built from encapsulated surfaces representing the boundary between two considered tissues. Most BEM solutions consider only 3 interfaces: brain-skull, skull-scalp and scalp-air where EEG electrodes are placed. The regions between the interfaces are assumed to have isotropic conductivity. To calculate a numerical solution, each interface surface is tessellated in small boundary elements.

The electrical potential $V(\boldsymbol{r})$, over a surface S_k at position $\boldsymbol{r} \in S_k$ can be calculated for a conductivity medium conformed with closed surfaces S_i $(i = 1 \dots n_s)$ for n_s compartments each having isotropic conductivity σ_j^{in} as follows:

Figure 2.10 show a typical 3-layered BEM model with tesselated brain, skull, and scalp surfaces, where $\boldsymbol{r'}_{dip}$ is a current dipole inducing the potential $V_0(\boldsymbol{r})$ over the scalp surface S_3 at position $\boldsymbol{r}$. The self contained surfaces $(S_1 \in S_2 \in S_3)$ holds isotropic conductivities σ_i.

Eq 2.10 formulated by [Geselowitz, 1967] and [Sarvas, 1987] can be calculated for a potential V_0 induced for a current dipole immersed in a medium with σ_0 isotropic conductivity. Additionally, conductivity $\sigma_k = \left(\sigma_k^{in} + \sigma_k^{out}\right)/2$ is the mean conductivity value for two different mediums with interface surface S_k, and $\Delta\sigma_i = \sigma_k^{in} - \sigma_k^{out}$ is the difference. Furthermore Eq 2.10 integrals can be solved for piecewise approximated closed surfaces consisting of differential surface elements dS_i' with surface normal orientations $\boldsymbol{n}'$ at positions $\boldsymbol{r}'$. The boundary surfaces S_i are commonly approximated by tesselated triangulations, replacing the integral by summations over the triangle planes dS_i' differential elements [Fuchs et al., 2002, Van't Ent et al., 2001, De Munck et al., 2000, De Munck, 1992].

2.3.5 The Finite Element Method - FEM

FEM technique is the most used volumetric technique for the solution of the forward problem in realistic head models. The *Galerkin* approach is used to solve Eq 2.1 with

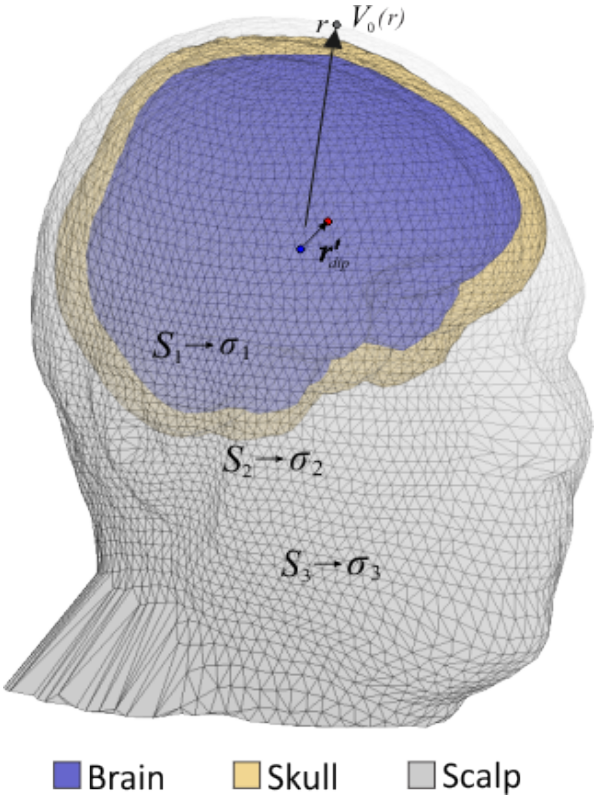

$$\sigma_k V(\boldsymbol{r}) = \sigma_0 V_0(\boldsymbol{r}) + \frac{1}{4\pi}\sum_{i=1}^{n_S}\Delta\sigma_i \oiint_{S_i} V(\boldsymbol{r}')n(\boldsymbol{r}')\frac{\boldsymbol{r}'-\boldsymbol{r}}{\|\boldsymbol{r}'-\boldsymbol{r}\|^3}dS_i \quad (2.10)$$

Figure 2.10: BEM realistic head model with 3 layers

boundary conditions 2.2, 2.3, 2.4. Thus, Eq 2.1 is multiplied with a ψ function, and then integrated over the Ω head volume as follows:

In FEM, 3D volume is discretized in small elements, typically tetrahedrons or hexahedrons. Due to this, FEM techniques require a tesselating stage in order to obtain a discretized volumetric mesh. The Venant approach from [Wolters et al., 2007a] use deformable hexahedrons with a *shift* parameter between 0 and 0.45 to adapt the hexahedrons vertex to the irregular morphology of a realistic head model interfaces Γ_l and boundary $\partial\Omega$. Figure 2.11 show a hexahedral meshing for a realistic 5-layers head volume. We show a plane-axial projection of two different shifting deformation meshes with $shift = 0$ producing regular cuboids (top), and $shift = 0.45$ producing a node-shifting mesh with irregular hexahedrons (button). Figure was obtained using the FEM Simbio routine for the *fieldtrip* toolbox [Vorwerk et al., 2018]. Furthermore, Eq 2.11 is called *weak* or *integral* forward problem formulation and can be solved for discrete computational points φ_i, with $i = 1 \ldots N$ corresponding to the N vertices

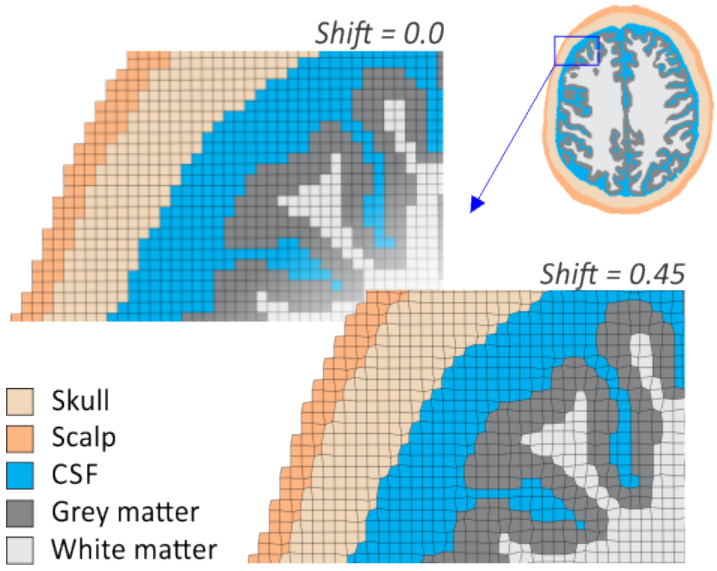

$$-\int_G \psi \nabla \cdot (\boldsymbol{\Sigma} \nabla \boldsymbol{\phi})\, dG = \int_G \psi I_m dG \quad (2.11)$$

Figure 2.11: FEM hexahedric mesh for a 5 layered realistic head model

of the discretized irregular grid. Thus, unknown potentials $\phi(\boldsymbol{r})$ can be obtaining as follows:

$$\phi(\boldsymbol{r}) = \sum_{i=1}^{N} \varphi_i \psi_i(\boldsymbol{r}) \quad (2.12)$$

Where $\psi_i(\boldsymbol{r})$ denotes a set of test functions, also called basis functions, having local support and producing a span of piecewise polynomial functions. Further, due to the local support of the basis, each equation in Eq 2.12 consists only of a linear combination of φ_i including the analyzed point and its adjacent points producing a linear equation system $\boldsymbol{A}\boldsymbol{\phi} = \boldsymbol{I}$, where $\boldsymbol{\phi} \in \mathbb{R}^N$ are potential unknowns, $\boldsymbol{I} \in \mathbb{R}^N$ is a given current source vector, and $\boldsymbol{A} \in \mathbb{R}^{N \times N}$ is the system or *stiffness* matrix. In general, the *stiffness* matrix $\boldsymbol{A}$ is very big (commonly $N > 5 \times 10^6$), making the estimation of potentials $\boldsymbol{\phi}$ very computationally expensive. Thus, iterative solvers for large sparse systems are used to reduce the computational burden and increase efficiency EEG FEM-based forward solvers [Engwer et al., 2017, Wolters et al., 2002].

2.4 Experiments and results

Methods used in this Chapter experiments and results are described in Chapters 3 and 4. In specific, *ghost-filling* finite difference anisotropic reciprocity method (GFDARM) is introduced in Chapter 3. Additionally the 6−layer spherical head model is described in section 3.2.1, and realistic head model (RHM) in sections 4.1 and 4.2.

2.4.1 GFDARM vs available numerical solutions

We use the 6−layers spherical head model describe in section 3.2.1 to analyze the differences between the BEM, FEM, and GFDARM numerical techniques to solve the Poison Eq 2.1. Thus, with the purpose of simulate a neuroimage data head model, we build a 3D discretized sphere with $1mm^3$ voxel resolution. We illustrate the 6-layer discretized spherical head model in the Figure 2.12, where the skull and WM areas can be configurated to include anisotropic conductivity. Additionally, we use a set of 112 electrodes evenly distributed over the scalp surface in 6 geodesic circles, as suggested by [Stenroos et al., 2012].

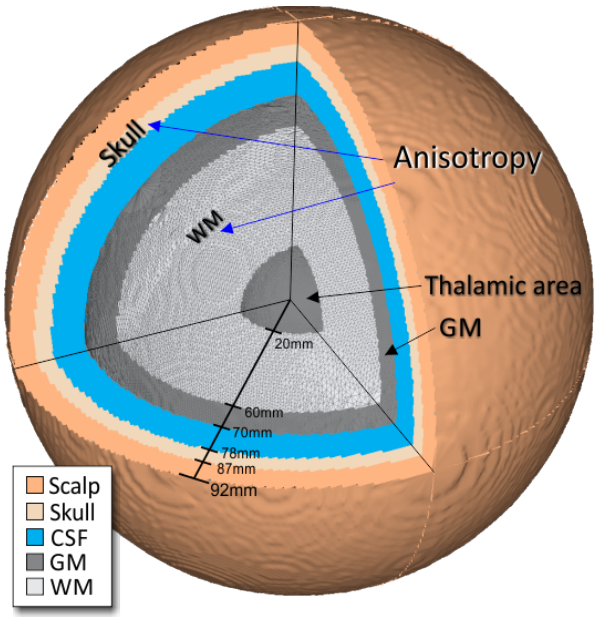

Figure 2.12: Spherical head model, including anisotropic skull and WM.

Moreover, we use the *Simbio* FieldTrip to calculate an isotropic FEM solution with a hexahedral meshing, and deformation grid $shifth = 0.3$ (default value for

the FEM routine) [Vorwerk et al., 2018]. Also, we calculate a BEM solution for a 3-layers spherical head model including only the scalp, skull, and brain interfaces. Tesselation and forward calculations were done using the Fieldtrip BEM routines [Oostenveld et al., 2011], including mesh surfaces holding 6000 vertex, for a total of 18000 discrete points solution. Besides, we also perform forward calculations in a reciprocity setup using the GFDARM algorithm, building two different head models, a fully isotropic medium, and an anisotropic and skull head model. For the anisotropic case, we set the WM radial/tangential ratio to 9:1, and for the skull to 1:10 as we explained in section 3.2.1.

In the first test, we analyze the electrode potentials for the considered numeric techniques, namely, BEM, FEM, and anisotropic GFDARM, including also the anisotropic analytical solution. To this end, we induce a single dipole in the positive Z orthogonal direction, placed in the GM compartment.

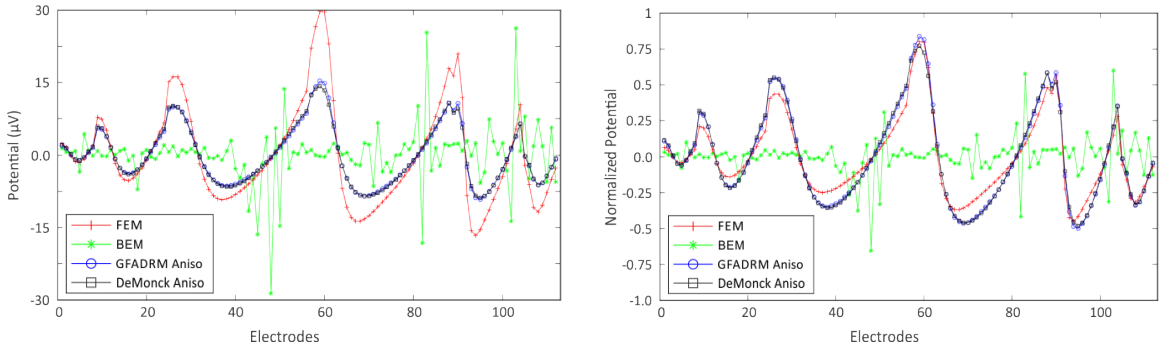

(a) Electrode potentials

(b) Normalized potentials

Figure 2.13: Numerical BEM, FEM and GFDARM potentials. Also including analytical solution potentials.

Figure 2.13 shows the potentials for the considered 112 electrodes. We plot the potentials in the original space Figure 2.13(a), including also a normalization plot, where we divide the potential magnitudes by the dynamic range of the entire signal 2.13(b). Results show that numerical GFDARM anisotropic solution has a high correspondence with the analytical distribution, whereas, the FEM solution present not only an increased potential magnitude in the original potential space Figure 2.13(a) but also significant differences in the normalized Figure 2.13(b), showing an energy distribution that does not correspond to the anisotropic modelling. Finally, BEM solution shows an unusual potential distribution compared against the analytical reference, suggesting

that BEM approximations are not the best way to calculate forward potentials.

Furthermore, we build a $3mm^3$ regularly spaced source grid including 20955 dipoles in the GM and thalamic areas. Subsequently, we calculate analytical solutions using the DeMunck algorithm, for a fully isotropic medium and a WM and skull anisotropic medium as reference potential spaces. Then, we performed tests comparing the isotropic analytical solution against isotropic GFDARM and FEM. Finally, we compared the anisotropic analytical solution against the isotropic FEM and an anisotropic skull and WM A-GFDARM.

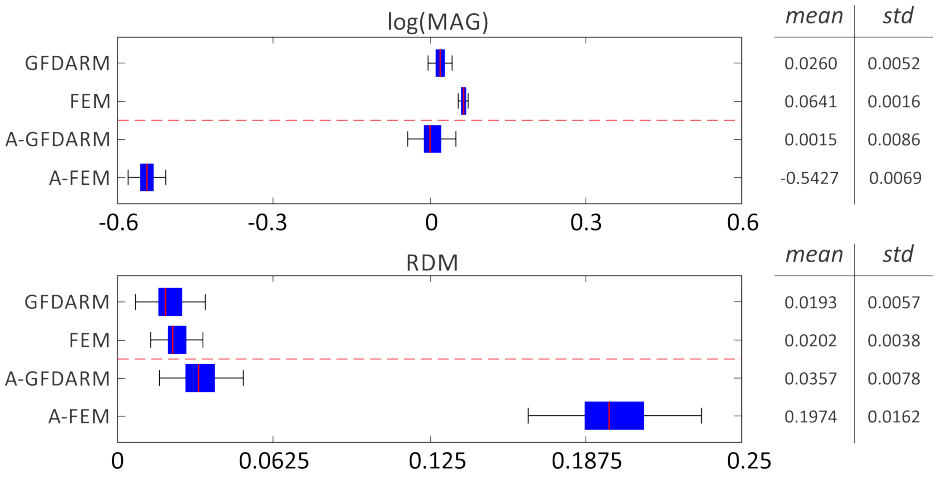

Figure 2.14: log Magnitude ln(MAG) and relative difference measures (RDM).

Figure 2.14 shows the log(MAG) and RDM results, showing the total span data as black lines, and the 50% of the data as blue boxes, including the medium value as a red line. We also include mean and standard deviation (std) values for every test, and a horizontal dashed red line separating the isotropic (top) and the anisotropic (button) tests. For the isotropic cases we can appreciate a slightly better performance for the GFDARM technique with lower mean values. However, FEM technique report very low *std* rates indicating a high consistency for every source considered positions. Besides, for the anisotropic case, the results show an appreciable increase in the mean errors for the A-GFDARM test. Accordingly, for the A-FEM test, mean errors present a high increment, indicating important differences between the isotropic FEM solution and the anisotropic analytical DeMunck solution.

2.4.2 Computational performance

We performed a computational analysis to investigate the time spent and memory allocation needed for the numeric BEM, FEM, and GFDARM solutions. Moreover, is important to notice that BEM and FEM methods need meshing calculation and allocation to yields a solution. However, we don't include the time spend to generate the irregular FEM and BEM meshes, due to the fast tessellation algorithms routines from FiledTrip [Oostenveld et al., 2011]. Additionally, FEM *Simbio* solution needs an octahedral grid mesh, a precalculated lead-field potentials matrix, and the system or stiff matrix to perform forward calculation. On the other hand, BEM requires a 3-layers self-contained mesh and a stiff system matrix. Likewise, GFDARM needs also a stiff system matrix, and a precalculated lead-field potentials matrix, where the mesh grid does not have to be stored, due to its regular nature, corresponding to the already regularly voxel information data from neuroimages [Cuartas et al., 2015].

Parameters	**GFDARM**	**FEM**	**BEM**
Stiff Matrix size	[3342701×3342701]	[3342701×3342701]	[6000×18000]
Stiff Isotropic Memory (Mb)	380.0716	728.5138	823.9746
Stiff Anisotropic Memory (Mb)	**628.3062**	-	-
Mesh size	-	[8×3262312]	[3×6000]
Mesh Memory (Mb)	-	300.5338717	1.2374
Leadfield size	[111×3342701]	[112×3342701]	-
Leadfield Memory (Mb)	2830.8090	2856.3119	-
Total Memory (Mb)	**2030.4002**	3885.3595	825.2120
Isotropic Total time (sec)	**12091**	27555	258.17
Anisotropic Total time (sec)	**23841**	-	-

Table 2.1: Computational performance for GFDARM, *Simbio* FEM, and *FieldTrip* BEM techniques, using the synthetic spherical head model.

Table 2.1 shows the computational performance results including memory allocation in Mega bytes (Mb), size of numerical arrays, and total calculation time in seconds (sec). We use the spherical discrete head model (Figure 2.12), with a volume Ω holding 3262312 voxels. Results show that the proposed GFDARM technique outperforms FEM in both, time spent and memory allocation, showing a very reliable computational performance. By contrast, BEM solution is fast, and present low memory requirements, but the numerical approximation is not as accurate as the FEM or FDM solutions.

Realistic head model

As a final test, we analyze the computational performance of the GDFARM algorithm and the *Simbio* FEM solution defining three diferent head models, namely, Isotropic GFDARM, Anisotropic GFDARM, and FEM. We use the realistic head model (RHM) defined in section 4.1.2, holding 4910171 voxels in the segmentation volume. Moreover, we employed a full isotropic RHM for the FEM and Isotropic GFDARM cases, and, we include anisotropic skull and white matter for the anisotropic GDFARM model, as explained in section 4.2.

Parameters	Isotropic **GFDARM**	Anisotropic **GFDARM**	*Simbio* **FEM**
Stiff Matrix size	[5059556×5059556]	[5059556×5059557]	[5068594×5068594]
Stiff Memory (Mb)	574.2584	863.2035	1099.767921
Leadfield size	[69×5059556]	[69×5059556]	[70×5068594]
Leadfield Memory (Mb)	1572.4690	1572.4690	2706.9212
Mesh grid size	-	-	[8×4910171]
Mesh grid Memory (Mb)	-	-	453.1859
Total Memory (Mb)	**2146.7274**	**2435.6725**	4259.8751
Total time (sec)	**18251**	**29386**	46976

Table 2.2: Computational performance for GFDARM and FEM in the Realistic head model.

Table 2.2 shows the computational performance results. Regarding the GFDARM algorithm is important to notice that the finite differences based solution doesn't need to store a mesh grid for the numerical analysis. Furthermore, considering isotropic models, FEM solution is 2.57 times slower than the Isotropic GFDARM, needing almost the double memory allocation space. By contrast, the Anisotropic GFDARM is 1.6 times faster and needs 1.75 less memory allocation than the Isotropic FEM. Finally, times and memory values reported in Tables 2.1 and 2.2 where estimated in a `Intel Xeon CPU E5-2687W` computer with 64Gb RAM, using the Matlab software environment.

2.5 Discussion

We compared the most commonly used EEG forward modeling numeric techniques. To this end, we introduce a synthetic spherical discrete volume holding cubic voxels with discretization step $h = 1mm^3$, resembling a real neuroimage data. Numerical models

were examined against the analytical DeMunck spherical solution [De Munck, 1988]. Further, we calculate two different head models for the analytical estimations, namely, a full isotropic medium, and an anisotropic skull and WM models. Our results show high correspondence between the analytical DeMunck solution and the proposed finite differences forward modeling, that we called *ghost-filling* finite difference anisotropic reciprocity method (GFDARM), and that is introduced and deeply analyze in the Chapter 3.

2.5.1 Considerations concerning BEM

The comparison for the FielTrip BEM modeling show high discrepancies with the analytical DeMunck solution. However, for general analysis, BEM continues as the most used forward solver. This due to its fast computation and low memory requirements. Moreover, most BEM available solvers consider only three surface boundaries, neglecting important tissue compartments like the CSF [Strobbe et al., 2014a], and the brain GM and WM [Vorwerk et al., 2014]. Nevertheless, strong BEM simplification directly impacts in the accuracy of the technique, as we can appreciate in Figure 2.13, where the potential distribution is very dissimilar in comparison with the analytical solution and the volumetrics FEM and GFDARM techniques. Therefore, we suggest using volumetric modeling for detailed analysis, considering that the memory allocation and computing capacities nowadays are sufficient to deal with volumetric based forward solutions.

2.5.2 Considerations concerning FEM

Simbio FEM forward solution presents a high correspondence with the analytical DeMunk solution for the considered spherical head data a shown in Figure 2.13. Moreover, FEM shows a very low standard deviation in the results reported in Figure 2.14 indicating a high consistency of the solution. Yet, the main restriction of FEM is the computational time and memory needed to store the precalculated potentials, and the non-regular solution mesh.

Although *Simbio* FEM is accurate, the FielTrip *open* pipeline is not clear about the required tools or routines to include anisotropic information [Vorwerk et al., 2018]. However, despite the anisotropic inclusion difficulties, FEM is the most widely known and used volumetric technique with anisotropic capabilities, that can handle across voxel conductivity information. The technique evolves for tetrahedral irregular meshing

to hexahedral quasi-regular grids, including a minor shifting parameter that adapts the solution points to the irregular boundaries of realistic head models (Figure 2.11). In this way, is interesting finding that the major advantage fo FEM techniques, that is multi-resolution voxelizations, were changed for a quasi-regular cubic grid that contains the same discrete potential unknowns that the available voxels in a neuroimage data, resembling a GFDARM regular cubic voxelization very much voxelization [Vorwerk et al., 2014, Wolters et al., 2006].

2.5.3 Considerations concerning GFDARM

Results show that GFDARM technique is very versatile, and we can include isotropic or anisotropic compartments in a voxelwise distribution. Besides, GFDARM solution does not need a meshing or tessellation stage, neither the allocation of the solution points in a separated mesh structure. Moreover, a fundamental advantage of GFDARM as compared to FEM's is its straightforward integration with neuroimaging registers (MRI, CT or DWI to DTI data), which are always acquired in regular tri-dimensional grids. This makes GFDARM intrinsically suitable for modelling across voxel conductivity and anisotropy, without the need of defining tissue compartments with homogenous physical properties.

Also, our results show that the GFDARM technique has the best performance of the three considered numerical solutions, presenting very similar potentials compared against the analytical spherical Demunck solution as shown in Figure 2.13. In addition, GFDARM present the best behaviour reported in Figure 2.14, showing a high consistency for the wide range of considered source positions. Finally, the slight error increment between the results for the isotropic GFDARM and the anisotropic A-GFDARM in the Figure 2.14 is caused by the discrete voxelized approximation in the local anisotropic tensors for the skull and WM, that is a fundamental discretization error associated to every numerical approximation technique.

2.5.4 General computational considerations

The reported BEM solution results of Table 2.1, considering 18−thousand potential unknowns for the estimated spherical head model, dist from the number of calculations and memory requirements of the volumetric techniques. Thus, FEM and GFDARM solution spaces hold more than 3.3 millions potential unknowns. For this reason, BEM solution is the faster and memory inexpensive considered numerical technique, but

its desirable computational performance is due to the substantial simplification of the forward solution. On the other hand, FEM and FDM volumetric techniques require more time and memory to perform forward calculations for high-resolution volumes. Moreover, Table 2.1 shows significant differences for the stiff matrix memory demands, where the isotropic GFDARM needs half of the memory compared against the FEM solution. Besides, even the anisotropic GFDARM stiff matrix needs a less amount of memory than the isotropic FEM model, this due to the GFDARM 18-points stencil (section 3.1, Figure 3.1) that generates a sparse diagonal stiff matrix with only 19 non zero values per row. Further, leadfield matrix allocation is very similar for GFDARM and FEM, but, the irregular FEM grid adds not only complexity to the solution, but also increase memory demands. Finally, analyzing total time and memory allocation results, the GFDARM proposed technique outperforms the *Simbio* FEM solution, using almost half of the time and memory requirements.

We also analyze the computational performance of the volumetric FEM and GFDARM techniques for the RHM data set, showing concluding results in favor of the proposed GFDARM. Thus, isotropic *Simbio* FEM, takes almost twice of the time compared with anisotropic GFDARM, being also three times slower than the isotropic GFDARM. Moreover, FEM total memory allocation is almost the double of the GFDARM storage needs, as shown in Table 2.2.

Finally, based on our results, we are confident in indicating that the proposed ghost-filling finite difference anisotropic reciprocity method (GFDARM) is a more accurate and computational reliable technique compared against the available state of the art *Simbio* FEM solution.

Chapter 3

Finite difference EEG forward problem solution

Significant progress has been made in the EEG forward solution FEM-based techniques in order to reduce the computational requirements, improve the accuracy of the models, and the source singularities [Vorwerk et al., 2018]. Such techniques are the subtraction [Drechsler et al., 2009, Wolters et al., 2007b], partial integration [Schimpf et al., 2002], or the Venant approaches [Wolters et al., 2007a], being the last, one of the most computational efficient FEM methodologies [Vorwerk et al., 2014]. This approach uses hexahedral deformable elements instead of the commonly tetrahedral voxels. For the solution of the linear equation system they use the incomplete-Cholesky preconditioned conjugate gradient in a reciprocity approach. This setup allows fast forward calculations, but, in comparison with BEM, the computational time is still a major issue.

The main difference between FDM and FEM techniques is that FEM uses an adaptative grid with arbitrary/adjustable node positions, and, in this way, FEM solutions are very versatile, thus in theory, one can adjust their reconstruction accuracy and computational demands by varying the mesh resolution locally [Lee et al., 2007]. In contrast, FDM discretizes a volume into a uniform voxel grid and this seems like a big disadvantage, especially for complex boundaries morphologies, however, the developing in neuroimaging techniques have reached a point where higher spatial resolutions are possible. Thus, nowadays, $0.5mm^3$ or even more detailed spatial resolutions are possible. In this sense, a fundamental advantage of FDM as compared to FEM is its straightforward integration with structural imaging data (CT/MR and DWI),

which are always acquired in regular tri-dimensional grids [Huang et al., 2016]. This makes FDM intrinsically suitable for modeling across voxels differences in conductivity and anisotropy, without the need of defining tissue compartments with homogenous physical properties [Li and Yan, 2009]. On the other hand, FEM commonly needs a tesselation stage to build a nonregular grid, and also complex and more expensive numerical approximations due to its non-regular grid nature [Haufe et al., 2015]. In comparison with FEM, there is not a significant effort in the bibliography to improve the computational time and accuracy of the EEG forward solution FDM-based techniques. In [Mohr et al., 2003], authors analyses four different solvers (SOR, CG, AMG and a variation of CG) concluding that the best solution yields with the AMG solver, nevertheless, most solutions use the stationary SOR solver algorithm [Hallez, 2009], or fictitious domain approaches [Turovets et al., 2014] suggesting that fast and stable FDM solutions are still an open issue [Salman et al., 2016].

This chapter is devoted to the formulation of an efficient and numerical stable FDM volumetric framework to solve the EEG forward problem in realistic head data that can handle voxelwise anisotropic definitions, aiming to improve the ESI accuracy but also reducing the computational burden of the technique.

3.1 Finite difference numerical solution

A finite difference formulation of a partial differential equation uses a regular cubic grid, covering the domain Ω, and approximating the solution at the nodes of the grid by a finite difference operator.

Figure 3.1 show the volumetric FDM stencil S_j arround the node j with asymmetric discretization distances dx_F and dx_B for the X orthogonal direction where F stands for *frontal* in the positive X cartesian direction, and B for *back* in the negative X cartesian direction. Symilarly, for the Y direction we deffine dy_E and dy_W with E being *east* (positive Y direction) and W *west* (negative Y direction), and for Z distances dz_N and dz_S with N stands for *north* (positive Z direction) and S for *south* (negative Z direction). We use central finite differences for the 3D stencil of Figure 3.1 to approximate the conservative Poisson equation 2.8 for an inhomogeneous anisotropic medium (see section 2.3.1) following the previous works of [Saleheen et al., 1998, Asenco et al., 1991] where each vertex of the regular cubic domain correspond to a voxel centroid in the Ω domain.

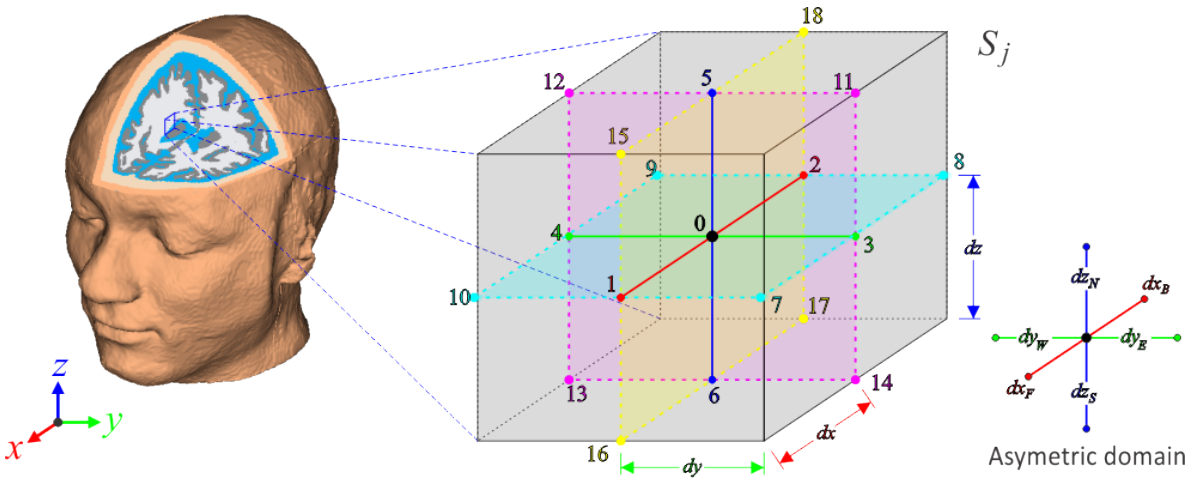

Figure 3.1: FDM 3D stencil.

We can rewrite the conservative form of the Poisson equation 2.8 as follows:

$$(\sigma_{11}\phi_X)_X + (\sigma_{22}\phi_Y)_Y + (\sigma_{33}\phi_Z)_Z + 2(\sigma_{12}\phi_X)_Y + 2(\sigma_{23}\phi_Y)_Z + 2(\sigma_{13}\phi_Z)_X = \iota(r) \quad (3.1)$$

Where $(\sigma_{ij}\phi_A)_B = \frac{\partial}{\partial B}\left(\sigma_{ij}\frac{\partial \phi}{\partial A}\right)$.

Thus, we define second order Taylor series around the node 0 for its 18 neighbours in the 3D stencil FIgure 3.1, around the S_j region, for $\sigma\phi_i$, where ϕ_i corresponds to a potential unknown for the node $i = 0, \ldots, 18$, and σ stands for the local conductivity value. Furthermore, to approximate the partial derivates in Eq 3.1, we consider the following Taylor expansions:

$$\left.\begin{matrix}\sigma_{11(1)}\phi_1 \\ \sigma_{11(2)}\phi_2\end{matrix}\right\} \rightarrow (\sigma_{11}\phi_X)_X = \frac{\sigma_{11(1)}\phi_1 - (\sigma_{11(1)} + \sigma_{11(2)})\phi_0 + \sigma_{11(2)}\phi_2}{(dx_F + dx_B)^2} \quad (3.2)$$

Eq 3.2 show the finite difference approximation for the second order Taylor series $\sigma_{11(1)}\phi_1$ and $\sigma_{11(2)}\phi_2$, where $\sigma_{mn(i)}$ is the (m, n) positions of the conductivity tensor Σ (defined in section 2.2.3) for the $i-th$ node. Thus, from the Eq 3.2 one can obtain the approximation for the first term of Eq 3.1 corresponding to the second order derivate $(\sigma_{11}\phi_X)_X$. Similarly, expansions for $\sigma_{mm(1,\ldots,6)}\phi_{1,\ldots,6}$ allows to obtain the second and

third terms of Eq 3.1.

$$\left.\begin{array}{l}\sigma_{12(7)}\phi_7\\ \sigma_{12(8)}\phi_8\\ \sigma_{12(9)}\phi_9\\ \sigma_{12(10)}\phi_{10}\end{array}\right\} \rightarrow 2\left(\sigma_{12}\phi_X\right)_Y = \frac{\sigma_{11(7)}\phi_7 - \sigma_{11(8)}\phi_8 + \sigma_{11(9)}\phi_9 - \sigma_{11(10)}\phi_{10}}{\left(dx_F + dx_B\right)\left(dy_E + dy_W\right)} \tag{3.3}$$

Moreover, Eq 3.3 show the approximation for the mixed derivate $2\left(\sigma_{12}\phi_X\right)_Y$. Furthermore, we calculate Taylor series for $\sigma_{mn(7,\ldots,18)}\phi_{7,\ldots,18}$, obtaining second-order approximations for the mixed derivates terms (fourth, fifth and sixth terms) of Eq 3.1.

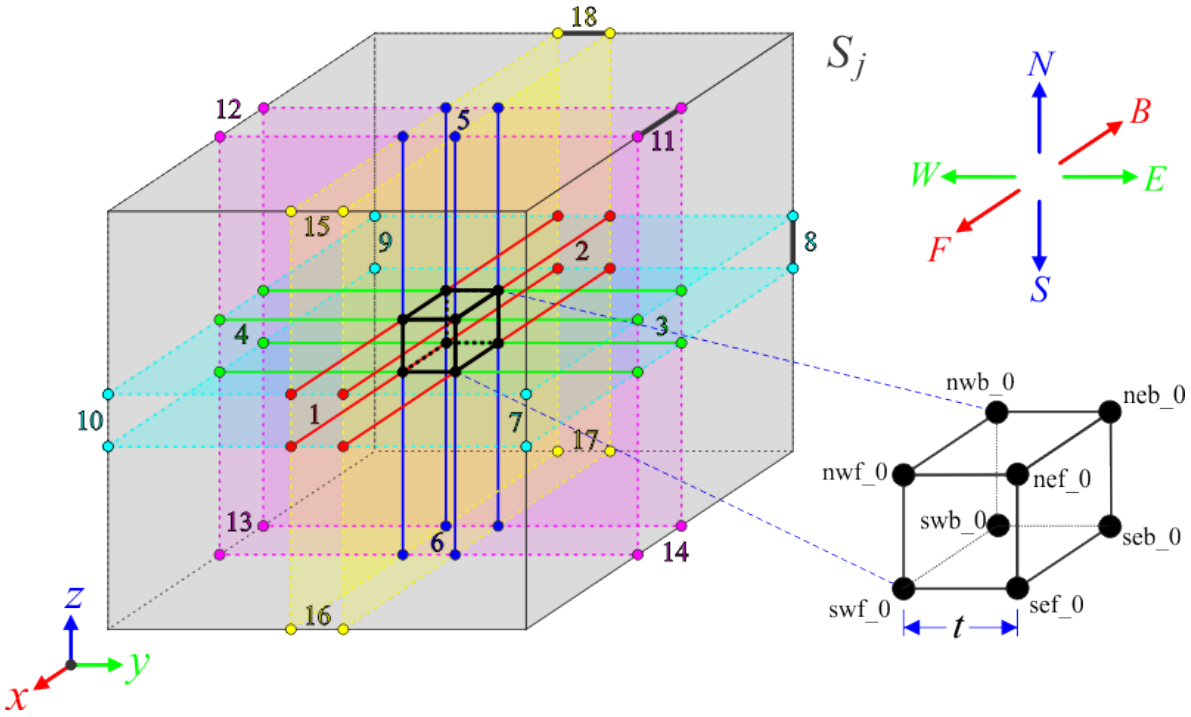

Figure 3.2: Transition layer stencil around node 0.

However, for in a generalized discrete inhomogeneous anisotropic media, the neighbour elements around the node 0 for the 3D stencil S_j can have different conductivity tensors, inducing singularities in the conductivity derivatives at the boundaries interfaces Γ_l or between anisotropic elements. For boundaries with a definite normal direction, these can be handled with proper boundary conditions, but

this is not the case for the stencil S_j where the normal directions are not clearly defined, causing that the Newman flux boundary condition (Eq 2.3) cannot be properly formulated in the Γ interfaces. For this reason, a transition layer method introduced by [Asenco et al., 1991, Panizo et al., 1977] is used in order to remove the singularities in the spatial derivatives of the conductivity tensors and satisfy the Dirichlet and Newman flux general boundary conditions (Eq's 2.2 and 2.3).

In the transition layer technique, the node 0 from the stencil S_j (Figure 3.1) is split into 8 nodes forming a cube with sizes of length t. The partition generates 8 different asymmetric domains around the node 0, having continuous conductivities and derivates over the entire layer. Thus, the transition layer acts as a buffer creating a smooth transition of the of the conductivities and their derivatives from one element to another [Saleheen et al., 1998].

Figure 3.2 show the transition layer partition around node 0, including the cube division that creates 8 new asymmetric stencils, each for every new node around node 0.

$$\phi_0 = \lim_{t \to 0} \frac{1}{8} \sum_{k=1}^{8} \phi_k^{tl} \tag{3.4}$$

3.1.1 FDM formulation

Eq 3.4 can be solved to obtain the finite differences approximation for the S_j stencil, around the node 0 for the ϕ_0 unknown potential as a numerical approximation of the Poisson Eq 2.1, in a inhomogeneous anisotropic medium, taking into account the Dirichlet (Eq 2.2) and Newman flux (Eq 2.3) boundary conditions, where ϕ_k^{tl} are the 8 central nodes in the transition layer. Furthermore, for the limit $t \to 0$, the nodes of the cubic transition layer return to their original positions generating regular inter-node distances, and resulting in a single formulation for the S_j region that can be expressed as follows:

$$\sum_{i \in S_j}^{18} \alpha_i^j \phi_i^j - \left(\sum_{i \in S_j}^{18} \alpha_i^j \right) \phi_0^j = \boldsymbol{\iota}_f \tag{3.5}$$

Where j is a specific node position of the discretized head volume Ω, with $\phi_0^j \in \mathbb{R}$ the potential unknown associated to node 0 for the S_j neighbor (see Figure 3.2) defining the unknown potential neighbor unknowns $\phi_i^j \in \mathbb{R}$. Moreover, $\boldsymbol{\iota}_f$ is a discretized dipole

current source. Additionally, $\alpha_i^j \in \mathbb{R}$ are the FDM coefficients form the discretized Eq 3.1 depending on the anisotropic conductivity tensor $\boldsymbol{\Sigma}$ (see section 2.2.3) and the inter-node distances dx, dy and dz, that can be writed as follows:

$$
\begin{aligned}
\alpha_1 &= \frac{1}{4dx^2}\left(\sigma_{11(9)} + \sigma_{11(2)} + \sigma_{11(0)} + \sigma_{11(3)}\right), \quad \alpha_2 = \frac{1}{4dx^2}\left(\sigma_{11(4)} + \sigma_{11(0)} + \sigma_{11(1)} + \sigma_{11(7)}\right) \\
\alpha_3 &= \frac{1}{4dy^2}\left(\sigma_{22(13)} + \sigma_{22(4)} + \sigma_{22(0)} + \sigma_{22(5)}\right), \quad \alpha_4 = \frac{1}{4dy^2}\left(\sigma_{22(6)} + \sigma_{22(0)} + \sigma_{22(3)} + \sigma_{22(11)}\right) \\
\alpha_5 &= \frac{1}{4dz^2}\left(\sigma_{33(16)} + \sigma_{33(6)} + \sigma_{33(0)} + \sigma_{33(2)}\right), \quad \alpha_6 = \frac{1}{4dz^2}\left(\sigma_{33(1)} + \sigma_{33(0)} + \sigma_{33(5)} + \sigma_{33(18)}\right) \\
\alpha_7 &= \frac{1}{2dxdy}\left(\sigma_{12(1)} + \sigma_{12(15)}\right), \quad \alpha_8 = -\frac{1}{2dxdy}\left(\sigma_{12(3)} + \sigma_{12(14)}\right) \\
\alpha_9 &= \frac{1}{2dxdy}\left(\sigma_{12(2)} + \sigma_{12(18)}\right), \quad \alpha_{10} = -\frac{1}{2dxdy}\left(\sigma_{12(4)} + \sigma_{12(13)}\right) \\
\alpha_{11} &= \frac{1}{2dydz}\left(\sigma_{23(5)} + \sigma_{23(15)}\right), \quad \alpha_{12} = -\frac{1}{2dydz}\left(\sigma_{23(4)} + \sigma_{23(9)}\right) \\
\alpha_{13} &= \frac{1}{2dydz}\left(\sigma_{23(6)} + \sigma_{23(16)}\right), \quad \alpha_{14} = -\frac{1}{2dydz}\left(\sigma_{23(3)} + \sigma_{23(8)}\right) \\
\alpha_{15} &= \frac{1}{2dzdx}\left(\sigma_{13(1)} + \sigma_{13(7)}\right), \quad \alpha_{16} = -\frac{1}{2dzdx}\left(\sigma_{13(6)} + \sigma_{13(13)}\right) \\
\alpha_{17} &= \frac{1}{2dzdx}\left(\sigma_{13(2)} + \sigma_{13(8)}\right), \quad \alpha_{18} = -\frac{1}{2dzdx}\left(\sigma_{13(5)} + \sigma_{13(12)}\right)
\end{aligned}
\tag{3.6}
$$

Eq 3.6 show the obtained FDM coefficients α_i, with $i = 1, \ldots, 18$ for the transition layer Eq 3.4. Previous works consider the non-conservative form of the Poisson equation 2.1 [Saleheen et al., 1998, Hallez, 2009]. To our knoledge, this is the first time that the FDM coefficients for the EEG forward problem are obtained using the conservative form of the Poisson equation (Eq's 2.8 and 3.1) for the transition layer setup.

3.1.2 Discrete FDM current dipole

The current dipole for the considered FDM solution can be defined across the stencil S_j in the orthogonal directions x, y or z.

Figure 3.3 shows a discrete current dipole for the FDM cubic grid in the positive y direction. The dipole is defined across nodes 4 and 3 of the stencil S_j, where the node 4 corresponds to the current source with position r^- and magnitude I_m, and the node 3 corresponds to the current sink with position r^+ and magnitude $-I_m$. Moreover, relative

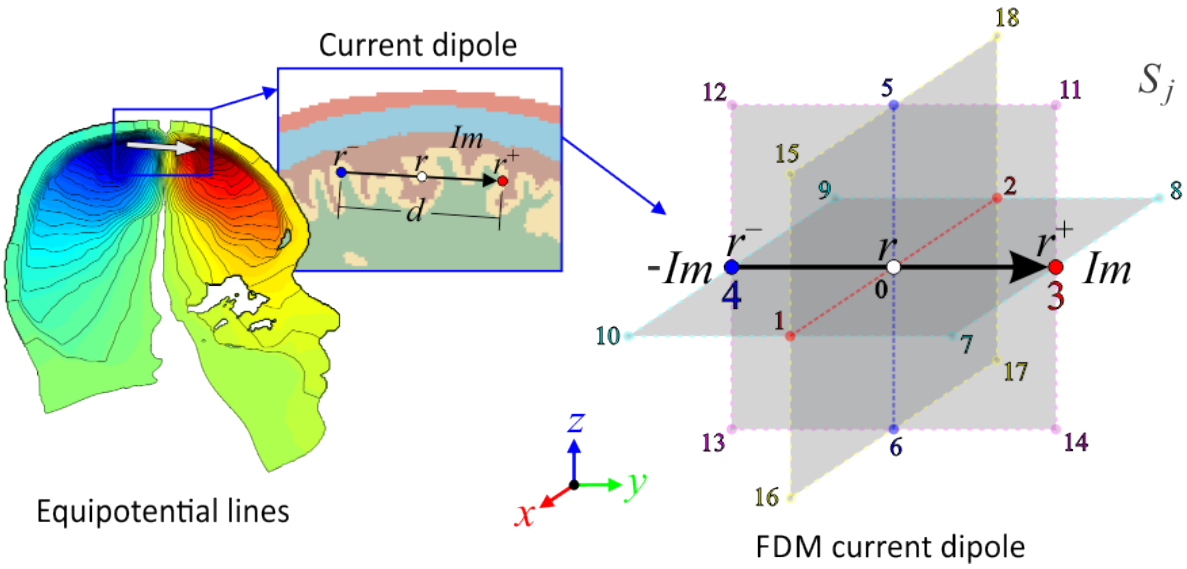

Figure 3.3: Transition layer stencil around node 0.

dipole position r lies in the middle distance between nodes 3 and 4 corresponding with node 0. Furthermore, the discretized FDM current dipole of 3.5 can be defined as:

$$\iota_f(r) = \begin{cases} -I_m/d, & r = r^- \\ I_m/d, & r = r^+ \\ 0, & \forall r \neq r^{\pm} \end{cases} \tag{3.7}$$

Where $d = \|r^+ - r^-\|_2$, and I_m is the current magnitude in Amperes.

For all cases under consideration, the Eq 3.5, including a discrete current dipole in the form of Eq 3.5, and considering the coefficients Eq 3.6 leads to solving a large linear equation system (LES) $A\phi = \boldsymbol{\iota}_f$. Where $\boldsymbol{\phi} \in \mathbb{R}^N$ is the solution vector holding N potential unknowns for N nodes in the FDM considered grid, $\boldsymbol{\iota_f} \in \mathbb{R}^N$ is the right-hand side vector representing a single discrete current dipole source, and $\boldsymbol{A} \in \mathbb{R}^{N \times N}$ is the so-called system or coefficient matrix.

3.1.3 Ghost-filling finite difference formulation (GFD)

The formulation of the coefficient matrix $\boldsymbol{A}$ depends on the FDM coefficients, the tissue conductivity tensors, and the discretization steps dx, dy and dz. However, the boundary conditions can considerably influence the matrix properties and the amount

of the unknowns of the LES [Ramière et al., 2007]. There are different methods to transform the 3D unknowns potentials from the volumetric FDM grid into a 1D vector in a LES formulation.

In the fictitious domain (FD) method, the volume conductor Ω is surrounded by an auxiliary domain $\tilde{\Omega}$ generally larger ($\Omega \subset \tilde{\Omega}$, see Figure 3.4) and with a simple/regular shape, containing low conductivity voxels representing the air, so, for a regular Cartesian box $\tilde{\Omega}$, the final three-dimensional space is always rectangular regardless the irregular shape of the immersed volume Ω. Further, the coefficient matrix formulation in FD becomes simple, due to the regular distribution of the potential unknowns. FD methods derive into tri-diagonal matrices that can be solved with fast circulant Fourier techniques [Ramière et al., 2007]. However, injecting low conductivity voxels increase the heterogeneity of the system matrix, decreasing its numeric stability, and implying additional unknowns in the final LES [Turovets et al., 2014].

In this work, we introduce a novel *ghost-filling* boundary solution for the proposed FDM formulation (GFD), relying on the generalized second-order FD approximation proposed by [Lin et al., 2017]. To this end, we add *ghost-cells* around the irregular boundary $\partial\Omega$, to fulfilling the non-flux homogeneous Neumann condition (Eq 2.4). The difference between the classic FD methods and GFD techniques lies in the coefficient matrix formulation. For the GFD case, we applied the natural row ordering method, assigning a label to the potentials ϕ_i^j, indicating its row position j and column position i for the system matrix, following the 18-neighbour stencil, Figure 3.1.

The Figure 3.4 shows an irregular head volume Ω with boundary $\partial\Omega$ separating the volume from the surrounding air. Moreover, Ω region is enclosed by a cuboid fictitious domain $\tilde{\Omega}$, including low conductivity voxels, representing the air. We also show a small zone of the Ω volume describing data segmented form neuroimages with regular rectangular voxels, where the red line is the discrete $\partial\Omega$ boundary. Further, we show the *ghost-filling* space (top) where the white dots represent the *ghost-cells* around the $\partial\Omega$ discrete interface. Similarly, blue dots represent the potential unknowns along the Ω domain. On the other hand, we show the *fictitious domain* (button) including additional low conductivity points describing the air, for the domain $\tilde{\Omega}$.

Taking into account that the current sources in Poisson Eq 2.1 must lie inside the head volume, or $\iota_f(r) \notin \partial\Omega$, we can write that $\iota_f|_{\partial\Omega} = 0$. Furthermore, for the Newman homogeneous flux condition (Eq 2.4) we can apply the *ghost-filling* finite difference as

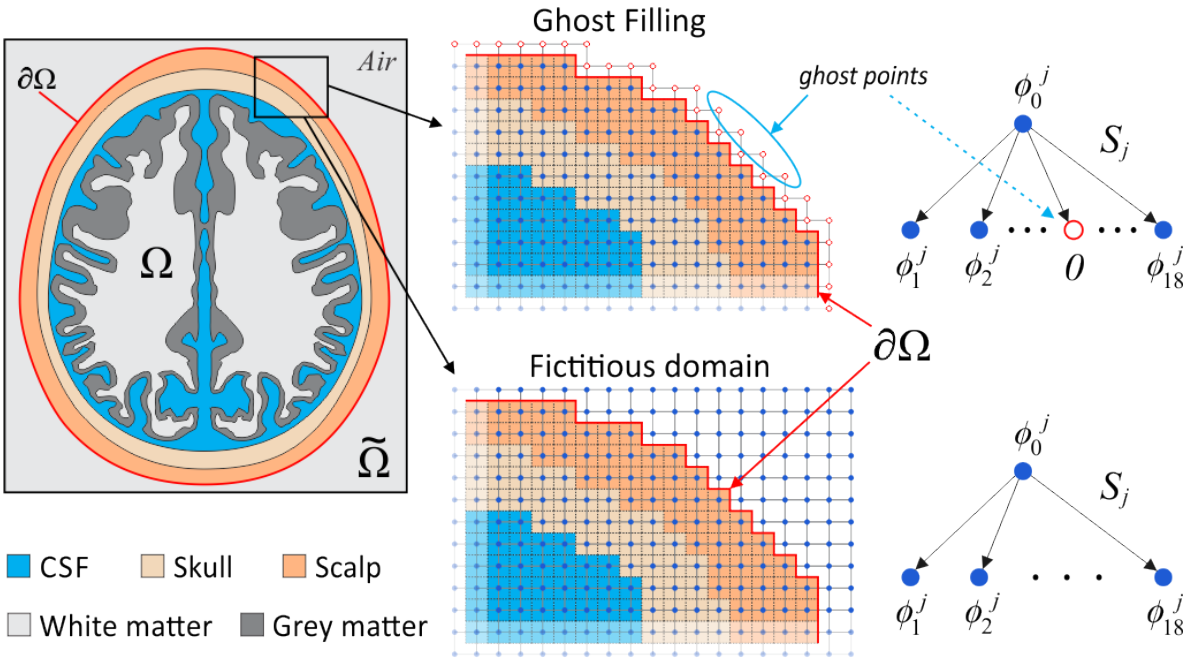

Figure 3.4: Head volume domain showing *ghost-filling* and fictitious domain for a discretized FDM grid.

follows:

$$\left.\frac{\partial \phi}{\partial r}\right|_{\partial\Omega} = \frac{1}{2h}\left(\phi_{\partial\Omega} - \phi_{-1}\right) + O\left(h^2\right) = 0 \tag{3.8}$$

Where h is the discretization step, $\phi_{\partial\Omega}$ is the unknown potential at the interface $\partial\Omega$ and ϕ_{-1} is the *ghost-cell* variable introduce to approximate the potential $\phi_{\partial\Omega}$ with second order accuracy truncation error $O\left(h^2\right)$.

Replacing Eq 3.8 in the FDM formulation Eq 3.5 we obtain:

$$\alpha_1^j\phi_1^j - \cdots - \alpha_{-1}^j\phi_{-1}^j - \cdots \alpha_{18}^j\phi_{18}^j - \left(\alpha_1^j - \cdots - \alpha_{-1}^j - \cdots \alpha_{18}^j\right)\phi_{\partial\Omega}^j = 0 \tag{3.9}$$

Where $\alpha_{-1}^j = 0$ for null air conductivity outside the head volume Ω [IT'IS, 2016], and $\phi_{-1}^j = 0$ taking into account the non-flux homogeneous Newman condition 2.4. Moreover, the *ghost-filling* Eq 3.9 allows the subtraction of *ghost-cell* potentials outside the head volume Ω from the coefficient matrix.

3.1.4 FDM Ghost filling coefficient matrix formulation

In general, the coefficient $c_{r,i}{\in}\mathbb{R}$ are the entries of system matrix $\boldsymbol{A}$, for the FDM formulation of the discretized head volume Ω, holding $N_Z{\in}\mathbb{Z}$ non-zero potentials unknowns $\phi_i^r{=}\phi(x_i^r, y_i^r, z_i^r){\in}\mathbb{R}$, with $(x_i^r, y_i^r, z_i^r){\in}\Omega$ the 3D FDM discretized spatial positions for the volume domain Ω, where $r, i{=}1, 2, \cdots, N_Z{\in}\mathbb{Z}$ represent the row and columns of the coefficient matrix $\boldsymbol{A}$ respectively. Moreover, we introduce $l_i^r(x_i^r, y_i^r, z_i^r){\in}\mathbb{R}$ as a penalization function for the *ghost-cell* variables as follows:

$$l_i^r(x_i^r, y_i^r, z_i^r) = \begin{cases} 1, & \phi_i^r \neq \phi_{-1}^r \\ 0, & \phi_i^r = \phi_{-1}^r \end{cases} \tag{3.10}$$

where ϕ_{-1}^r in Eq 3.10 represents the *ghost-cell* potentials. Thus $l_r(x_i^r, y_i^r, z_i^r) \neq 0$ for all non-*ghost-cell* unknowns in Ω. Further, we define the coefficients $c_{r,i}$ as follows:

$$c_{r,i} = \begin{cases} -\sum_{i \in S_r}^{18} \alpha_i^r, & \forall l_i^r \neq 0, \forall i = r \\ \alpha_i^r, & \forall l_i^r \neq 0 \in S_r, \forall i \neq r \\ 0, & \text{otherwise} \end{cases} \tag{3.11}$$

Where each row r corresponds to a neighbor S_r, and each column corresponds to the i position for the coefficient matrix A in the linear expansion of the spatial discrete coordinates (x_i^r, y_i^r, z_i^r) .

As a result, the combination of the proposed finite differences for the conservative Eq 3.1 with the *ghost-filling* solution Eq 3.9 results in a symmetric, predominant soft-diagonal, sparse coefficient matrix formulated in Eq 3.11, with only 19 non-zero entries per row.

The new system matrix $A_{GFD}{\in}\mathbb{R}^{(N\times N)_\Omega}$, (with N unknowns) holds not only a smaller conditional number than the FD system matrix $A_{FD}{\in}\mathbb{R}^{(M\times M)_{\tilde{\Omega}}}$, (with M unknowns), but also, the conditional number remains stable (similar values) for different model resolutions, showing stability. Additionally, $N < M$, implying that the A_{NZ} GFD matrix is smaller than the A_{FD} FD matrix.

3.1.5 Linear equation system solution

Several iterative methods have been developing for solving large and sparse linear systems similar to the proposed A_{GFD} [Volkov et al., 2009, Mohr et al., 2003,

Wolters et al., 2002, Wolters et al., 2000]. Yet, the choice of the solver depends mainly on two considerations: the convergence speed to achieve a given relative minimum residual, depending on the coefficient matrix properties, and the computational complexity of each iteration. Notably, the numerical properties of the coefficient matrix highly influence the convergence rate of any solver. Thus, the more ill-conditioned the system matrix, the slower the convergence of the iterative solver method. The condition number of $\boldsymbol{A}$, define as $C = \|\boldsymbol{A}\|\|\boldsymbol{A}^{-1}\|$, generally measures the sensitivity of a linear system solution to perturbations in the data. As such, it can be used to estimate the convergence rate of an iterative solver: the larger the conditional number, the larger the iterations needed to reach a desired minimal residual [Li et al., 2018]. In this regard, we use the preconditioning technique to reduce the condition number C, by selecting an adequate non-singular matrix $\boldsymbol{M}$ such that the condition number of the product $\boldsymbol{M}^{-1}\boldsymbol{A}$ is improved. Therefore, we can indirectly solve the LES in the following form:

$$\boldsymbol{M}^{-1}\boldsymbol{A}\boldsymbol{\phi} = \boldsymbol{M}^{-1}\boldsymbol{\iota}_f \tag{3.12}$$

where $M \in \mathbb{R}^{N\times N}$ is the so-called preconditioner for the system matrix $A \in \mathbb{R}^{N\times N}$, $\boldsymbol{\phi} \in \mathbb{R}^N$ in the vector of unknown potentials, and $\boldsymbol{\iota}_f \in \mathbb{R}^N$ is the right hand side of the LES (excitation).

3.1.6 Reciprocity in the ghost-filling finite difference anisotropic method

EEG source imaging (ESI) distributed solutions require a *lead-field* matrix $L \in \mathbb{R}^{N_E\times \mathbb{N}_D}$ relating the scalp potentials in N_E electrodes (sensors) due to N_D dipole sources generators in the brain compartment. Moreover, theoretically speaking, the forward problem should be solved for each of those dipoles, implying around N_D forward calculations. However, this is a bad scenario for a volumetric technique solution like FDM, this due to the size of the coefficient matrix and the computational burden to solve the sparse linear equation system equations (section 3.1.5) [Hallez et al., 2007b]. Therefore, we use the reciprocity approach for a given distribution of N_E electrodes over the scalp $\partial\Omega$ allowing us to calculate forward solutions for the electrodes space rather than for each dipole position.

Figure 3.5 illustrates the reciprocity theorem Eq 3.13, where a virtual dipole current I_{AB} is injected between the scalp electrodes A and B, generating the potential V_r. Further, current dipole I_r induces a potential U_{AB}. Thus, reciprocity Eq 3.13 states

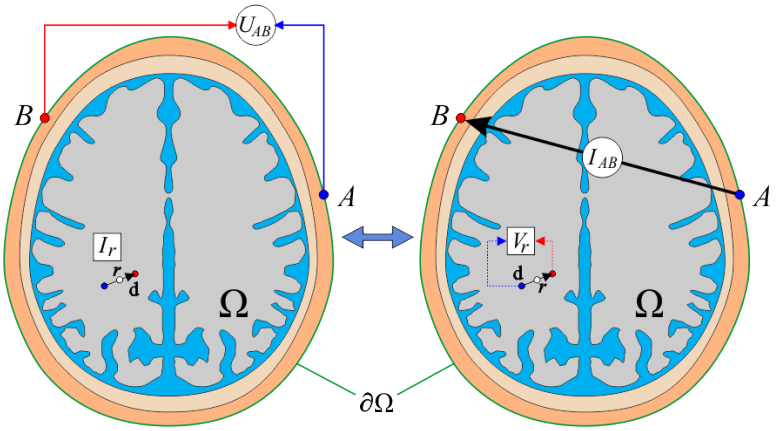

$$U_{AB}I_{AB} = V_r I_r \quad (3.13)$$

Figure 3.5: Reciprocity for the EEG forward problem

that there is an equality relating potentials U_{AB} and V_r with current sources I_{AB} and I_x [Plonsey, 1963]. Moreover, causes and effects can be exchanged to calculate a single unknown in Eq 3.13 if the other three parameters are known [Rush et al., 1969]. The reciprocity theorem for a random orientation dipole states that:

$$U_{AB}(\boldsymbol{r}, \mathbf{d}) = \frac{d^T \cdot \nabla V(r)}{I_{AB}} \quad (3.14)$$

Where $U_{AB}(\boldsymbol{r}, \mathbf{d})$ is called the *lead-pair* potential between two electrodes A and B generated for a dipole moment $\mathbf{d}$ (see section 2.2.3, Eq 2.6) placed in the position $\boldsymbol{r}$ with $\hat{d}$ orientation. Moreover I_{AB} is the current dipole between the same pair of scalp electrodes [Ziegler et al., 2014]. Is important to notice that the dipole sources are approximated from the current dipole I_{AB} applied to an electrode pair $A-B$ generating the potential $V(r)$ over a single $\boldsymbol{r}$ position in the head volume. In other words, using reciprocity, we are able to approximate the electrodes scalp potentials for any dipole moment $\mathbf{d}$ having position $\boldsymbol{r}$ and orientation $\hat{d}$. Thus, for a given electrode configuration and a single dipole position $\boldsymbol{r}$ we obtain:

$$U_{AB}(\boldsymbol{r}, \mathbf{d}) = \left(I_{AB}^{-1}\right) \cdot C_{xyz} \cdot \hat{d} \quad (3.15)$$

With $\left(I_{AB}^{-1}\right) \in \mathbb{R}^{(N_E \times N_E)}$ an electrode source and sink matrix for the N_E electrodes; $U_{AB} \in \mathbb{R}^{(N_E \times 1)}$ the *lead-pair* potentials and $C_{xyz}\,(r) \in \mathbb{R}^{N_E \times 3} = \|\mathbf{d}\|\,\nabla V(r)$ is a finite difference estimation for the partial derivates in $\nabla V(r)$ [Hallez et al., 2007b].

Reciprocity in FDM

To apply the reciprocity theorem for a dipole moment $\mathbf{d}$ with arbitrary position $\boldsymbol{r} = (r_x, r_y, r_z)$ in FDM, we approximate the partial derivates in $\nabla V(\boldsymbol{r})$ using finite differences as follows:

$$\nabla V(\boldsymbol{r}) \simeq \frac{V(r_x+dx)-V(r_x-dx)}{2dx}\hat{x} + \frac{V(r_y+dy)-V(r_y-dy)}{2dy}\hat{y} + \frac{V(r_z+dz)-V(r_z-dz)}{2dz}\hat{z} \quad (3.16)$$

Where dx, dy and dz, are the discretization steps in the three orthogonal directions. However, FDM only solve numerical potentials for the discrete grid points positions [Vanrumste et al., 2001b]. Thus, to obtain the potentials differences in Eq 3.16 for any arbitrary position $\boldsymbol{r}$ inside the head volume Ω, we use the trilinear interpolation method that approximate the potential $V(\boldsymbol{r})$ using the 8 surrounding FDM nodes that forms a cube around the point $\boldsymbol{r}$ [Hallez et al., 2005].

Finally, the electrode potentials for any given dipole moment $\mathbf{d}$ with $\boldsymbol{r}$ position can be calculated as:

$$V_L = L(\boldsymbol{r}) \cdot \mathbf{d} \quad (3.17)$$

Where $V_L \in \mathbb{R}^{(N_E \times 1)}$ is the electrode potentials for a single dipole with position $\boldsymbol{r} \in \mathbb{R}^{(3\times 1)}$ and moment $\mathbf{d} \in \mathbb{R}^{(3\times 1)}$. Moreover, $L(\boldsymbol{r}) = [L(r_x), L(r_y), L(r_z)]$, $L(\boldsymbol{r}) \in \mathbb{R}^{(N_E \times 3)}$, is the so-called *leadfield* matrix relating dipole current sources in the brain to the electric potentials measured on the scalp.

We apply the reciprocity theorem stated above for any given electrode distribution generating $N_E - 1$ *lead-pairs* that can be precalculated to obtain the electrode potentials for any given dipole moment $\mathbf{d}$ with $\boldsymbol{r}$ position using Eq 3.17. Moreover, using reciprocity we reduce the number of forward calculations, considering that the number of *lead-pairs* (around 100) is smaller than the number of sources ($N_E < N_D$). Since our method also incorporates anisotropy information, we refer to it as ***Ghost-filling* finite difference anisotropic reciprocity method** (GFDARM).

3.2 Experiments and results

3.2.1 Six layer spherical head model

We design a six layers anisotropic spherical head model, including CSF and two brain areas, a cortical, and a deep thalamic area to test the proposed GFDARM

numerical solution following [Hallez et al., 2005]. Figure 3.6 show the spherical head model with the following radii center to the different conductivity tissue boundaries: Scalp – 0.092 $[mm]$, Skull – 0.087 , Cerebro Spinal Fluid (CSF) – 0.078, Grey matter (GM) – 0.070, White Matter (WM) – 0.060, and thalamic inner sphere (TL) – 0.020. Furthermore, our spherical model incorporates a deep grey matter area (Thalamic inner sphere) to simulate deep brain tissue surround by anisotropic white matter medium.

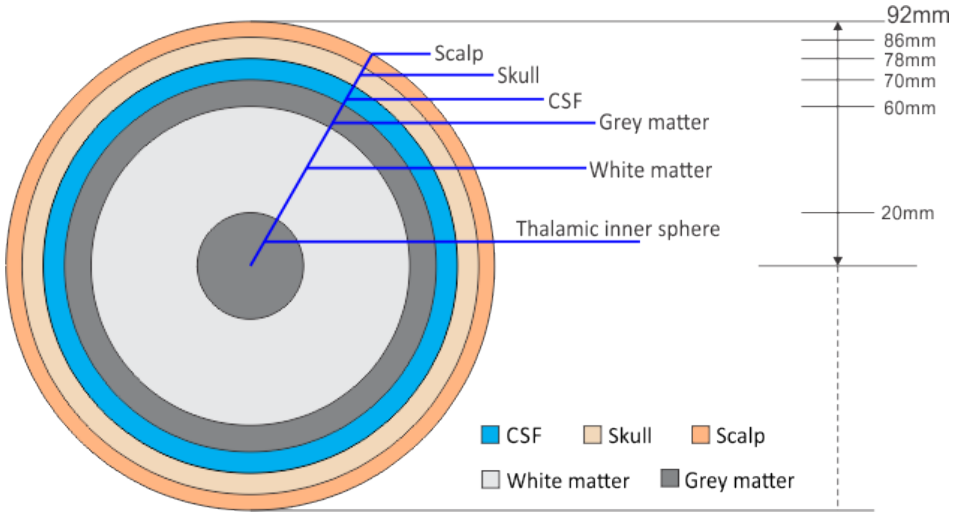

Figure 3.6: Spherical head model.

We select the isotropic conductivity values following the Table 4.1, (see section 4.1.1). Moreover, we set an anisotropic 9:1 radial/tangential ratio for the white matter, and a 1:10 radial/tangential ratio for the skull as suggested in [Wolters et al., 2006]. We apply rotational transformations to the local coordinate system for the anisotropic skull and white matter conductivity tensors, aiming to reorient the eigenvectors in a normal direction from the concentric spheres as carried out in [Hallez et al., 2008]. Finally, we use the GFDARM numerical technique to compare against the analytical anisotropic spherical solution introduce by [De Munck, 1988] (section 2.3.2).

3.2.2 Solving the sparse linear equation system

We test 8 different numerical solver combinations (NSC) comparing the *ghost-filling finite difference* (GFD) set up against the *fictitious domain* (FD). We consider two LES solvers, namely the baseline successive overrelaxation (SOR), and the biconjugate gradient stabilized (BiCG-Stab). First, we calculate solutions using SOR and

BiCG-Stab without preconditioning for both, GFD and FD. Then, we applied LU and iLU preconditioner for the GFD and also iLU and Fourier-Jacobi (FJ) preconditioners for FD as proposed in [Turovets et al., 2014] and following [Cuartas et al., 2015] using only the BiCG-Stab solver. Further we use the six layers spherical head model with $h = 3mm$ spatial resolution including anisotropic skull and white matter (Figure 3.6), setting a low relative residual $\varepsilon = 10^{-13}$ to analyze local minimum convergence with a maximum iterations $maxit = 800$. Both solvers (SOR and BiCG-Stab) where configure with 3 stop criterium, namely: reaching the desired relative residual within *maxit* cap; iterate *maxit* times without reaching ε; and two consecutive equal iterations.

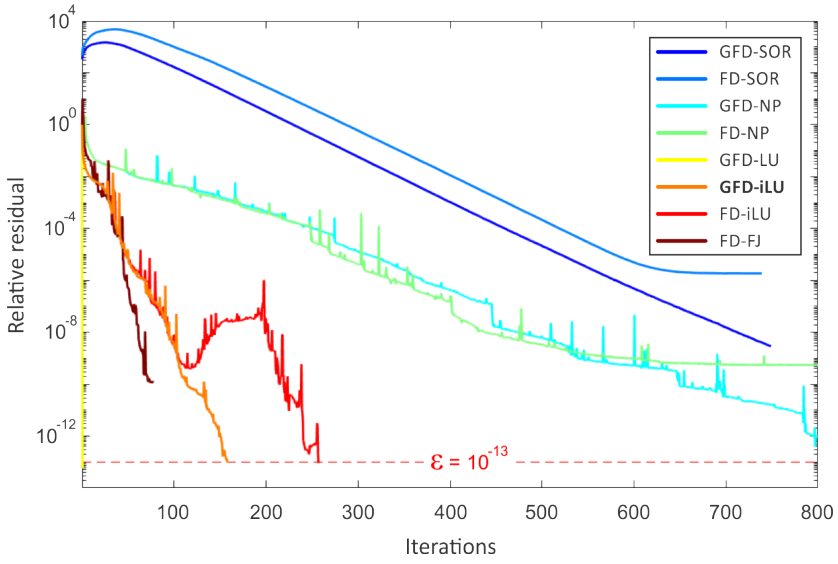

Figure 3.7: Relative residual convergence for the considered NSC's. Dashed red line stands for the selected minimal residual.

The Figure 3.7 shows the 8 proposed solver combinations performance, including a red dashed line for the $\varepsilon = 10^{-13}$ minimum residual cap. The Figure shows that the stationary SOR have a very smooth convergence rate, but it gets stanged after 700 iterations with two consecutive equal iterations without reaching ε, where we can appreciate a better convergence behavior for the GFD space with a lower final relative residual of 2.93×10^{-9} compared against the FD space reaching 1.87×10^{-6}. Additionally, the proposed preconditioners highly improve the convergence rate of the BiCG-Stab solver, however, FD-FJ reaches a minimum relative residual around 10^{-9} that is far from the imposed ε. In particular, only 3 NSCs reach the desired ε namely, GFD-LU, GFD-iLU y FD-iLU.

	Iterations	*Min residual*	*Iteration time*	*Solver time*	*Precond time*	*Total time*
GFD-SOR	750	3.07x10-9	0.0049	3.6622	-	3.6622
FD-SOR	740	1.87x10-6	0.0111	8.2405	-	8.2405
GFD-NP	797	3.89x10-13	0.0062	4.9626	-	4.9626
FD-NP	800	5.51x10-10	0.0131	10.4476	-	10.4476
GFD-LU	2	5.82x10-14	6.2081	12.4162	1460.8	1473.21
GFD-iLU	**158**	**9.53x10-14**	**0.0189**	**2.9917**	**0.0428**	**3.0345**
FD-iLU	257	9.2x10-14	0.0355	9.1287	0.0561	9.1848
FD-FJ	78	1.19x10-10	0.0414	3.2314	0.2978	3.5292

Table 3.1: Computational performance for different solver implementations.

In addition, we analyze the number of iterations, minimum residual reached, iteration time, total solver time, preconditioner computation time and the total time spend for the 8 proposed NSC's. Table 3.1 shows the test results, where we highlight the GFD-iLU as the best NCS for both, convergence and time. We can notice that the LU preconditioner using BiCG-Stab reach the desired minimum residual in only two iterations, however, the time spend to calculate LU is very high in comparison with FJ and iLU. Moreover, the computation time of LU factorization depends on the LES size, thus, for a lower spatial resolution, the estimation of the complete LU factorization is not affordable. Times reported in Table 3.1 where obtained in a `Intel Xeon CPU E5-2687W` computer with 64Gb RAM, using the Matlab software environment.

It is important to notice that the data variables for GFD include 129936 unknowns with a 1543212 non-zero values in the sparse coefficient matrix, and regarding FD, we have 238328 unknowns with 2297372 non-zero values coefficient matrix. This for the consider spherical head model and $3mm$ regular discretization resolution. In fact, the amount of data and unknowns for the FD is almost the double compared with GFD, this because FD includes not only the significant potential unknowns placed inside the volume conductor but also the potential unknowns for the air surrounding the volume.

	Unknowns	*Coef mat (Mb)*	*Prec iLU (Mb)*	*Prec FJ (Mb)*	*lead-pair (Mb)*	*Total Average (Mb)*
GFD	**129936**	25,128	28,173	-	**1,015**	54,316
FD	238328	37,758	43,344	33,155	1,862	82,965

Table 3.2: Memory allocation and number of unknowns.

Table 3.2 show the number of unknowns and the amount of memory use for $8-bytes$ double precision variables. Moreover, it is important to highlight that the *lead-pair*

memory allocation is crucial in a reciprocity solution, thus, the GFD shows a reduction of almost half of the memory needed to store a *lead-pair* compared to the FD.

3.2.3 Convergence analysis for GFDARM

We use the grid refinement method described in [Li et al., 2018], to analyze the convergence of the GFDARM numerical solution compared against the analytical spherical solution described in section 2.3.2. First, we set 112 electrodes in 6 geodesic rings evenly distributed over the spherical scalp surface as suggested in [Turovets et al., 2014] (see Figure 3.11(b)), obtaining the analytic solution $\boldsymbol{u}$ (see section 2.3.2) and the numerical solution $\boldsymbol{U}$ using the GFDARM method. Then we define the global error as the difference between the numerical and the analytical solution as $\boldsymbol{E} = \boldsymbol{U} - \boldsymbol{u}$. Thus, defining a ratio of error between two numerical solutions with different grid resolution approximations, we can estimate the convergence order as:

$$ratio = \frac{\|\boldsymbol{E}_h\|}{\|\boldsymbol{E}_{h/2}\|} \approx \frac{Ch^p}{C\,(h/2)^p} \approx 2^p \tag{3.18}$$

Where $\boldsymbol{E}_h$ is the error vector for a numerical solution $\boldsymbol{U}_h$ with a spatial resolution h, $\|\cdot\|$ is a norm distance, $C(h)^p$ is the global truncation error for h, and p is the estimated convergence order. From Eq 3.18, we can write:

$$p \approx \frac{\log\left(\|\boldsymbol{E}_h\| \,/\, \|\boldsymbol{E}_{h/2}\|\right)}{\log 2} \approx \frac{\log\left(ratio\right)}{\log 2} \tag{3.19}$$

Where p is an estimation of the convergence order, thus, to estimate p with Eq 3.19 we use two different norms for the vector $\boldsymbol{E}$, namely $E_\infty = \|\boldsymbol{E}\|_\infty = max\,\{e_i\}$, and $E_2 = \|E\|_2 = \left(\sum_i h_i \left|e_i\right|^2\right)^{1/2}$. Therefore, if $1 < p < 2$, the numerical solution is super-linear in the analyzed h space [Li et al., 2018].

In our experiment, we select five different spatial resolutions in potents of 2 ($h = [0.001, 0.002, 0.004, 0.008, 0.016]\,mts$) to analyse both, a fully isotropic medium and an anisotropic skull and WM medium using two different norms, namely E_2 and E_∞. Additionally, we set two different source positions, one in the GM and another in the TL area. Both source positions where select having surrounding voxels of the same tissue to avoid crossing a boundary Γ_l as suggested in [Hallez et al., 2008].

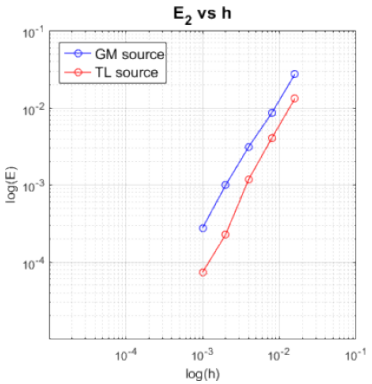

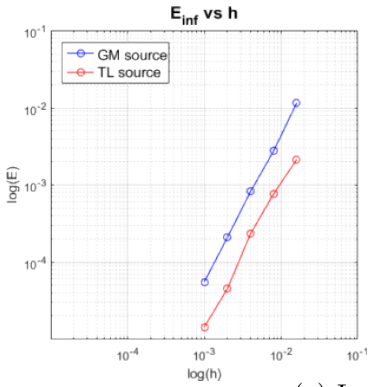

h	E_2 - GM	E_2 - TL	E_∞ - GM	E_∞ - TL
$p\left(\frac{h=0.001}{h/2}\right)$	1.8456	1.6326	1.9171	1.6530
$p\left(\frac{h=0.002}{h/2}\right)$	1.6584	2.3831	1.9738	2.3679
$p\left(\frac{h=0.004}{h/2}\right)$	1.4587	1.7772	1.7527	1.7192
$p\left(\frac{h=0.008}{h/2}\right)$	1.6728	1.7055	2.0718	1.4864
Average	1.6589	1.8746	1.9289	1.8066

(a) Isotropic

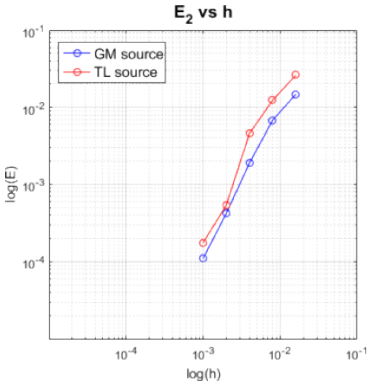

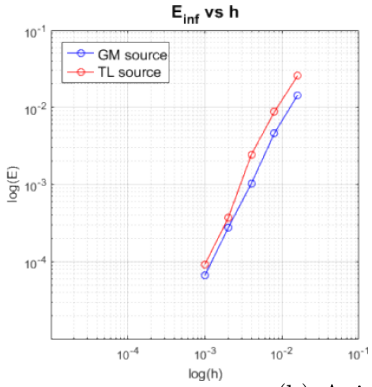

h	E_2 - GM	E_2 - TL	E_∞ - GM	E_∞ - TL
$p\left(\frac{h=0.001}{h/2}\right)$	1.9405	1.6178	2.0524	1.9924
$p\left(\frac{h=0.002}{h/2}\right)$	2.1692	3.0876	1.9080	2.7303
$p\left(\frac{h=0.004}{h/2}\right)$	1.8478	1.4332	2.1732	1.8516
$p\left(\frac{h=0.008}{h/2}\right)$	1.1180	1.0836	1.6426	1.5558
Average	1.7689	1.8056	1.9440	2.0325

(b) Anisotropic

Figure 3.8: Grid refinement analysis including on the left log-log charts showing the convergence rate with p slope, and, on the right, the values for the p estimation.

In the Figure 3.8 we show the results for the isotropic (top) and the anisotropic (button) mediums, using two different norms, namely E_2 (left) and E_∞ (right) in a logarithmic scale for both axes, including the numerical p estimation on the right. Each chart shows the global error for the GM and TL sources in the analyzed h space, showing always a superlinear approximation with $1 < p < 2$. Finally, the convergence analysis against an analytical solution shows second-order accuracy for all considered scenarios.

3.2.4 Stability analysis for the GFDARM linear system

Te so-called system matrix $\boldsymbol{A}$ is considered stable if $\|A^{-1}\| \leqslant \varepsilon$, for all $0 < h < h_0$, where ε and h_0 are two constants that are independent of h [Li et al., 2018]. Due to the sparse nature of the FDM system matrix we calculate the conditional number $C = \|\boldsymbol{A}\| \, \|\boldsymbol{A}^{-1}\|$, where $\boldsymbol{A}$ is the coefficient matrix of the linear system for both, FD and GFD to analyze stability following [Lin et al., 2017]. Furthermore, we consider 13 different spatial resolution, using the six layers anisotropic spherical head model (section 3.2.1) ($h = [0.003, 0.004, 0.005, 0.006, 0.008, 0.01, 0.012, 0.014, 0.016, 0.018, 0.02, 0.025, 0.03]\, mts$).

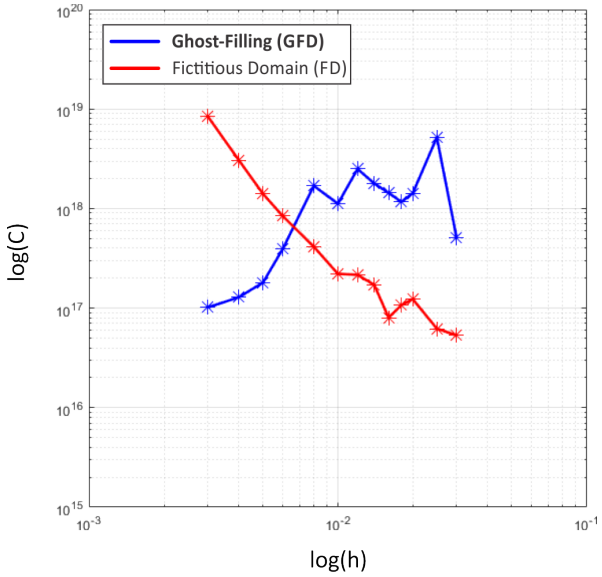

Figure 3.9: Conditional number.

Figure 3.9 shows the conditional number for the GFD and FD numerical spaces. The results show an exponential increase in the FD (red line) for smaller h values. In

comparison, the conditional number remains stable even for the minor considered h grid sizes for the GFD system matrix, showing stability in all considered resolutions.

We also investigate the stability of the GFDARM numerical solution adding random noise with uniform distribution ($\xi = [\text{ - } 1,1]$) to the excitation vector and the coefficient matrix of the LES. Thus, we analyze the sensitivity of the technique in a Montecarlo approach with 100 trials for every test using an anisotropic spherical head model with $h = 0.002mts$. Moreover, for the LES $\boldsymbol{A\phi}=\boldsymbol{\iota}$ we define the following test scenarios:

- Test A: Additive noise in the excitation vector

  $$A\phi = \iota_f + \eta\xi, \quad \text{where} \quad \iota_f(f) = \begin{cases} 0, & \forall f \neq \{f_+, f_-\} \\ 1+\eta\xi & f_+ \\ -1-\eta\xi & f_- \end{cases}$$

- Test B: Additive noise in the conductivity tensor eigenvalues

  $$A\left(\sigma_{noise}\right)\phi = \iota_f, \quad \text{where} \quad \sigma_{noise} = R\left(\lambda + \eta\xi\right)R^T$$

- Test C: Additive noise in the conductivity tensor eigenvectors and normalization of the eigenvector matrix

  $$A\left(\sigma_{noise}\right)\phi = \iota_f, \quad \text{where} \quad \sigma_{noise} = \overline{R}_\xi\left(\lambda\right)\overline{R}_\xi^T, \quad \text{and} \quad \overline{R}_\xi = \left(\overline{R+\eta\xi}\right),$$

  being $\overline{R}_\xi$ the normalized eigenvector matrix.

- Test D: Additive noise in the conductivity tensor eigenvectors and eigenvalues

  $$A\left(\sigma_{noise}\right)\phi = \iota_f, \quad \text{where} \quad \sigma_{noise} = R_\xi\left(\lambda + \eta\xi\right)R_\xi^T, \quad \text{and} \quad R_\xi = \left(R + \eta\xi\right)$$

We select 4 different values of noise power η for the normalized signal to noise ratios of $S/N = 10, 5, 3, 0$ obtaining a total of 1600 forward solutions for the 4 proposed tests, and the 4 different S/N. Furthermore, we used two different measures: the log Magnitude ($log(MAG)$) and Relative Difference Measure (RDM), to quantify the differences between a reference potential vector L_R without noise, and a tested potential vector L_T as in [Strobbe et al., 2014a, Schimpf et al., 2002, Meijs et al., 1989]. Moreover, $log(MAG)$ and RDM measures are defined as follows:

$$log(MAG) = ln\left(\frac{\|L_T\|_2}{\|L_R\|_2}\right) \tag{3.20}$$

$$RDM(L_R, L_T) = \left\| \frac{L_R}{\|L_R\|_2} - \frac{L_T}{\|L_T\|_2} \right\|_2 \tag{3.21}$$

The closer to 0 the $log(MAG)$ in Eq 3.20, or to 0 the RDM in Eq 3.21, the closer the *test* model L_T to the *reference* L_R model. Further, a large $log(MAG)$ measure, indicates very large values (unbounded) in the *test* potentials vector, similarly, a large RDM measure indicates a non-significant (close to zero) *test* potential vector norm.

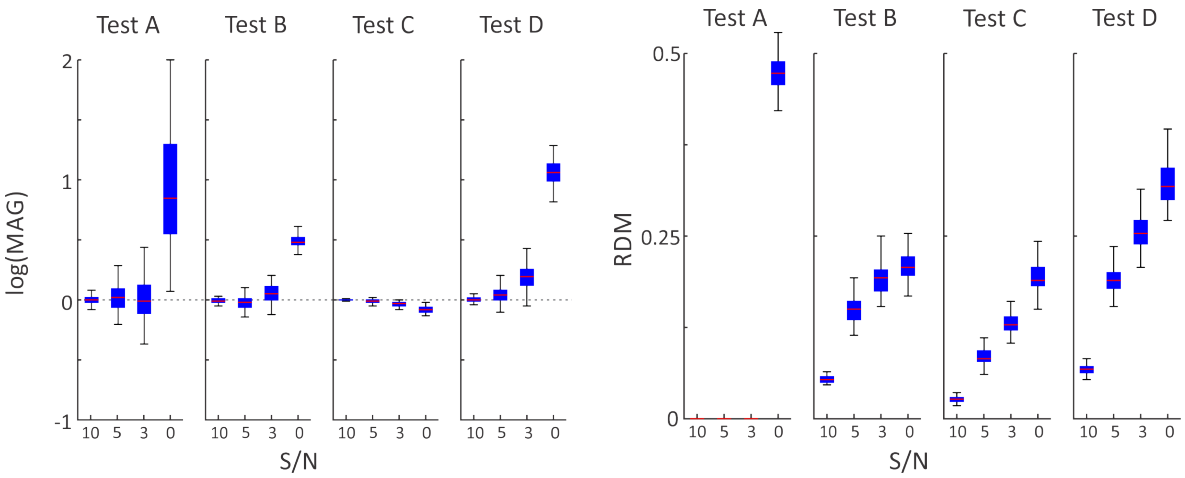

(a) ln(MAG) (b) RDM

Figure 3.10: Sensitivity analysis.

The Figure 3.10 includes the stability analysis results, showing in 3.10(a) the $log(MAG)$ and in 3.10(b) the RDM measures including the four proposed tests, and the considered S/N scenarios. The Figure shows blue bars for the 25% to the 75% percentile of the data total distribution (in dashed lines), including a red line for the mean value. The LES stability analysis results show a stable behaviour for the numerical proposed technique, even in the presence of high S/N definitions. Moreover, the numerical solution remains stable in all cases under consideration.

3.2.5 Validation: Analytical Vs Numerical spherical

For validation purposes, we use the six layers spherical head model with $h = 1mm$ grid size, setting a fully isotropic and an anisotropic skull and white matter mediums (section 3.2.1). We calculate the potentials over 112 electrodes to compare the proposed GFDARM and the analytical spherical solution placing a single source in the GM area with normal orientation to the GM surface boundary.

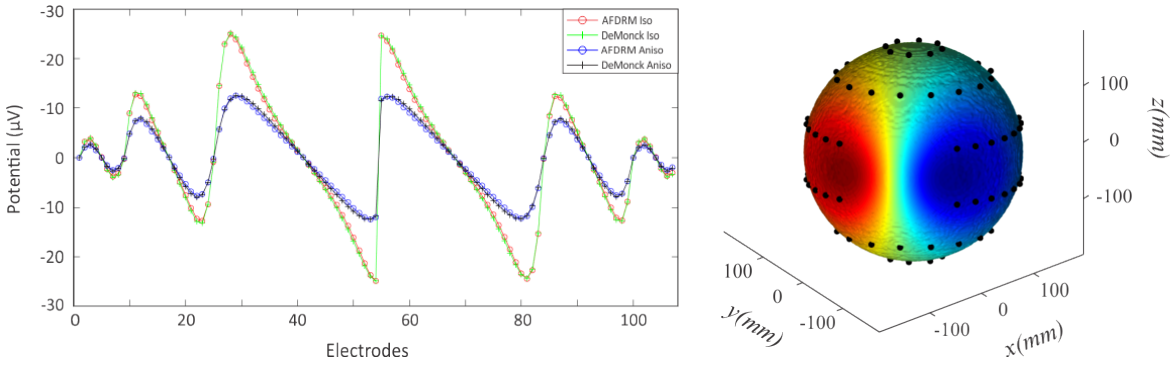

(a) Electrode potentials (b) Scalp potetial distribution

Figure 3.11: Numerical and analytical potentials for spherical head model.

Figure 3.11 shows the electrode potentials for the numeric and analytic solution using isotropic and anisotropic mediums illustrating a high correspondence between the numerical GFDARM potentials and the analytical solution for the Figure 3.11(a). We also illustrate the potentia distribution for the scalp surface in the anisotropic case Figure 3.11(b). Additionally, we select 300 random directions from the sphere volume center to the scalp surface, placing sources along each direction considering the voxel positions contained in the GM and TL areas following [Stenroos et al., 2012]. As a result, a total 8640 dipole sources were analyzed, considering the three orthogonal (X, Y, and Z) orientations for a total of 51840 forward calculations. Finally, we obtained the analytical and numerical potentials for the considered electrodes and dipole sources.

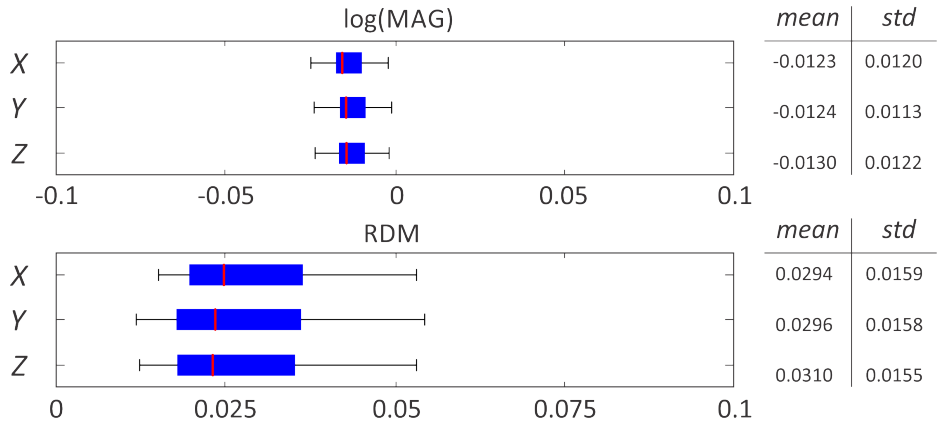

Figure 3.12: logaritmic Magnitude (*log(MAG)*) and relative difference measures (*RDM*).

The Figure 3.12 shows a box-plot graphic of the $log(MAG)$ and RDM measures for the 8640 comparisons in the three orthogonal directions. The blue box extends between the 25% and the 75% percentile of the data represented along the dashed black line, and the red line represent the median value. The results exhibit a very low standard deviation of the compared measures with mean values near to zero presenting a very high correspondence between the numerical and the analytical solutions for almost every source position or orientation.

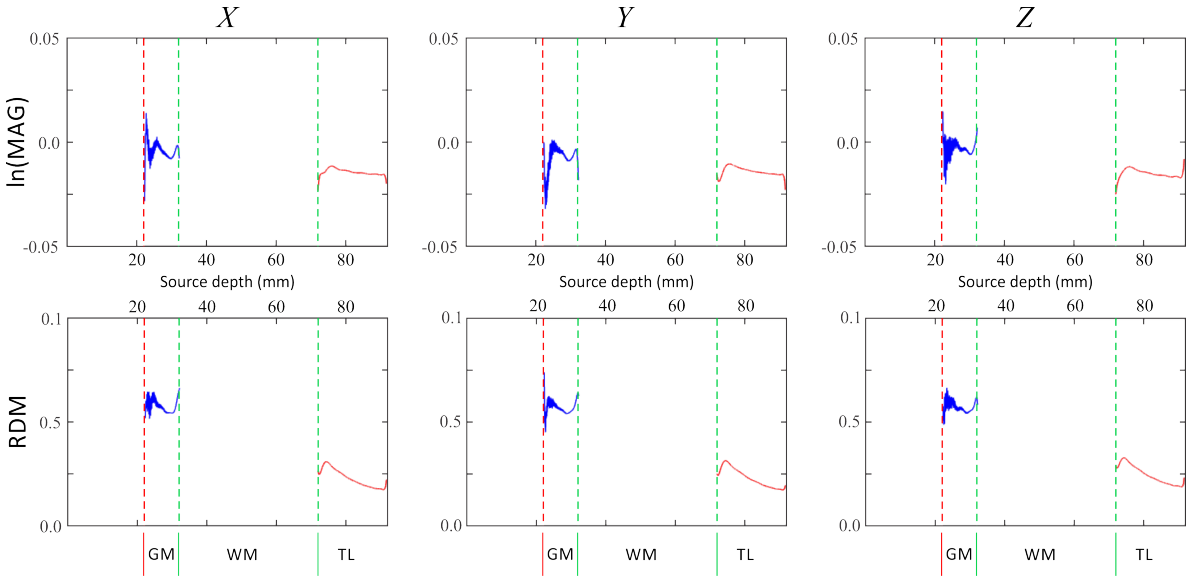

Figure 3.13: Source depth error behavior for the log(MAG) and RDM measures.

Additionally, Figure 3.13 shows the log(MAG) and RDM measures against the source depth for all the considered sources comparisons in the three orthogonal directions (X, Y and Z). In the Figure, we highlight the depth boundaries for the GM and TL where the sources were placed, with the WM in the middle area. Results show lower differences between the analytic and the numeric GFDARM technique for depth sources (in the TL area).

3.3 Discussion

We introduced a novel finite difference solution for the EEG forward problem applying the *ghost-filling* boundary approximation for the homogeneous Newman flux

condition, that we called ***ghost-filling* finite difference anisotropic reciprocity method** (GFDARM). Our method shows a coefficient matrix with improved stability and a linear equation system with fewer unknowns compared with the commune fictitious domain solution. Moreover, our finite difference solution based on the conservative form of the inhomogeneous anisotropic medium Poisson equation generates a symmetric, soft-diagonal sparse matrix that is stable for the considered discretization spaces, presenting superlinear convergence approximation with second-order accuracy. Furthermore, the introduced GFDARM allows the incorporation of voxel-wise conductivity information providing a direct adaptation of the technique to the available structural MR imaging without using previous head compartment tessellations like in FEM. Furthermore, our method is intrinsically built to consider conductivity anisotropy, which is essential to ensure correct modelling of current flow in the head.

3.3.1 GFDARM Linear Solver

The selection of the iLU preconditioner and BiCG-Stabilized solver takes advantage of the coefficient matrix properties for the proposed GFDARM solution, generating a fast, stable, convergent, and reliable numerical solution that can include voxel-wise anisotropic tensors, where results in section 3.2.2 show an improved convergence for the GFD-iLU compared to the previously used stationary SOR, and the FD-FJ solvers [Hallez et al., 2005, Turovets et al., 2014]. Moreover, GFD compared to FD solutions shows a better numerical behavior for all considered solver combinations, including the FJ circulant preconditioner used in [Turovets et al., 2014]. Furthermore, our results show a strong reduction of computational times for the proposed technique with fewer iterations (Table 3.1), considering also the reduction of the coefficient matrix size and the number of unknowns that directly reduce the storage memory requirements of the proposed GFD technique *lead-pairs* by half, compared with the commonly used FD (Table 3.2).

3.3.2 Numerical solution

The convergence grid refinement analysis show very consistent results with a superlinear approximation for two different norms applied to the global error vector obtained from the analytical solution [De Munck, 1988] and the proposed GFDARM numerical approximation for isotropic and anisotropic mediums (Figure 3.8). The results show superlinear approximation under all considered spatial resolutions for both considered

mediums. Thus, for the isotropic case, the results show an appreciably improved behavior for the deep TL source compared to the GM cortical source, however, this tendency is inverted for the anisotropic case, showing that when a source is surrounded by anisotropic tissue (from the WM) the numerical approximation have more error compared against a cortical source. Furthermore, we analyze the stability of the technique, estimating the conditional number for the coefficient matrix, thus, Figure 3.9 shows that the conditional number remains stable for a very wide range of grid resolutions, and tends to stabilize for the lower grid sizes values. Finally, we analyze the sensitivity of the linear equation system with four different tests considering different additive noise S/N factors, showing that the proposed numerical solution is stable and convergent for all tests under consideration.

3.3.3 Validation

The validation using a six layer spherical model including two different brain zones, namely GM and TL allow us to analyze deep sources surrounded by anisotropic WM and skull tissues. In comparison, other works consider simplistic spherical head models without taking into account anisotropic information [Vanrumste et al., 2001b, Lanfer et al., 2012, Turovets et al., 2014, Strobbe et al., 2014a]. Moreover, we set an exhaustive numerical comparison considering 8650 sources covering the GM and TL regions in the three orthogonal directions for a total of 51840 forward calculations. The results show a high correspondence between the analytical and the proposed GFDARM numerical solution (Figure 3.11), with a very low dispersion of the data for all the test under consideration (Figure 3.12).

3.3.4 Constraints and limitations

The volumetric anisotropic methods like the proposed GFDARM have increased complexity and computational burden compared against spherical approximations or numerical isotropic BEM techniques. A single isotropic lead-field calculation can take around $200s$, and for the anisotropic case estimation can take more than $400s$, this for the considered shperical head model holding $h = 1mm$ discretization step size. Moreover, in a reciprocity solution space, the memory needed to store the precalculated potential leads for the volumetric unknowns is very high, reching almost $3Gb$ as reported in Table 2.1. Finally, the GFDARM its constrained to sufficiently smooth boundaries between tissue compartments, and the computational time and memory allocation

needed is very high in comparison with the most used BEM technique as reported in Table 2.1.

Chapter 4

Forward volumetric modeling for realistic head data

The solution of the Poisson equation 2.1 for realistic free-form head volumes is only possible using numerical approximations [Irimia et al., 2013]. In particular, individual magnetic resonance (MR) and computed tomography (CT) images can be segmented into different tissue types, such as white and gray matter (WM/GM), cerebrospinal fluid (CSF), compact and spongy bone, skin, among others. Recently, diffusion-weighted imaging (DWI) has also been used to determine the anisotropy profile of brain structures based on the movement of water molecules [Le Bihan et al., 2012]. DWI is particularly important for modeling anisotropic properties in the WM. Moreover, anisotropic conductivity in the skull has also a large impact on the current flow from sources to sensors [Montes et al., 2013, Dannhauer et al., 2011].

The most simplistic numerical solution from neuroimaging real data is the boundary element method (BEM) [Ferguson et al., 1997] (see section 2.3.4). BEM method is widely used because of its low computational needs, however, most solutions only consider three surface boundaries (scalp, skull, and brain), and is restricted to isotropic conductivities. In this sense, several works analyze the influence of neglecting the human head anisotropy tissues in the ESI techniques [Cuartas et al., 2017b, Montes et al., 2016, Ziegler et al., 2014, Wendel et al., 2009, Wolters et al., 2006]. Particularly there are two decisive factors that expose the need for volumetric and realistic forward models, the first one is the strong anisotropic behaviour of the skull and white matter (among others tissues like the thalamic areas) due to the direct impact on ESI accuracy [Strobbe et al., 2014a], and, the patient-specific analysis

with multiple tissues definition that drastically reduce the errors of using spherical approximations or general atlas [Vorwerk et al., 2014, Vallagh et al., 2007].

There are two main methodologies that can handle anisotropic conductivities and realistic patient-specific analysis, namely, Finite Element Method (FEM) [Wolters et al., 2002, Liu et al., 2005], and Finite Difference Method (FDM) [Vanrumste et al., 2001b, Hallez, 2009]. The main practical limitation of FEM and FDM in comparison with BEM is the computational burden, where the solution leads to linear systems, and the system matrix is typically sparse and has a large number of unknowns in comparison with BEM. Nevertheless, significant advances in computing capabilities have made it possible to calculate and use volumetric forward techniques like FDM [Vorwerk et al., 2018, Turovets et al., 2014, Volkov et al., 2009]. In this chapter, we will introduce a framework to build patient-specific high-resolution anisotropic head models, using the GFDARM technique.

4.1 From neuroimaging to realistic forward head models

Advances in magnetic resonance imaging (MRI) have made it possible to extract detailed information about structural properties of the head, which can be used to build more detailed and anatomically realistic head models. Moreover, conductivity anisotropy in the WM can be estimated across voxels by combining information from DWI and MRI images. Further, nowadays, it is common practice to assign conductivity values extracted from the literature to each segmented tissue [Michel et al., 2012, Liu et al., 2017]. Alternative solutions as the electrical impedance tomography have been developed [Malony et al., 2011]. These solutions, however, are computationally intensive and only estimates average conductivity values for pre-segmented tissues, rather than providing a conductivity value for each location in the head. Preliminary work using MRI has shown encouraging results for mapping low-frequency electrical properties of head tissues [Michel et al., 2016]. If the necessary developments take place, MR-based conductivity mapping may become a state-of-the-art technique for the construction of realistic head models for EEG applications, opening the need of a forward volumetric modeling technique that allows across-voxel conductivity definitions.

Figure 4.1 shows an example of MRI/CT neuroimage data segmented into a $5-$layers head compartment model. Included tissues are scalp, skull, CSF, WM and GM.

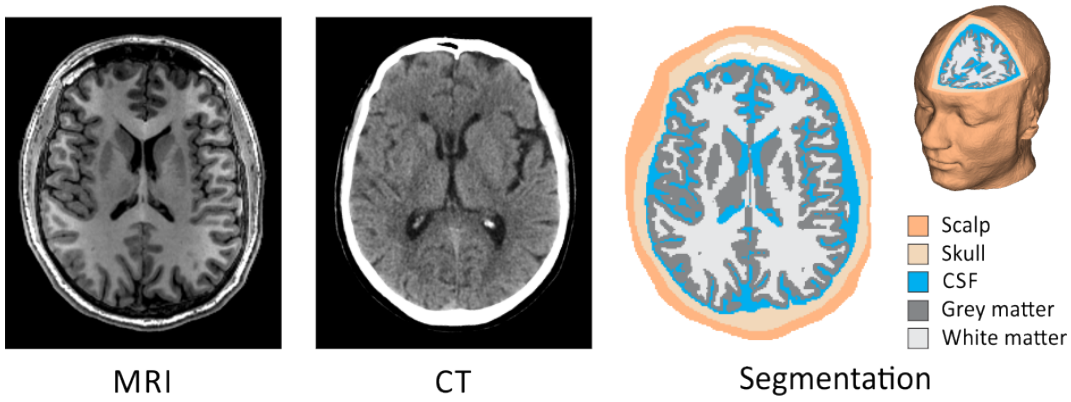

Figure 4.1: MRI/CT 5−layers neuroimage segmentation.

The segmentation was made with *FreeSurfer* software (https://surfer.nmr.mgh.harvard.edu/) providing interfaces Γ_l between different tissues, and boundary $\partial\Omega$ separating the head volume domain Ω from the surrounding air. Segmentation methods are commonly based on probabilistic atlas including information about the distribution of most known tissues of the human head. Most free use neuroimaging software have unsupervised routines to segment patient-specific MRI's [Yazdani et al., 2015, Balafar et al., 2010].

4.1.1 Head tissue conductivities

From the segmented neuroimages, each layer is assigned with known conductivity values from the literature. In addition, for anisotropic tissues modeling, is necessary to define the main direction of the conductivity tensor eigenvectors, and also its eigenvalues. The most influence anisotropic tissues in the human head regarding the ESI task are the skull and WM [Dannhauer et al., 2011, Marin et al., 1998, Bashar et al., 2008a, Gullmar et al., 2010]. Furthermore, we refer to the specific methods for the anisotropy modeling in section 4.2.

Table 4.1 show the considered isotropic conductivities for this work (last column), taking into account multiple previous ESI studies [Wolters et al., 2006, Montes et al., 2013, Vorwerk et al., 2014] and including also the IT'IS Foundation database holding a large list of low frequency tissue conductivities [Gabriel, 1993, IT'IS, 2016]. Magnitudes are given in Siemens per meter (S/m).

Compartment	[Wolters et al., 2006]	[Montes et al., 2013]	[Vorwerk et al., 2014]	[Gabriel, 1993]	**Selected**
Skin	0.3300	0.3279	0.4300	-	0.4300
Skull	0.0042	0.0105	0.0100	-	0.0105
CSF	1.7900	1.7857	1.7900	1.7800	1.7900
GM	0.3300	0.3300	0.3300	0.2390	0.3300
WM	0.1400	0.1428	0.1400	0.1280	0.1400
Muscle	-	-	-	0.3550	0.3550
Fat	-	-	-	0.0573	0.0573
Eyes	-	-	-	1.5500	1.5500
Vessels	-	-	-	0.2800	0.2800

Table 4.1: Considered head tissue isotropic conductivities (S/m).

4.1.2 Realistic patient-specific neuroimage head model (RHM)

We build a realistic, high-resolution, patient-specific volume conductor model from neuroimages, including anisotropic skull and white matter modeling. Further, we use T1, IDEAL T2 and diffusion-weighted imaging (DWI) MR scans acquired from a healthy 32-years-old male (me) in the Rey Juan Carlos University, Medicine Faculty, Medical Image Analysis and Biometry Lab, Madrid, Spain.

Acquisition

MRI data were collected on a 3T MR scanner (General Electric Signa HDxt), using the body coil for excitation and an 8-channel quadrature brain coil for reception. Imaging was performed using an isotropic $3DT1w$ SPGR sequence under the following parameters: TR=8, $7ms$, TE=$3.2ms$, TI=$400ms$, NEX=1, acquisition FOV=$260mm$, $matrix$=320 × 160, resolution $1 \times 1 \times 1mm$, flip angle 12; an IDEAL $T2$ sequence with TR=$3000ms$, TE=$81.9ms$, NEX=6, FOV=$260mm$, acquisition matrix 320×160, flip angle 90; a Time of Flight (TOF) sequence consisting of 8 volumes with 6 slices overlap and TR=$20ms$, TE=$2.1ms$, NEX=1, acquisition FOV=$224mm$, matrix 224×224, resolution $1 \times 1 \times 1mm$, flip angle 15; and a DWI sequence with TR=$9200ms$, TE=$83.8ms$, TI=$0ms$, NEX=1, acquisition FOV=$240mm$, matrix 100×100, flip angle 90, directions 45, thickness $2mm$.

Segmentation

Image preprocessing was performed using 3D Slicer built-in modules [Kikinis et al., 2014]. The preprocessing steps included: MRI bias correction (N4 ITK MRI bias correction), and Registration (BRAINS) for movement correction. Cortical Segmentation, including brain white matter (WM) gray matter (GM), and cerebrospinal fluid (CSF), was performed in the T1-weighted volume using *FreeSurfer* [Fischl et al., 2002]. The skull was estimated using a multi-atlas and label fusion-based approach [Torrado et al., 2016]. To this end, we applied to a CT database the Simultaneous Truth and Performance Level Estimation (STAPLE) algorithm [Warfield et al., 2004]. The remaining CSF was computed as the residual of the skull and the brain segmentation using a GNU Octave script. To segment the skin we use the background noise variance and thresholds of the anisotropically filtered volume as in [Torrado et al., 2014]. Then, Gaussian smoothing was applied to reduce aliasing artefacts in the skin surface and to ensure a minimum of 2 voxels thickness for the skin volume. The eyeballs were segmented by applying a threshold and edge detection algorithm to the IDEAL in-phase head sequences. We also performed a smooth approximation of the main arteries by using an expectation-maximization algorithm to the median filtered TOF images. The remaining tissue was classified in muscle and fat/cartilage, using the expectation-maximization algorithm on the IDEAL fat and water images [Cuartas et al., 2017b].

Finally, all available data (T1, T2, and DWI) was aligned with a voxel similarity-based affine registration procedure to correct subject orientation and geometrical distortions. Then, all registered DWI data were re-sampled to have a unique size $1\times1\times1mm$ by using the FSL toolbox [Jenkinson et al., 2012]. The final head model is shown in Figure 4.2 holding 9 different tissues namelly: skin, skull, CSF, GM, WM, muscle, fat, eyeballs and vessels, including also a $1mm^3$ DWI. Furthermore, we refer to this dataset as realistic head model (RHM). Figure 4.2, shows a 5-layer, and a 9-layer segmentation for the RHM model.

4.2 Modeling tissue conductivity anisotropy

Anisotropic behavior is important in conductivity head modeling and even more in ESI solutions. First anisotropic measures for EEG current propagations in head volumes was found by [Rush et al., 1968]. In this regard, several works

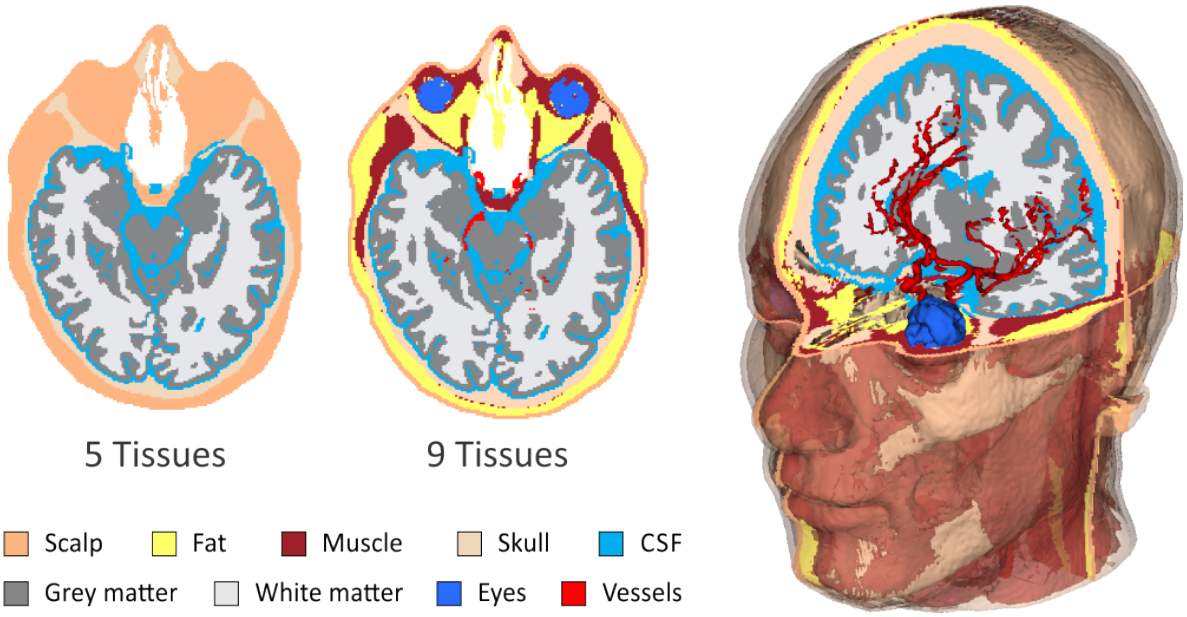

Figure 4.2: RHM segmentation.

study the anisotropic behaviour of specific tissues in the human head as the skull [Montes et al., 2016, Lanfer et al., 2012, Cuartas et al., 2014b] and the white matter [Wolters et al., 2006, Cuartas et al., 2014a, Hallez et al., 2008]. In a realistic head model, tissue conductivities must be modelled both isotropically and anisotropically depending on the tissue. In the first case, the conductivity tensor is defined as $\mathbf{\Sigma} = \sigma_{\text{iso}} I_3$, where I_3 is the 3×3 identity matrix, and σ_{iso} is the isotropic conductivity value from 4.1 for a specific tissue. For the anisotropic case, we must adequately define eigenvectors and eigenvalues to assemble voxel-wise anisotropic tensors for specific tissue/regions in the head volume. Anisotropic mathematical tensor is introduced in section 2.2.3.

Figure 4.3 illustrate the morphology of the WM and skull tissues anisotropy. In the skull case 4.3(b), the tissue region is shaped by two different types of bone (hard and spongy) in a 3-layered distribution. Hard bone has very low conductivity ($0.0064 S/m$), in comparison with the spongy bone ($0.02865 S/m$). Skull tissue is formed by a spongy area enclosed between two hard bone sections generating a local anisotropic behaviour in the skull compartment, having low conductivity in the normal direction of the skull surface and larger conductivity in the tangential plane as shown in 4.3(b).

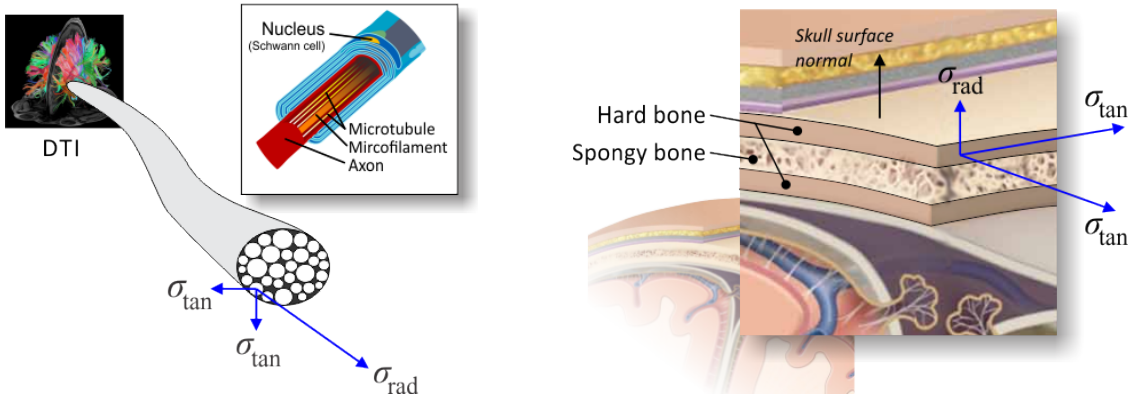

(a) WM anisotropy (b) Skull anisotropy

Figure 4.3: Skull and WM tissue anisotropy morphology.

Similarly, WM is formed by nerve bundles (groups of axons) connecting cortical grey matter in distant areas 4.3(a). Moreover, nerve bundles in WM are often aligned parallel to each other. Water and ionized particles can move more easily along the nerve bundle than in perpendicular direction. Therefore, the conductivity along the nerve bundle is measured to be nine times higher than in the perpendicular to it. Further, water diffusion (mobility) can be estimated using DWI, and, in particular, WM local anisotropy conductivity share eigenvectors with diffusion tensor imaging (DTI) that can be obtained form DWI registers [Basser et al., 1994]. Figure 4.3(b) shows a WM tract axon containing microtubule and microfilament formations restricting the water mobility to the longitudinal/radial direction of the tracts bundles.

4.2.1 Modeling the skull conductivity anisotropy

Anisotropy on the skull depends on its morphology, thus, the conductivity is knowing to be larger in the tangential direction and smaller in the normal direction of the skull surface [Montes et al., 2013, Lanfer et al., 2012, Pohlmeier et al., 1997], therefore, we calculate the anisotropic skull conductivity estimating the local voxel eigenvectors from a smooth mesh that holds an adequate approximation of the local normal directions to the skull surface following [Wolters et al., 2006, Marin et al., 1998].

Estimating the tensor eigenvectors: We estimated a skull surface mesh using the 3D Slicer built-in *model-maker* module including the marching cubes and spatial

smooth filtering routines [Kikinis et al., 2014]. Additionally, we use the *MeshLab* to eliminate redundant vertex and closed faces, applying a local hole filling algorithm to close holes in the final mesh [Janaszewski et al., 2010]. Then, we performed an affine transformation between the mesh and the head volume, ensuring that all the vertex normals in the mesh have a corresponding single voxel in the skull volume. After this, we guarantee that all directions are pointing outside the head. To this end, we create radial vectors between the middle point of the grey matter and every single skull voxel. Then, we compute the dot product between such radial vector and the mesh normal associated with a voxel, and, if the result is negative, the normal direction is inverted. This procedure is repeated for all the skull voxels comprising normal vectors from the skull mesh. Finally, we iteratively propagate the available normal vectors using interpolation to obtain the eigenvectors of the skull voxels that not have an associated normal. The Fig 4.4 show the considered steps to estimate the volume normals from the skull mesh. The figure also shows the iterative propagation process where the normal vectors are interpolated to the entire skull volume.

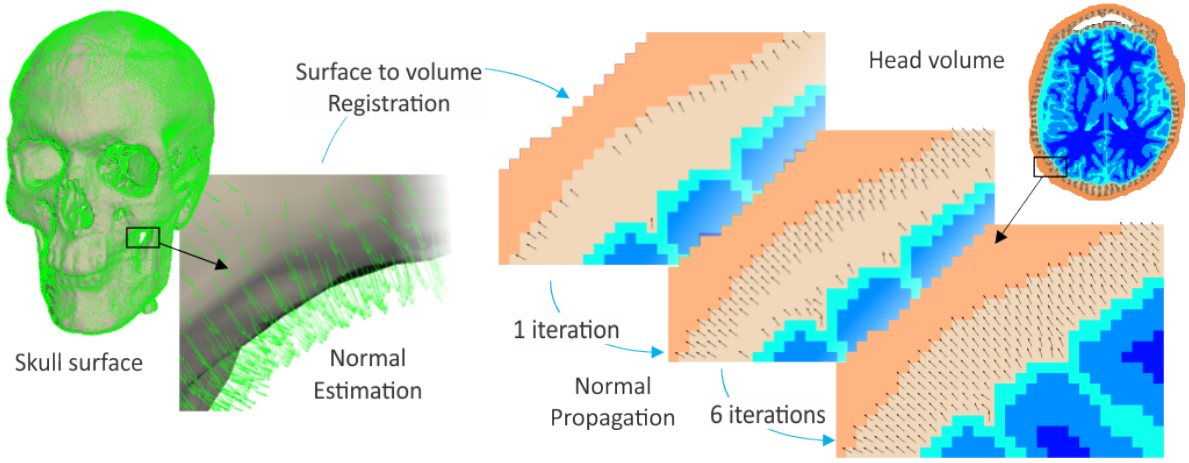

Figure 4.4: Skull anisotropy eigenvectors estimation, illustrating the mesh normal propagation in the head volume after six iterations.

Defining the tensor eigenvalues: Finally, to establish the skull conductivity eigenvalues, we use the spherical volume constraint defined as follows [Wolters et al., 2006]: $\sigma_{\text{rad}}(\sigma_{\text{tan}})^2{=}\sigma_{\text{iso}}^3$, where $\sigma_{\text{rad}}{\in}\mathbb{R}^+$ and $\sigma_{\text{tan}}{\in}\mathbb{R}^+$ are the conductivity values of the radial and tangential directions, respectively. $\sigma_{\text{iso}}{\in}\mathbb{R}^+$

is the isotropic conductivity value from Table 4.1. We used a small radial to tangential anisotropic ratio as suggested in [Montes et al., 2016], fixing the isotropic skull conductivity as σ_{iso}=0.0105 S/m and skull ratio to 1:1.82 (radial:tangential) obtaining σ_{tan}=0.0123S/m and σ_{rad}=0.007S/m.

4.2.2 Modeling white matter conductivity anisotropy

Contrary to the skull, anisotropy in the white matter cannot be estimated from the tissue morphology. Thus, we use diffusion tensor imaging (DTI) data to determine the conductivity tensors in the WM compartment.

From DWI to DTI: DWI data are re-sampled to have the same $1mm^3$ resolution of the T1 and T2 segmented sequences. Afterwards, motion, eddy currents, and field inhomogeneities are removed. Later, the diffusion tensor images (DTI) are estimated using the Diffusion-Toolkit from the 45 gradient directions of the DWI [Le Bihan et al., 2001, Westin et al., 1999]. Finally, the DTI data are co-registered to the anatomical T1 image space. All procedures are carried out using the FSL tool [Jenkinson et al., 2012].

From DTI to local conductivity tensors: Early works assume a strong 9 : 1 radial to tangential anisotropic constant ratio [Wolters et al., 2006, Hallez et al., 2007a]. However, recent studies show that the eigenvalues from the DTI better describe the anisotropic behavior of the WM [Vorwerk et al., 2014]. Thus, we estimate the conductivity tensors $\boldsymbol{\Sigma}_{\boldsymbol{WM}}^{(j)}$ from the diffusion tensors $\boldsymbol{D}^{(j)}\in\mathbb{R}^{3\times3}$ using a local linear relationship $\boldsymbol{\Sigma}_{\boldsymbol{WM}}^{(j)}=s_j\boldsymbol{D}^{(j)}$, as suggested in [Tuch et al., 2001] and [Vorwerk et al., 2014]. Furthermore, the scalar factor s_j can be obtained as follows:

$$s_j = \frac{\sigma_{WM}^{iso}}{(\lambda_1\lambda_2\lambda_3)^{1/3}}, \tag{4.1}$$

where $\sigma_{WM}^{iso} = 0.14S/m$ is the isotropic conductivity value for the white matter, and λ_1, λ_2, and λ_3 are the eigenvalues of the local tensor $\boldsymbol{D}^{(j)}$.

The Figure 4.5 illustrates the procedure to obtain the local anisotropy conductivity tensors $\boldsymbol{\Sigma}_{\boldsymbol{WM}}^{(j)}$ in the WM, showing the volume constrain depending on the DTI eigenvalues.

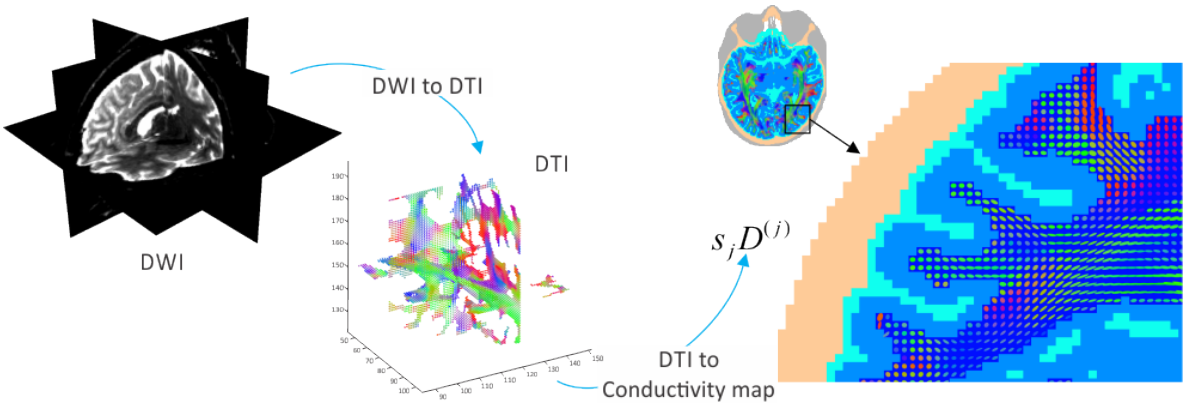

Figure 4.5: White matter anisotropy estimation process in two stages: First, we performed the transformation from DWI to DTI, and then, we estimate the local scaling factor s_j using a volume constraint to transform the DTI to the conductivity tensor.

4.2.3 From EEG to volume electrode positions

The placement fo the EEG electrodes in the volumetric forward model is also crucial for ESI solutions. A one to one relationship between the dipole localization errors and the average displacement of the electrode positions in the head conductor volume using ESI techniques is reported by [Van Hoey et al., 2000]. Thus, accurate modeling of the electrode positions on the scalp surface is essential in forward modeling and positions directly related to the field propagation of the brain sources [Strobbe, 2015].

Recent works introduce automatic labeling, detection and positioning of hdEEG arrays [Liu et al., 2018, Marino et al., 2016].Moreover, most of the EEG databases include three-dimensional maps of the electrodes used for the study. Thus, we performed fiducial-based similarity transformations to align the EEG electrodes to the head volume. Finally, we project each electrode position towards the center direction of the head volume to ensure that the electrode is surrounded by scalp voxels, guaranteeing that the electrode voxel is not surrounded by air as suggested in [Hallez et al., 2009] and following our own constrain for *ghost-filling* stating that sources must lie inside the head volume ($\iota_f|_{\partial\Omega} = 0$) (section 3.1.3) when applying reciprocity.

4.2.4 EEG Forward Problem

After segmentation labeling, and local anisotropic conductivity tensors estimation, we proceed to solve the EEG forward problem in a reciprocity setup for a given electrode configuration using the GFDARM technique.

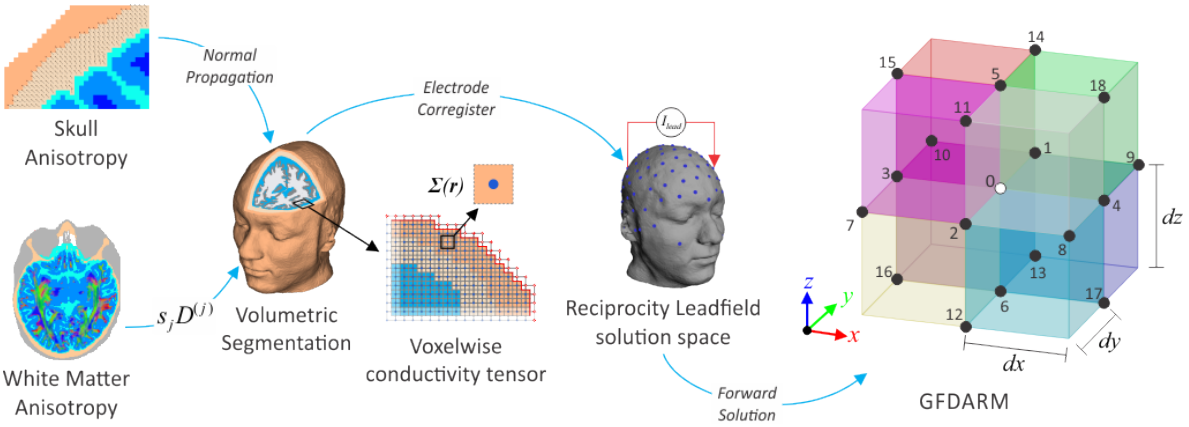

Figure 4.6: Forward anisotropy modeling: The Figure illustrates from left to right the anisotropy in the skull and withe matter estimation that are included in the volumetric segmentation. The solution is carried out in a voxelwise conductivity framework for a *lead-field* reciprocity space of a corregistered electrode data set. Finally, forward calculations are carrier out using the GFDARM algorithm.

Figure 4.6 shows the proposed realistic head modelling methodology pipeline. Thus, from left to right, we illustrates the anisotropic skull (see section 4.2.1) and WM (see section 4.2.2) procedures, assembled into the neuroimage tissue-labelled segmentation (see section 4.1.2), allowing a voxelwise anisotropic conductivity distribution that can be isotropic or anisotropic taking known conductivity parameters from the literature (see section 4.1.1). Moreover, from the conductivity model, we define a reciprocity solution space for a given three-dimensional electrodes map that is co-registered to the scalp (skin) segmentation volume (see section 4.2.3). Finally, we perform forward calculations using the proposed GFDARM solution (see section 3.1) in a reciprocity space (see section 3.1.6) to obtain the potential propagation for any given source moment or positioning inside the head volume.

4.3 Parametric inverse solution

In a reciprocity space with N_E electrodes, we can calculate the electrode potentials V_E for a given dipole moment $\mathbf{d}$ and position $\boldsymbol{r}$ using Eq 3.17 (see section 3.1.6). Furthermore, a parametric inverse solution can be estimated for a reference head model with electrode potentials V_R, compared against a tested head model with electrode potentials V_T, using the same electrode reciprocal space [Vanrumste et al., 2000]. Thus, we can estimate the pairwise dipole parameters $(\tilde{\boldsymbol{r}}, \tilde{\mathbf{d}})$ that best fit the reference potentials $V_R(\boldsymbol{r}, \mathbf{d})$ by calculating the potentials, $V_T(\tilde{\boldsymbol{r}}, \tilde{\mathbf{d}})$ in a minimization parametric relative residual energy (RRE) function as follows:

$$RRE = \min_{(\tilde{\boldsymbol{r}}, \tilde{\mathbf{d}})} \left\{ \frac{\left\| V_R - V_T\left(\tilde{\boldsymbol{r}}, \tilde{\mathbf{d}}\right) \right\|^2}{\|V_R\|^2} + C\left(\tilde{\boldsymbol{r}}\right) \right\} \tag{4.2}$$

Where $V_R \in \mathbb{R}^{N_E \times 1}$ are the electrode potentials of the reference model, usually the most realistic or complex head model. $V_T\left(\tilde{\boldsymbol{r}}, \tilde{\mathbf{d}}\right) \in \mathbb{R}^{N_E \times 1}$ are the electrode potential of a tested model, that must be iteratively recalculated to minimize the Eq 4.2. Additionally, the term $C\left(\tilde{\boldsymbol{r}}\right) \in \mathbb{R}^{+}$ is a penalization parameter that is set to zero for $\boldsymbol{r}$ positions inside the gray matter, and it's very large otherwise. Moreover, notation $\|\cdot\|$ stands for the Euclidean norm. Thus, Eq 4.2 can be solved using the nonlinear unconstrained optimization Nelder-Mead simplex method [Nelder et al., 1965, Lagarias et al., 1998].

Solving the Eq 4.2 for a single dipole from the reference model $(\boldsymbol{r}, \mathbf{d})$, we obtain a single dipole from the test model $(\tilde{\boldsymbol{r}}, \tilde{\mathbf{d}})$ that can be compared to obtain the dipole localization error (DLE) using positions $\boldsymbol{r}$ and $\tilde{\boldsymbol{r}}$ as follows:

$$DLE = \left\| \hat{\boldsymbol{r}} - \boldsymbol{r} \right\|_2 \tag{4.3}$$

And the dipole orientation error (DOE) for the dipole moments $\mathbf{d}$ and $\tilde{\mathbf{d}}$ as follows:

$$DOE = \cos^{-1}\left(\frac{d}{\|d\|} \cdot \frac{\tilde{d}}{\left\|\tilde{d}\right\|} \right) \tag{4.4}$$

Furthermore, we use Eq's 4.3 and 4.4 to compare numerical head models in the reciprocity space.

4.4 Experiments and results

4.4.1 Influence of the anisotropic modeling in the potential fields propagation

We used the 5-layer RHM (see section 4.1.2, Figure 4.2), placing a single dipole in the GM area oriented along the negative Y orthogonal axis. Then, we calculate reciprocity forward solutions using GFDARM and a 128 biosemi electrode distribution, considering two head models, a fully isotropic medium and an anisotropic skull and white matter medium.

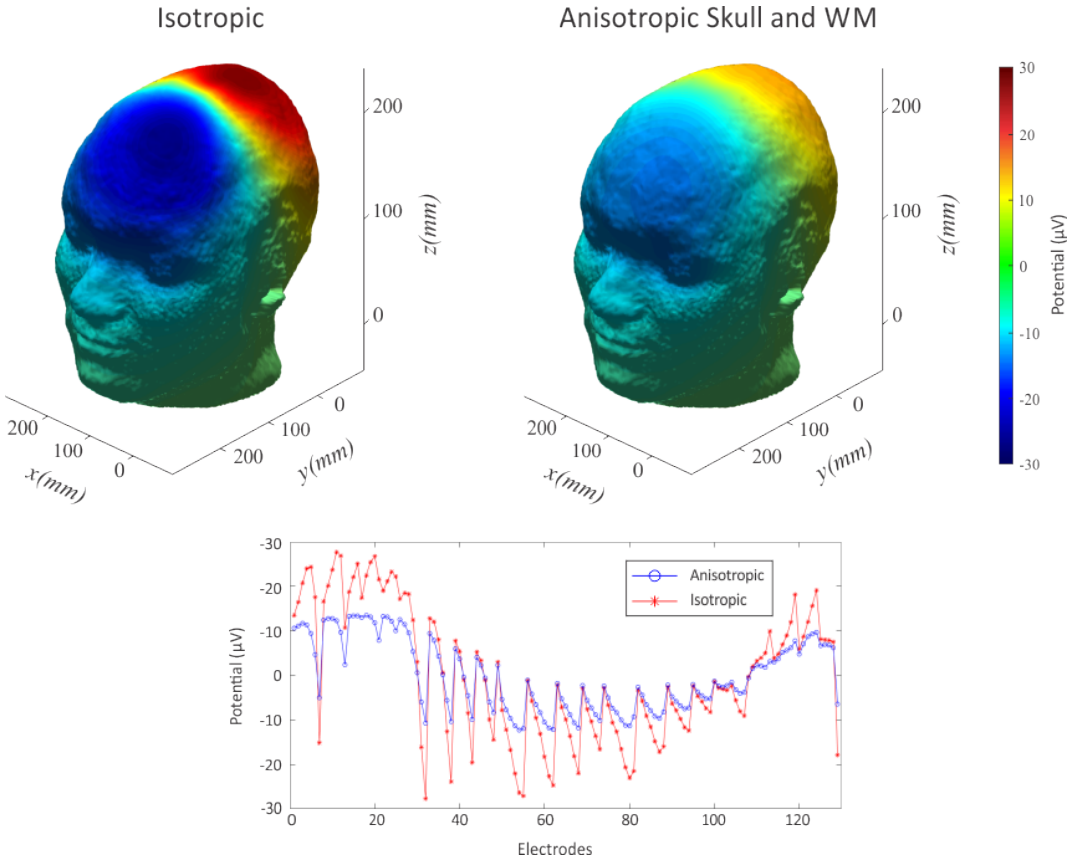

Figure 4.7: Scalp potentials for a single dipole placed in the central motor area of the GM oriented horizontaly (negative Y direction).

The Figure 4.7 shows the scalp potential distribution for both, the isotropic (top-left) and the anisotropic medium (top-right), and also the electrode potentials (button)

for the reciprocity solution. Results show significant differences not only in the scalp potentials intensity but also in the potential distribution along the scalp surface, where the maximum value appears in a translated position towards the frontal area of the head for the anisotropic medium. Moreover, we show the electrode potentials for the isotropic (blue line) and the anisotropic (red line) mediums. The Figure 4.7 shows significant differences in the amplitude between both considered models, with a substantial attenuation for the electrode potentials in the anisotropic case.

Additionally, we analyze the differences in the equipotential propagation lines in a non-reciprocal setup, to study the electric field propagation for the considered head models.

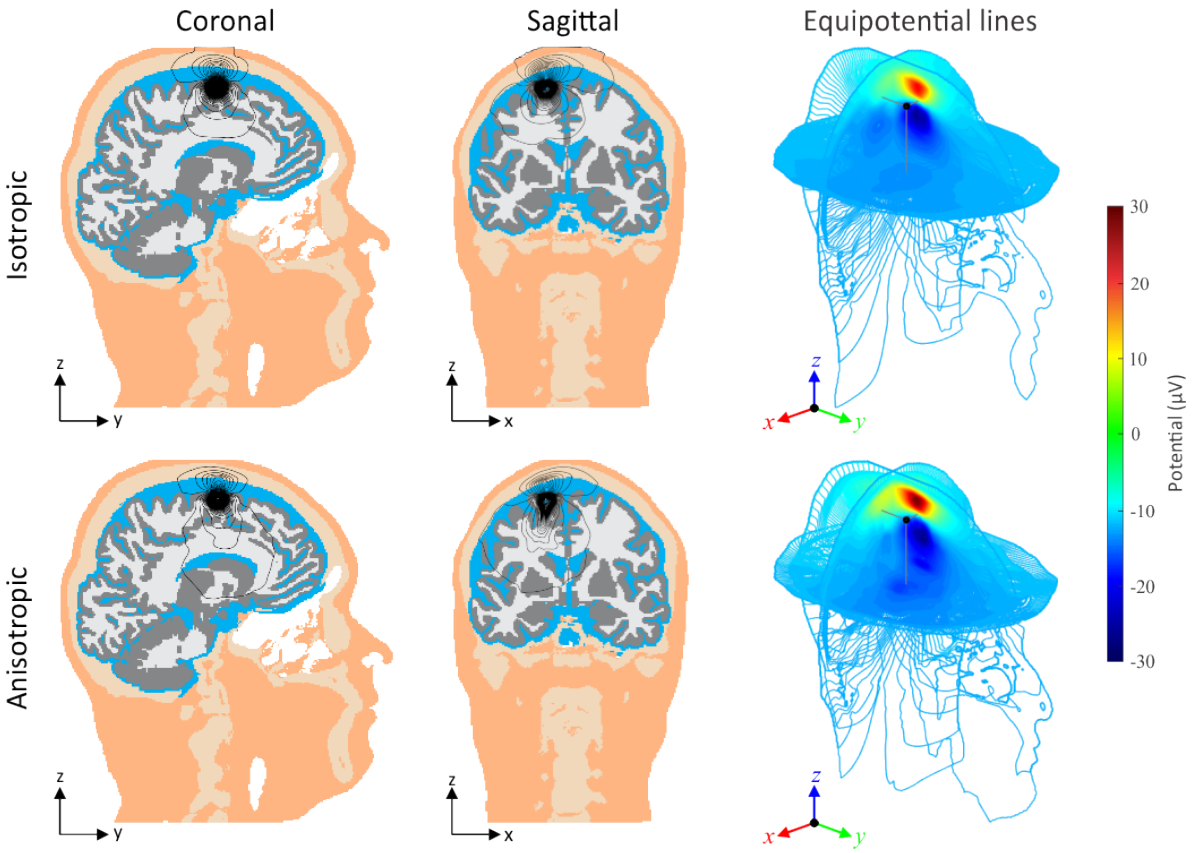

Figure 4.8: Sagittal, coronal and tridimensional views of the equipotential lines propagation from a single dipole in the GM, for both, a full isotropic model (top) and an anisotropic skull and WM model (button).

Coronal and sagittal views are included in Figure 4.8 to illustrate the potentials propagation of a single dipole with normal orientation concerning the GM cortical-motor area (positive Z orthogonal direction). Moreover, we show a three-dimensional render of orthogonal planes containing the equipotential distribution for the considered source represented in the Figure 4.8 as a black dot. The results show essential differences in the equipotential lines between isotropic and anisotropic mediums. Further, for the isotropic case, the lines are smooth, and the electric fields easily reach the scalp surface due to the homogeneity in the skull compartment conductivity. In comparison, for the anisotropic medium, the equipotential lines tend to align with the local anisotropy eigenvectors, showing irregular patterns in the WM area, and tangential to radial restrictions in the skull compartment.

4.4.2 Influence of the skull anisotropy

We used a simulated spherical head model with a modified skull compartment to analyze a single layer anisotropic skull against a 3−layer isotropic compartment following our previous work [Cuartas et al., 2014b].

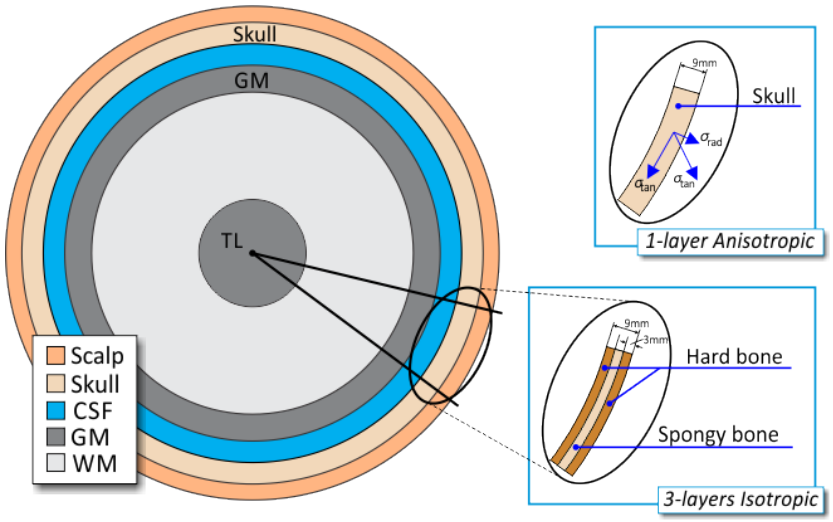

Figure 4.9: Spherical 3−layer skull model.

Figure 4.9 shows the spherical head model (defined in section 3.2.1, Figure 3.6) with a modification of the skull dividing the tissue compartment into three different isotropic layers. We performed a parametric inverse comparison taking the anisotropic 1−layer

model as the reference model, and the isotropic 3−layer as the test model, for a $10-20$ electrode distribution with 30 sensors.

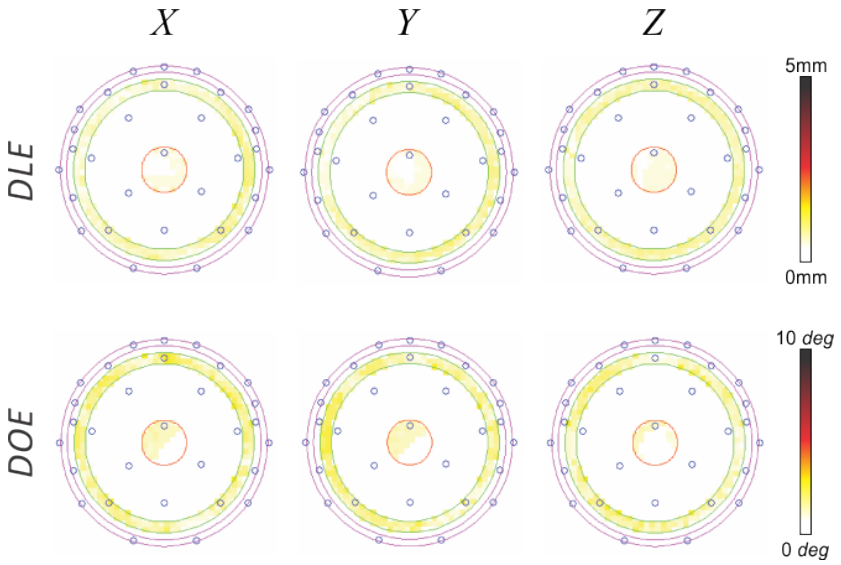

Figure 4.10: Parametric inverse comparison for the 3−layer isotropic skull and the 1−layer anisotropic skull.

We show the *DLE* (top) and *DOE* (button) for the parametric inverse comparison in the Figure 4.10. The results show low dispersion in the *DLE*, with differences of 0.88 ± 0.70, indicating a high correspondence between the models. Moreover, the *DOE* illustrates a similar result with 1.45 ± 0.68 error. The results are consistent with the reported in the literature, showing equivalence between the isotropic 3−layer and the anisotropic 1−layer skull models [Montes et al., 2013, Dannhauer et al., 2011].

Finally, we perform a parametric inverse comparison using the RHM data set. We calculate reciprocity solutions using the GFDARM algorithm for a 128 electrode setup. First, we estimate a reference anisotropic skull model following the setup presented in section 4.2.1, and later we calculate a full isotropic model used as the test model.

Figure 4.11 shows the *DLE* due to neglect the skull anisotropy in RHM. The results show a significant impact in the source localization where *DLE's* can be larger than $20mm$, especially in zones of the brain near to the skull (grey matter outer cortex). Following this results, one can expect an important influence in the distributed source localization algorithms in ESI solutions due to neglect the skull anisotropy. Similarly, the *DOE*'s can be larger than 115 degrees, and this must be considered because the

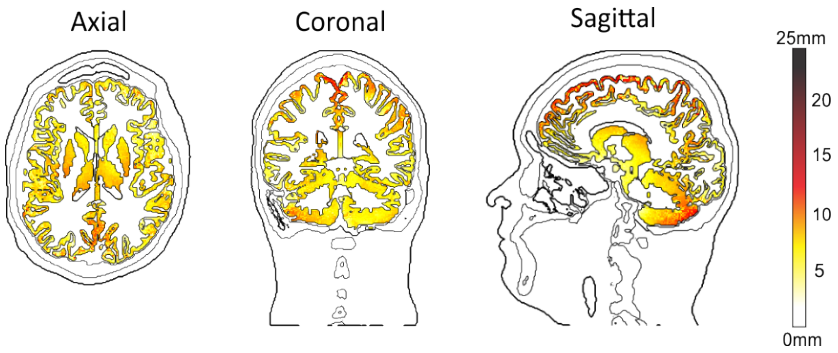

Figure 4.11: *DLE* due to neglect the skull anisotropy.

dipole orientation directly influences the estimation of the source spatial direction (normal to the GM tissue) in ESI solutions.

4.4.3 Influence of the WM anisotropy

Following our previous work [Cuartas et al., 2014a], we analyze the dipole estimation errors in a parametric inverse solution setup for three different anisotropic eigenvalues estimations for the WM compartment. The anisotropic models were set as reference models and compared against a full isotropic head model. We used Structural MRI and DWI data from IDA-LONI database publicly available (`https://ida.loni.usc.edu/login.jsp`). The MRI was a $T1$ sequence of a healthy 24-years male subject. The data were acquired on a SIEMENS Trio Tim $3T$ MRI Scanner with a $1mm^3$ resolution. A DWI sequence with 72 slices was acquired with an echo spin sequence having the following parameters: 64 directions, repetition time was 890.0 ms, echo time was 88.0 ms, thickness of 2.0 mm, and voxel size - $1.98 \times 1.98 \times 1.98\, mm$. To correct subject orientation and geometrical distortions, the $T1$ and DWI data were aligned with a voxel similarity-based affine registration procedure. The registered DWI data were re-sampled to $1mm^3$ and transformed into DTI using the FSL toolbox [Jenkinson et al., 2012]. Head model was segmented with the LBF method [Cardenas et al., 2013], setting a Gaussian kernel with scale σ=3 considering five different tissues, namely skin, skull, CSF, WM and GM. We used the GFDARM algorithm to perform forward calculations taking the isotropic conductivities from Table 4.1. Further, we used the registered DTI data to approximate the anisotropic conductivity tensors D in the white matter, considering four head models, particularly, a simple full isotropic model that we used a test model, and three different anisotropic ratio modeling with the following eigenvalues

Model	$DLE[mm]$	$DOE[deg]$
A	$2.33 \pm 1.32 \uparrow 8.400$	$11.06 \pm 7.48 \uparrow 45.74$
B	$2.64 \pm 1.53 \uparrow 12.23$	$12.73 \pm 9.47 \uparrow 63.44$
C	$2.58 \pm 1.48 \uparrow 11.47$	$11.92 \pm 7.98 \uparrow 59.44$

Table 4.2: Dipole estimation error due to neglect the anisotropic WM.

estimation for the anisotropic WM:

Model A We set the anisotropic white matter conductivity using a constant $1 : 0.11$ (radial:tangential) ratio with a volume constrain as assumed in [Wolters et al., 2006].

Model B We set the anisotropic white matter conductivity eigenvalues using the fractional anisotropy (FA) local measure as a variable ratio considering a spherical volume constrain, following [Gullmar et al., 2010]:

$$FA = \sqrt{\frac{1}{2}\left(3 - \frac{1}{tr(R^2)}\right)} \tag{4.5}$$

Where $R = D/tr(D)$ is the normalized diffusion tensor D, and $tr(\cdot)$ stands for the trace operator.

Model C We used of the anisotropy ratio (AR) measure given in [Hallez et al., 2008] and formulated as:

$$AR = \frac{\lambda_{max}}{0.5(\lambda_a + \lambda_b)} \tag{4.6}$$

Where $\lambda_{max} = max(\lambda_i)$ is the major eigenvalue, and λ_a, λ_b are the secondary eigenvalues in the diffusion tensor D.

Figure 4.12 shows the dipole estimation errors using the isotropic model as test model, and the three anisotropic WM models A, B and C as reference models. We show Axial, Coronal and Sagittal views of the DLE for the three anisotropic WM considered models. In case of the model A, the results measure the errors when neglecting the anisotropic nature of WM, while in the simulations B and C results reflect the source localization performance when neglecting the variable ratio of the anisotropic WM.

Table 4.2 shows the dipole estimation errors due to neglect the anisotropic WM. We illustrate the DLE and DOE *mean*, standard deviation (std) and maximum (max)

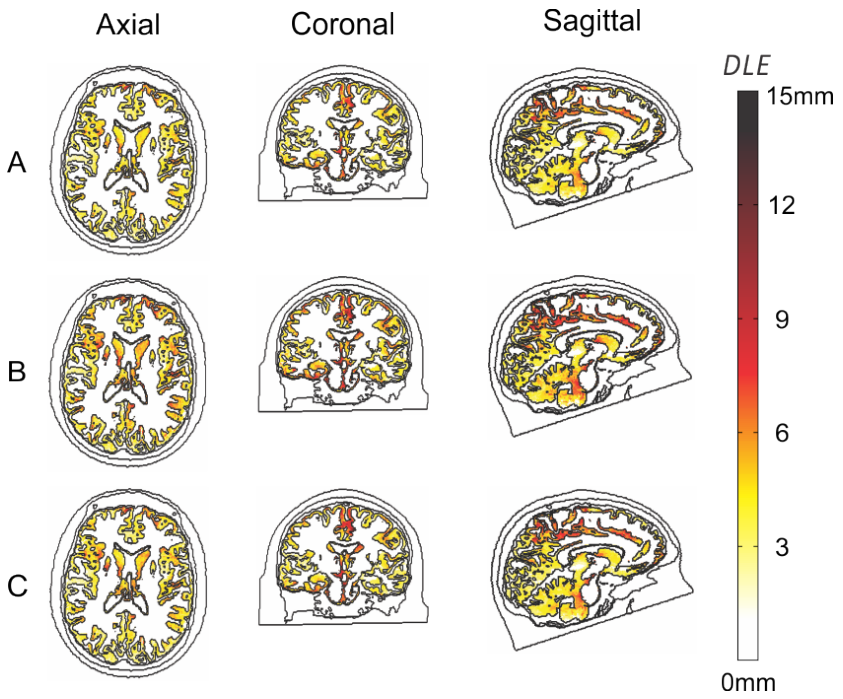

Figure 4.12: Dipole estimation errors due to different anisotropic WM modeling

values ($mean \pm std \uparrow max$) for the three considered anisotropic WM models. Results show the lowest values of *DLE* and *DOE* for the model *A*.This can be explained since the model considers only constant anisotropy ratio and does not assume highly anisotropic areas of the WM. In turn, simulation *B* provides larger *DLE* and *DOE* values due to the inclusion of information varialbe eigenvalues extracted from the DTI data, emphasising the highly anisotropic areas in the white matter. Finally, the simulation *C* performs a bit lower error values since the used variable anisotropic ratio (that is, *AR* Eq 4.5) is smoother than the *FA* measure.

Achieved *DLE* and *DOE* values are highly correlated in all three simulations. Nonetheless, the maximun *DLE* values slightly differ between model *A* and models *B* and *C*. The same situation remains for the *DOE* but in a lower rate. The significant separation between the estimated mean and maximum values is due to the presence of white matter areas having very dissimilar anisotropic values, especially in the deeper areas of the brain with strong anisotropic behaviour as the corpus callosum. Obtained results show significant influence of the anisotropic variable ratios of deep brain sources reaching values of $12\,mm$ and $60\,deg$ for *DLE* and *DOE*, respectively.

Finally, we perform a parametric inverse comparison using the RHM data set.

We calculate reciprocity solutions using the GFDARM algorithm and a 128 BioSemi electrode array, estimating a reference anisotropic WM model following the setup presented in section 4.2.2, and comparing against full isotropic test model.

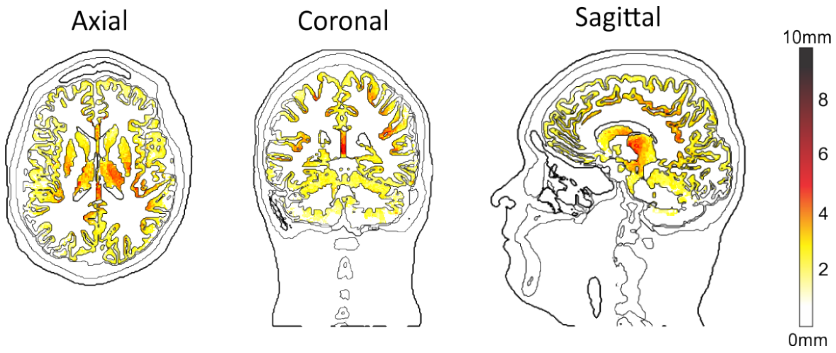

Figure 4.13: *DLE* due to neglect the WM anisotropy.

Figure 4.13 shows the *DLE* due to not include anisotropy in the WM tissue, exposing a significant impact in the source localization, where the *DLE* errors can be larger than $8mm$, especially in deep brain areas. Similarly, the *DOE* can be larger than 48 degrees, also in deep brain areas. Furthermore, the results are consistent with other works reported in the literature [Vorwerk et al., 2014, Wolters et al., 2006, Hallez et al., 2007a, Bashar et al., 2008c].

4.4.4 Multiple tissues influence in the forward modeling

As a final test, we analyze the dipole estimation errors due to not include multiple tissue compartments with varying conductivities in the realistic forward modeling. Further, we calculate forward reciprocity models using GFDARM with isotropic conductivities taken from Table REF. We employed the 9-layer RHM segmentation (Figure 4.2) as the reference model, including the additional tissues representing eyes, fat, muscle and blood vessels. Additionally, we used the 5-tissues segmentation for the RHM model as the test model in a parametric inverse setup following [Cuartas et al., 2017b].

Figure 4.14 shows Axial, Coronal and Sagittal planes for the *DLE* comparing the 9-layer reference model against the simplistic 5-layer test model using the RHM data. Results show *DLE* larger than $20\,mm$ in the deep brain and inter-cortical GM areas. This result is also consistent with the literature, where the complexity of the realistic head model often increase the accuracy of ESI techniques [Vorwerk et al., 2014, Strobbe et al., 2014a, Irimia et al., 2013, Irimia et al., 2011].

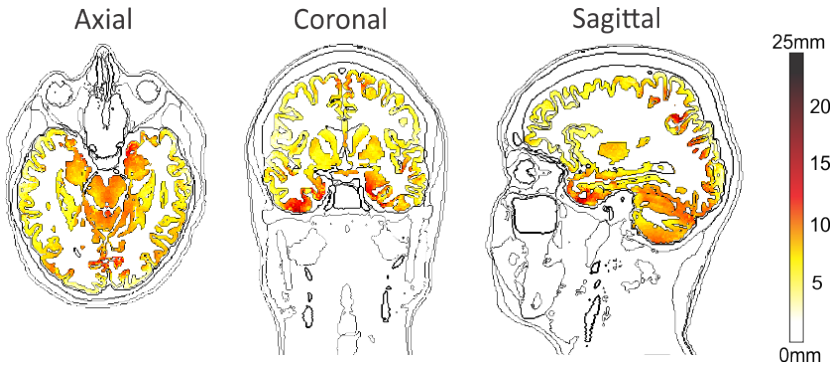

Figure 4.14: Dipole localization errors for a 9-tissues segmentation against a simplify 5-tissues head model.

We also analyze the influence of anisotropic blood vessels modeling, based on our previous work [Cuartas et al., 2017b], considering the analysis of low-frequency anisotropic behaviour of blood vessels in the human body [Wtorek et al., 2005]. To perform the arteries segmentation, we apply a mask that is extracted from a T2-angiogram and enables estimation of the blood flow direction for the RHM data set. Then, a kernel with six directions is convolved with the mask to produce a normalized vector map that describes the eigenvectors inside the segmented arteries. Further, we model the anisotropic blood vessel setting local eigenvectors $\boldsymbol{R}$ that points towards the local eigenvector of the blood vessels gradient. The anisotropic blood vessels conductivity eigenvalues at the maximum movement are defined as λ=diag$(\sigma_b, \sigma_a, \sigma_b)$, where a σ_a=0.21S/m, and σ_b=0.49S/m, following [Wtorek et al., 2005].

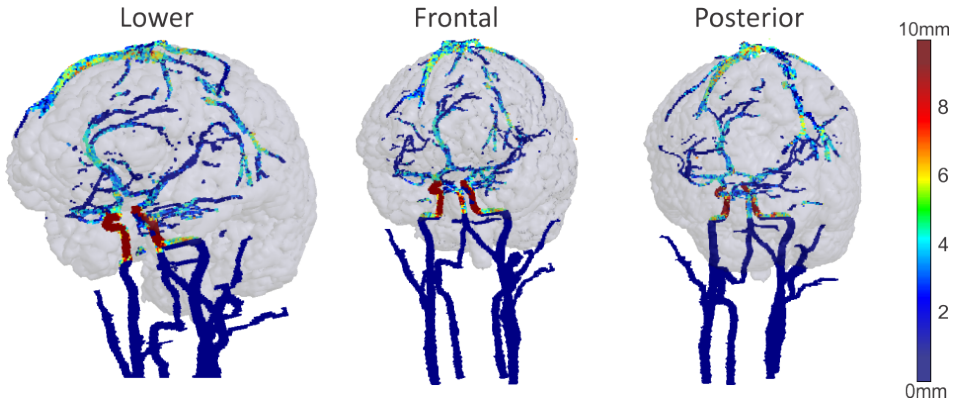

Figure 4.15: Dipole localization errors due to neglecting the anisotropic blood vessels.

We set a 9-layer anisotropic blood vessel reference model and compared against an 8-layer test model without blood vessels segmentation compartments. Remaining tissues where considered isotropic with conductivity values taken from Table 4.1. Figure 4.15 shows three different views (frontal, posterior and bottom), for a *DLE* 3D map, revealing that neglecting the anisotropic blood vessels induce *DLE* larger than $10\,mm$ in zones near to the Willis polygon (deep brain areas). Moreover, mean *DLE* was $4\,mm$ for the GM area, and potentials propagation differences can be larger than $30\mu V$ in zones near the corpus callosum. Few works reported in the literature analyze the impact of blood vessels in forward modeling [Fiederer et al., 2016], and to our knowledge, only this work analyzes the influence of an anisotropic blood vessels in forward modeling.

4.5 Discussion

We present a flexible framework to calculate patient-specific forward models using the GFDARM algorithm. The framework can include anisotropic tensor information in a voxel-wise setup (section 4.2.4, Figure 4.6). Moreover, we introduce methodologies to compute local eigenvectors and eigenvalues in the skull (section 4.2.1, Figure 4.4) and white matter (section 4.2.2, Figure 4.5) tissue compartments. Additionally, we present a novel anisotropic blood vessel modelling (section 4.4.4) for a 9-layer MRI based head data (section 4.1.2). Further, our results show notable attenuation of the magnitude and also a significant deviation of the equipotential lines over the scalp surface as a direct effect of anisotropic modelling using the proposed GFDARM solution. This result is similar to other works [Lanfer et al., 2012, Montes et al., 2013]. Also, we estimate parametric inverse solutions to analyze the dipole estimation errors due to neglect the skull anisotropy (Figure 4.11), registering *DLE* bigger than $20mm$. Moreover, analyzing WM anisotropy neglecting (Figure 4.13), we found *DLE* errors larger than $8mm$, especially in deep brain areas. This result was also similar to the reported in [Wolters et al., 2006, Hallez et al., 2008, Haueisen, 2007, Vorwerk et al., 2014].

4.5.1 Influence of the anisotropic forward modeling

The anisotropic behaviour of skull and white matter significantly affects the potentials propagation in realistic head models. Anisotropic modeling induces determinant potential scalp attenuations, inducing also notable deviations of the equipotential lines as resported in section 4.4.1. Our results also show 50 to 70 percent electrode scalp

potential attenuation (Figure 4.7). Moreover, equipotential lines tend to align with local dominant eigenvectors of skull and white matter displacing the equipotential lines (Figure 4.8) and producing deviated potential patterns in the WM, and tangential to radial restrictions in the skull compartment (Figure 4.8). Results show that anisotropic head modeling directly influences the potentials propagation in the human head, and based on the results, we suggest using anisotropic estimation in forward modeling.

4.5.2 Influence of skull anisotropy modeling

We develop a skull anisotropic framework for patient-specific data adapted to the GFDARM algorithm. Accordingly, we estimate a smooth skull mesh from the RHM dataset segmentation (section 4.1.2). Skull mesh is aligned with the MRI segmented data, and the mesh normals are used to determine local eigenvectors for the volumetric skull compartment applying an iterative propagation methodology (see section 4.2.1). Furthermore, to analyze the skull modeling, we defined a spherical 3−layer isotropic skull model (Figure 4.9) finding a high correspondence with the single layer anisotropic model (Figure 4.10) [Cuartas et al., 2014b]. This result is consistent with similar studies reported in the literature [Montes et al., 2016]. Furthermore, we used the RHM data to analyze the influence of neglecting the anisotropic skull in an inverse parametric solution, finding DLE's larger than $20mm$ in cortical GM areas (Figure 4.11), and DOE up to $115deg$. Our results show that neglecting the anisotropic skull induces significant errors in the dipole estimations being similar to the reported in the literature [Vorwerk et al., 2014, Dannhauer et al., 2011, Marin et al., 1998, Pohlmeier et al., 1997]. Thus, one can select a 3−layers isotropic skull compartment, but the segmentation of spongy bone from MRI is often a difficult task, and some authors use probabilistic atlas segmentation based on the energy invasive CT data [Torrado et al., 2016, Montes et al., 2016, Lanfer et al., 2012]. Due to this, and based in our results, we strongly suggest modeling the skull as a single anisotropic layer if the segmentation does not include hard and spongy bone tissue compartments.

4.5.3 Influence of white matter anisotropy modeling

Anisotropy in he white matter can be modeled using DWI data and DTI estimation. We develop a WM anisotropic framework for the GFDARM algorithm using DTI data and a tensor scaling transformation, using volume constraint to obtain anisotropy conductivity WM maps following [Vorwerk et al., 2014]. Moreover, early

anisotropic forward modeling consider constant radial to tangential eigenvalues [Wolters et al., 2006, Basser et al., 1994, Hallez et al., 2008]. However, the anisotropic distribution in the WM is not regular, and there are zones with highly anisotropic behaviour as the corpus callosum, in contrast, there are other areas with near isotropic behaviours, like the regions surrounding cortical brain areas [Basser et al., 1994]. On the other hand, latter works also use the eigenvalue information from the DTI [Vorwerk et al., 2014, Tuch et al., 2001]. We analyze three different WM anisotropy models, namely, a constant radial to tangential eigenvalue ratio, and two variable eigenvalue estimations based on the DTI data [Cuartas et al., 2014a]. Obtained results show significant influence of the anisotropic variable ratios of deep brain sources reaching values of 12 mm and 60 deg for DLE and DOE, respectively (Figure 4.12). Finally, we test the WM anisotropy modeling for the RHM data with eigenvalues obtained from the scaled DTI (Figure 4.5, Eq 4.1). Our results show that the anisotropic modeling of the WM is especially important in deep brain areas, where we obtained DLE larger than $8mm$, and DOE larger than $48deg$ (Figure 4.13). Accordingly, our suggestion based on the results is that the WM anisotropy eigenvalues must be obtained/adapted from DTI data and not fixed with a constant radial to tangential ratio.

4.5.4 Influence of multiple tissues in the forward modeling

Finally, we analyze the influence of multiple tissues definition for the 9−layer and the commonly used 5−layer head data. Our parametric inverse solution results show DLE larger than 20 mm in deep brain and inter-cortical GM areas. This result is also consistent with the literature, where the complexity of the realistic head model often increases the accuracy of ESI techniques [Vorwerk et al., 2014, Strobbe et al., 2014a, Irimia et al., 2013]. Moreover, we introduce an anisotropic blood vessel modeling based on gradients from the T2 angiomap of the RHM data. Our results show mean DLE of $4mm$, with a big impact in zones near to the Willis polygon (deep brain areas) resulting in DLE larger than $10mm$. To our knowledge, this is the first analysis for the anisotropic blood vessel in forwarding modeling, and other works analyze isotropic blood vessels influence [Fiederer et al., 2016]. Our suggestion is to use more detailed head models for ESI solutions, including several tissues segmentation with proper conductivity definitions. This suggestion is similar to the affirmed by [Irimia et al., 2013, Irimia et al., 2011].

Chapter 5

Forward model influence in the ESI task

The synergetic effects connecting spatial and functional techniques allows reduction of the weakness for single method analysis [Grech et al., 2008]. Specifically, EEG Source Imaging (ESI) relating structural head models and distributed source localization techniques improves the time and spatial resolution of single MRI or EEG analysis [Michel et al., 2004]. ESI information is used for diagnosis and preoperative stages of brain surgery being, in most cases, the only suitable analysis tools because of the high risk of surgical interventions [Martinez et al., 2017, Voges et al., 2011, Titto et al., 2004, Waberski et al., 2000].

ESI techniques allow the estimation of neuronal activity from electrical potentials measured over the scalp (EEG). In particular, ESI solution needs real EEG signals, a method for mapping of the measured activity from electrodes to the sources (EEG inverse problem solution), and a correct modeling of the potentials conduction and morphology of the head, meaning, a forward solution. In this regard, the accuracy of ESI solutions directly depends on the capabilities of the forward model to adequately describe the information from sources to sensors [Grech et al., 2008, Strobbe et al., 2014a, Vorwerk et al., 2014]. We use the GFDARM technique to calculate patient-specific head models, analyzing model complexity (number of tissue compartments) and anisotropic modeling in a Bayesian model selection framework following [Rigoux et al., 2014].

5.1 EEG source imaging (ESI)

Dipole current sources from large clusters of pyramidal cells are the precursors of the EEG (see section 2.1.1). Current dipoles representing synchronous activation in the brain cortex generate electric fields that propagates through the head volume, reaching the scalp. A single current dipole can reach several electrodes over the scalp surface (as shown in Figure 2.4(a)). Moreover, typical EEG protocols like the $10-20$ system contain 20 to 35 electrodes, regularly distributed over the scalp surface. Further, recent hdEEG arrays contain up to 256 sensors [Liu et al., 2018]. By contrast, distributed source localization techniques consider several thousands dipole sources in the GM. Thus, dipole source estimation or EEG inverse problem becomes an ill-posed problem, because the unknown information (sources) is larger than the available information (sensors) [Grech et al., 2008]. Due to this, EEG inverse solutions must rely on prior knowledge of the propagated sources, in addition to the observed EEG measurements. Therefore, Bayesian approaches establish the ESI as a linear problem formulated on a distributed source modeling, allowing the inclusion of source priors information to solve the EEG inverse problem. We use a Bayesian framework where a generalized verisimilitude cost function known as *free energy* is optimized to find a unique solution using Restricted Maximum Likelihood (ReML) methods [Martinez et al., 2017].

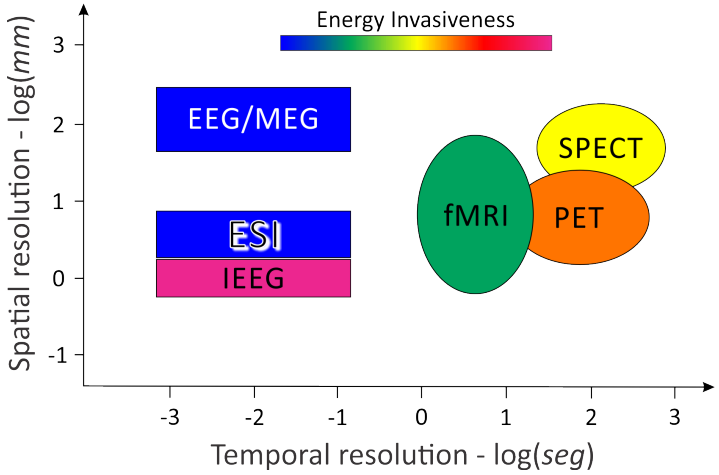

Figure 5.1: Brain imaging technologies.

Figure 5.1 show the spatial ($log(mm)$) and temporal ($log(seg)$) resolutions for the most comonly used brain imaging technologies, including an energy invasiveness color bar. Figure illustrates the positron emission tomography (PET), single photon

emission computed tomography (SPECT), functional magnetic resonance (fMRI), magneto-encephalography (MEG), invasive or intracranial EEG (IEEG), and EEG source imaging (ESI). The Figure 5.1 points that ESI is the technique with more desired properties including minimum invasiveness, high temporal resolution ($100ms$), and good spatial resolution (reaching $2mm$ for hdEEG). Thus, ESI solutions transform the EEG information into sources activations, allowing brain functional analysis with higher spatial resolution compared with the simple EEG registers while preserving the high temporal resolution. Moreover, Bayesian distributed solutions allow Bayesian model selection (BMS) analysis [Stephan et al., 2009] and random effect analysis [Rigoux et al., 2014] that we use to find the head models (forward solutions) that best represents the EEG considered signals [Strobbe et al., 2014a].

5.1.1 Event related potentials

Particular EEG responses associated with specific sensory, cognitive or motor events are known as Event-Related Potentials (ERPs). Further, the EEG contains several simultaneously brain processes, consequently, the brain response to an event of interest is usually unperceptible in a single EEG recording [Britton et al., 2000, Lange et al., 1997]. Thus, to obtain recognizable brain response due to a specific event is necessary to record various EEG trials for a specific stimulus, and then, making a time average to emphasise the repetitive event response eliminating the background noise [Castaño et al., 2015, Wakeman et al., 2015]. Ensemble averaging (EA) method has been widely used to extract the ERPs from a noisy background. The method makes two critical assumptions: i) Assumes that the on-going background EEG activity is a statistically random process, and will, therefore, be canceled out by averaging over a large number of trials, leaving the non-random ERPs signals. ii) Assumes that ERP's signals are similar for each trial included in the average [Jaskowski et al., 1999].

Figure 5.2 shows the ERP's signals (Figure 5.2(a)), scalp potentials map (Figure 5.2(b)), and ESI maps using MSP algorithm (Figure 5.2(c)) for a visual stimulus event. ERPs Figure 5.2(a) show variational dynamics across stimulus trials for a single experiment. Such variations may be associated with fluctuating attention levels, adaption to stimuli, fatigue, or other unknown factors [Haufe et al., 2016]. Thus EA methods may fail to track trial-to-trial variations both in latency and amplitude. For this reason, different models to extract the relevant information had been employed during past years, including Wiener filter, Adaptive filter, Maximum-Likelihood Method

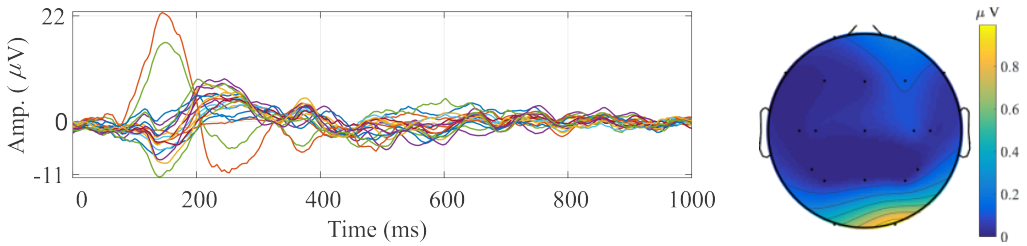

(a) ERP's (b) Scalp map

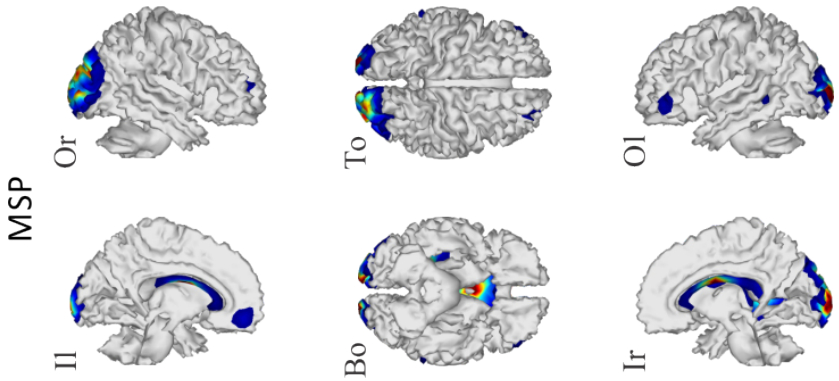

(c) EEG source imaging (ESI)

Figure 5.2: ESI solutions for a visual ERP stimulus.

and Autoregressive Process among others [Kilic et al., 2003].

5.2 The *lead-field* matrix

5.2.1 The source space

Forward modeling solution provides the potential for the whole conductivity volume concerning a single dipole source placed in the GM compartment. However, ESI solutions requires only the electrode potentials induced by a set of dipole sources, this is known as a *lead-field* matrix $L \in \mathbb{R}^{N_E \times \mathbb{N}_D}$ relating N_E electrodes (sensors) due to N_D dipole sources placed in the brain (as explained in section 3.1.6). Furthermore, distribute ESI solutions requires not only discrete source spaces for the GM, but also source prior information about the relation of the sources with other neighbouring dipoles. To fulfill this task, most ESI solutions nowadays use single bidimensional

meshes as source spaces, providing not only a directly renderable GM shaped surface but holding also connections between neighbour sources (source priors) and normal dipole orientations respect to the GM surface (dipole moments). However, the human head is volumetric, and GM is a volumetric compartment and not a single mesh interface surface. Nonetheless, most volumetric techniques use surface meshes as source space, losing volumetric interpretation about the head model.

5.2.2 Volumetric priors

We assumed a distributed volumetric source space for the GM compartment, taking a regular spacing δ_E in the three orthogonal directions for dipole positioning (we use $\delta_E = 3mm$ in this work). Furthermore, for every single dipole, we estimate a 3D influence area δ_γ with a specified distance from the dipole position, this area grants estimation of the neighbouring information that we use to calculate the Green's function adjacent matrix as source priors for distributed solutions following [Strobbe et al., 2014b] (we use $\delta_\gamma = 5{\times}5{\times}5mm$ in this work). Moreover, we estimate the dipole moments (orientations) using mesh surfaces from the GM and WM boundaries and propagating the mesh normals to estimate the dipole moments having normal directions respect to the GM cortex (as done in section 4.2.1, Figure 4.4). Finally we calculate *lead-field* matrices $\boldsymbol{L}_m{\in}\mathbb{R}^{N_C \times N_D}$ in a reciprocity approach using GFDARM for a given electrode disposition with N_C channels, and source space with N_D sources (dipoles).

The figure 5.3 show a volumetric neighbor influence area of $\delta_\gamma = 5mm^3$ where the analyzed dipole (green arrow) have 5 dipole neighbors (red arrows), for a $\delta_E = 3mm$ regular source spacing. In the figure we can also appreciate the normal estimation from both, WM, GM, and the directions of the estimated GM normals after the propagation process (yellow arrows).

5.3 Distributed inverse solutions

For a EEG dataset $\boldsymbol{Y}{\in}\mathbb{R}^{N_C \times T}$ of N_C sensors, T time samples, and a given *lead-field* matrix $\boldsymbol{L}_m \in \mathbb{R}^{N_C \times N_D}$, the magnitude of the neural activity $\boldsymbol{J}{\in}\mathbb{R}^{N_D \times T}$ for N_D current dipoles distributed in the GM, is generally represented by the general linear model [Dale et al., 1993]:

$$\boldsymbol{Y} = \boldsymbol{L}_m \boldsymbol{J} + \boldsymbol{\Xi} \tag{5.1}$$

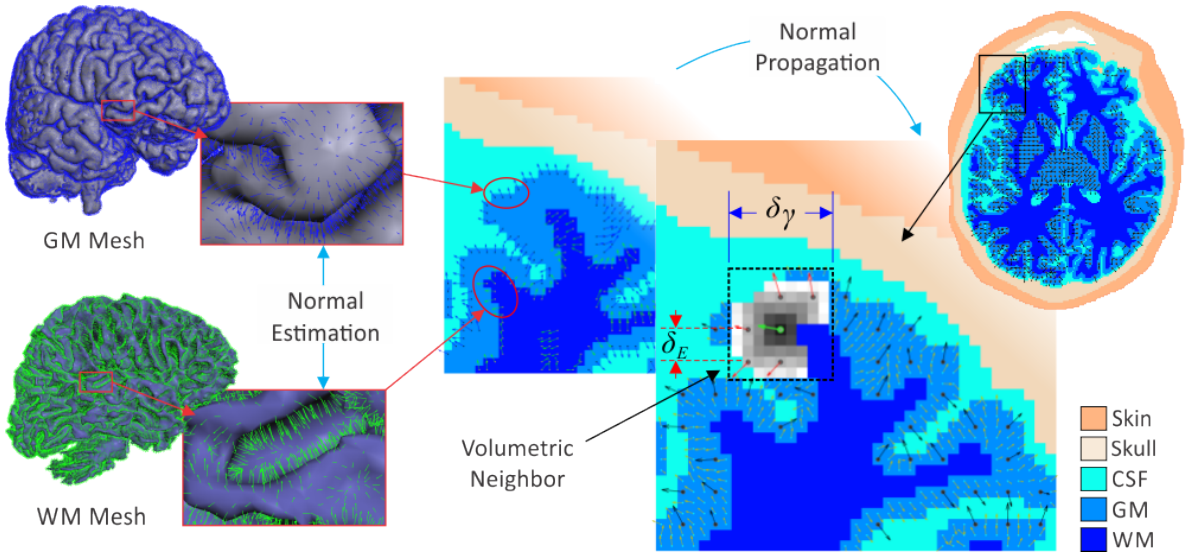

Figure 5.3: Volumetric priors estimation. Showing from left to right the GM and WM meshes used to estimate the cortex normal directions in the GM with an iterative normal propagation. The figure also illustrates a planar view of the Green's gaussian volumetric neighbour around a single dipole.

Where $\boldsymbol{\Xi} \in \mathbb{R}^{N_C \times T}$, is an additive white noise matrix with covariance $\text{cov}(\boldsymbol{\Xi}) = \exp(\lambda_0)\boldsymbol{I}_C$, where $\boldsymbol{I}_{N_C} \in \mathbb{R}^{N_C \times N_C}$ is an identity matrix, and $\lambda_0 \in \mathbb{R}^+$ an hyperparameter modulating the sensor noise variance. Under the previous premise, source estimation can be expressed by the expected value of the posterior source activity distribution, which can be computed from the input data using the Baye's theorem, as follows:

$$P(\boldsymbol{J}|\boldsymbol{Y}) = \frac{P(\boldsymbol{Y}|\boldsymbol{J})P(\boldsymbol{J})}{P(\boldsymbol{Y})} \tag{5.2}$$

We can solve Eq 5.2 assuming that $\boldsymbol{J}$ is a zero mean Gaussian process with prior covariance $\text{cov}(\boldsymbol{J}) = \boldsymbol{Q} \in \mathbb{R}^{N_D \times N_D}$. Consequently, brain activity estimation is carried out by solving the maximum-a-posteriori problem in the form:

$$\tilde{\boldsymbol{J}} = \underset{\boldsymbol{J}}{\text{argmax}} \{P(\boldsymbol{J}|\boldsymbol{Y})\} \approx \underset{\boldsymbol{J}}{\text{argmax}} \{P(\boldsymbol{Y}|\boldsymbol{J})P(\boldsymbol{J})\} \tag{5.3}$$

The optimization problem from Eq 5.3 yields the estimation of the following form:

$$\tilde{\boldsymbol{J}} = \boldsymbol{Q}\boldsymbol{L}_m^\top (\boldsymbol{Q}_\Xi + \boldsymbol{L}_m \boldsymbol{Q} \boldsymbol{L}_m^\top)^{-1} \boldsymbol{Y} \tag{5.4}$$

Requiring prior information about the source covariance matrix $\boldsymbol{Q}$. Further, we consider three different source prior covariance matrices, namelly Loreta-like (LOR) priors [Harrison et al., 2007], Empirical Bayesian Beamformer (EBB) priors [Belardinelli et al., 2012], and Multiple Sparse Priors (MSP) [Friston et al., 2008].

5.3.1 Loreta-like (LOR) priors

This formulation considers that sources vary smoothly over space. A smoothing function with the desirable behavior is proposed in [Harrison et al., 2007], using a Green's function $\boldsymbol{Q}_G = \exp(\sigma \boldsymbol{G}_M)$, with $\boldsymbol{Q}_G \in \mathbb{R}^{N_D \times N_D}$, where $\boldsymbol{G}_M \in \mathbb{R}^{N_D \times N_D}$ is a graph Laplacian that comprises inter-dipole connectivity information about all neighboring dipoles, and $\sigma \in \mathbb{R}^+$ rules the spatial expansion of the activated areas. Consequently, the source prior is computed as:

$$\boldsymbol{Q} = \exp(\lambda_1)\boldsymbol{Q}_G \tag{5.5}$$

with $\lambda_1 \in \mathbb{R}^+$ and hyperparameter to be estimated.

5.3.2 Empirical Bayesian Beamformer (EBB) priors

EBB assumes one global prior for the source covariance main diagonal, where the off-diagonal elements are zeros, i.e., no correlations assumed . Thus, the $d-$th position of the source covariance matrix main diagonal is calculated as [Belardinelli et al., 2012]:

$$\boldsymbol{Q} = diag\left(\exp(\lambda_1)(\boldsymbol{l}_{md}^{\top}\boldsymbol{C}_Y^{-1}\boldsymbol{l}_{md})\right) \tag{5.6}$$

where $\boldsymbol{l}_{md} \in \mathbb{R}^{N_D \times 1}$ is the d-th column of the lead field matrix, and $\boldsymbol{C}_Y \in \mathbb{R}^{N_C \times N_C}$ is the EEG data covariance matrix.

5.3.3 Multiple Sparse Priors (MSP)

MSP source covariance matrix is constructed as a sum of a set of P patches $\{\boldsymbol{Q}_p, p{=}1, \ldots, P\}$ each one reflecting one potentially activated region of cortex, weighted by the respective hyperparameter λ_p, as follows [Friston et al., 2008]:

$$\boldsymbol{Q}{=}\sum_{p=1}^{P} \exp(\lambda_p)\boldsymbol{Q}_p, \tag{5.7}$$

5.3.4 Free Energy as cost function

To estimate the hyperparameter set $\{\lambda_{\boldsymbol{\Xi}}, \lambda_{\boldsymbol{P}}\}$, we use the verisimilitude function known as *free-energy* [Wipf et al., 2010]. In this regard, for a given EEG recording and a certain forward model m, the free energy can be expressed as [Martínez Vargas et al., 2016]:

$$F(m)=-\frac{N_t}{2}Tr(\boldsymbol{\Delta}^{-1}\boldsymbol{C})-\frac{N_t}{2}ln\,|\boldsymbol{\Delta}|-\frac{N_cN_t}{2}ln2\pi-\frac{1}{2}(\boldsymbol{\mu}-\boldsymbol{\eta})^T\boldsymbol{\Omega}^{-1}(\boldsymbol{\mu}-\boldsymbol{\eta})+\frac{1}{2}ln\,|\boldsymbol{\Upsilon}\boldsymbol{\Omega}^{-1}| \quad (5.8)$$

where $\boldsymbol{\Delta} \in \mathbb{R}^{N_C\times N_C}$ is the estimated model covariance, computed as $\boldsymbol{\Delta}=\boldsymbol{LQL}^{\top}+\boldsymbol{Q}_{\Xi}$; $\boldsymbol{C} \in \mathbb{R}^{N_C\times N_C}$ is the measured data covariance, $\boldsymbol{\mu}, \boldsymbol{\eta} \in \Re^{N_D\times 1}$ are the prior and posteriors means of the hyperparameters $\{\lambda_{\Xi}, \lambda_p\}$. Likewise, $\boldsymbol{\Upsilon}, \boldsymbol{\Omega} \in \mathbb{R}^{N_D\times N_D}$ are the posterior and prior hyperparameter covariances. $|\cdot|$ represent the matrix determinant operator.

Therefore, maximizing the *free-energy* cost function Eq 5.8 can be considered as a trade-off between the accuracy and the complexity of the solution. The accuracy penalizes the difference in variance between the measured EEG data $\boldsymbol{Y}$ and the estimated solution $\widehat{\boldsymbol{Y}}=\boldsymbol{LJ}$. The complexity provides a measure of the difficulty level to optimize the hyperparameters for a given prior. Hence, the *free-energy* Eq (5.8) can be divided as follows:

$$F(m)=accuracy(\lambda)-complexity(\lambda), \quad (5.9)$$

Free Energy can be maximized using standard variational schemes [Wipf et al., 2010]. To perform this optimization scheme, we use a greedy search (GS) algorithm. Further, the set of GS hyperparameters were tuned through the Restricted Maximum Likelihood (ReML) algorithm, following [Belardinelli et al., 2012, Friston et al., 2008].

5.3.5 Bayesian model selection (BMS)

To compare different forward models using the Bayesian Framework, define the dependency on a certain forward model m, Eq 5.2 as:

$$p(\boldsymbol{J}_m|\boldsymbol{Y},m)=\frac{p(\boldsymbol{Y}|\boldsymbol{J}_m,m)p(\boldsymbol{J}_m)}{p(\boldsymbol{Y}|m)}, \quad (5.10)$$

where $p(\boldsymbol{J}_m)$ represents the prior assumptions about the source activity and $p(\boldsymbol{Y}|m)$ the model evidence [López et al., 2012]. Furthermore, the log evidence $\log p(Y, \hat{\lambda})$, of the *free-energy* computed with the optimal set of estimated hyperparameters, provides an approximation to the log model evidence $\log p(\boldsymbol{Y}|m)$ [López et al., 2012, López et al., 2014]. In consequence, the *free-energy* can be used for Bayesian model selection. Hence, some metrics based on the free energy values are defined to test the likelihood of obtaining a model in favor of another model, given the EEG data as follows

$$\log(\psi_{(m_1,m_2)}) = \frac{p(\boldsymbol{Y}|m_1)}{p(\boldsymbol{Y}|m_2)} = F(m_1) - F(m_2) \tag{5.11}$$

where $F(m_1)$ and $F(m_2)$ are the free energy corresponding with a model 1 and a model 2, respectively. The log group Bayes factor (Ψ) is defined as the sum of the individual log Bayes factors over N subjects as follows:

$$\log(\Psi) = \sum_{n=1}^{N} \log(\psi^n_{(m_i,m_j)}) \tag{5.12}$$

where, the subscripts i, j refer to the models being compared, and N is the number of subjects. According to [Penny et al., 2004], a model can be chosen in favor of another when there is a difference larger than three units for the Eq 5.12. This criteria apply for both the log ψ and the log Ψ at group level. It is worth to note that Ψ is a simple index for direct model comparison and it does not account for group heterogeneity or outliers. Furthermore, we performed a random-effects analysis to estimate the expected posterior model frequency that expresses the belief that a model has the highest posterior probability, relative to the other models following [Rigoux et al., 2014, Stephan et al., 2009]. Additionally, we calculate the Bayesian omnibus risk (BOR) that quantifies the probability that the expected posterior model frequencies are all equal to each other. Thus, if the BOR is smaller than 0.25, then we can be confident in the model selection based on the exceedance probability results [Strobbe et al., 2014a].

5.4 Experiments and results

5.4.1 New York head model (NYM)

We selected an additional head model template to compared against the RHM (see section 4.1.2). To this end, we use the New York segmentation template that combines the ICBM152 v2009b data ($0.5\,mm^3$ resolution) with the ICBM152 v6 image template of the non-brain area, having $1\,mm^3$ resolution [Huang et al., 2016] including the extended neck that uses an average of 26 subjects heads. The extended model is segmented with a $0.5\,mm^3$ resolution, admitting five tissues (scalp, skull, CSF, GM, and WM). Additionally, we perform a downsampling process to a $1\,mm^3$ resolution space, taking into account a minimum thickness of two voxels to ensure that the scalp tissue surrounds the electrode positions in the lead fields as suggested in [Hallez et al., 2009]. Likewise, we fix to one voxel the minimum thickness for CSF to make sure that the GM tissue is fully contained in the CSF and do not have connected voxels to the skull as suggested by [Ramon et al., 2006, Wolters et al., 2006].

5.4.2 EEG Data set

We use the multi-subject, multi-modal human neuroimaging dataset including fMRI and EEG (among other neuroimaging data) [Wakeman et al., 2015]. We selected 15 patients, 8 males, and 7 females, with an age range $23-37$ years, all Caucasian with European origins. An evoked potential visual experiment is carried out using face images stimuli including two sets of 300 greyscale photographs, half from famous people and the other half from nonfamous people (unknown to participants). In the data set, half of the faces were male, half female, leaving 3 trial-types (conditions): Familiar Faces (Famous), Unfamiliar Faces (Nonfamous) and Scrambled Faces. Stimuli were projected onto a screen approximately $1.3mts$ in front of the participant, and visual markers were projected to synchronize the stimuli apparition. A 70 channel Easycap EEG cap was used to record the EEG data simultaneously, with electrode layout conforming to the extended $10-10$ system. EEG data were acquired at an 1100 Hz sampling rate with a lowpass filter at 350 Hz and no highpass filter, including processing stages for automatic detection of bad channels throughout the run, notch-filtering of the 50 Hz line-noise and its harmonics and a trial rejecting stage. Finally, an averaging the remaining trials for each of the three conditions was made to calculate ERP's for $1s$ time windows. For more details about EEG data set see [Wakeman et al., 2015].

Furthermore, we used the 3D electrode positions included in the database to coregister the sensor positions to the head volumes (RHM and NYM) space using a fiducial-based similarity transformation. Additionally, the electrode locations are projected again towards the center direction of the head volume in order to find electrode voxel positions not surrounded by air as suggested in [Hallez et al., 2009].

5.4.3 Complexity considerations for the Head Models

We define six different forward model setups increasing the complexity (number of tissues and anisotropy) of the models. First, we build three isotropic models, beginning with the simplest model M1 including only three tissues, namely skin, skull, and brain, then, for the model M2, we add the CSF, and for the model M3, we divide the brain area into GM and WM. Further, form the 5 tissues model M3, we include skull anisotropy for model M4, WM anisotropy for model M5, and both, skull and WM anisotropy for the most complex M6 model. Finally, we calculate 10 different head models using the AFDRM algorithm for the 70 electrodes of the EEG database using M1 to M6 for RHM and M1 to M4 for NYM structural MRI data, as shown in Table 5.1.

Isotropic	*Anisotropic (M3)*
M1: skin, skull, brain	*M4*: skull anisotropy
M2:*M1* + CSF	*M5*: WM anisotropy
M3: *M3* + brain → GM,WM	*M6*: skull & WM anisotropy

Table 5.1: Proposed head models

5.4.4 Bayesian model selection for group studies

We used Bayesian model selection based on*free-energy* in order to study the head model influence in the studied group [Rigoux et al., 2014, Stephan et al., 2009] (see section 5.3.5). To this end, we calculate *free-energy* factors to the full ERP's time window ($1s$) using the LOR and EBB techniques for the 15 considered patients, the three different visual stimuli and the 10 proposed head models for a total of 900 test. Then we group the *free-energy* of the reconstructions over stimulus conditions for each ESI technique to apply a random effects analysis at the group level, where the log group Bayes factor can be obtained summing over the 15 subjects [Stephan et al., 2009].

5.4.5 Model comparison based on free energy

The Figure 5.4 show the expected posterior model frequency for both ESI considered techniques, EBB (right) and LOR (left) and the 10 considered head models. Both charts include a vertical dashed line separating the RHM and the NYM structural head data. Moreover, the Figure REF includes separate results for the different visual stimulus, Famous (blue), Unfamiliar (green), and Scrambled (red), showing the BOR values in the button part of the charts.

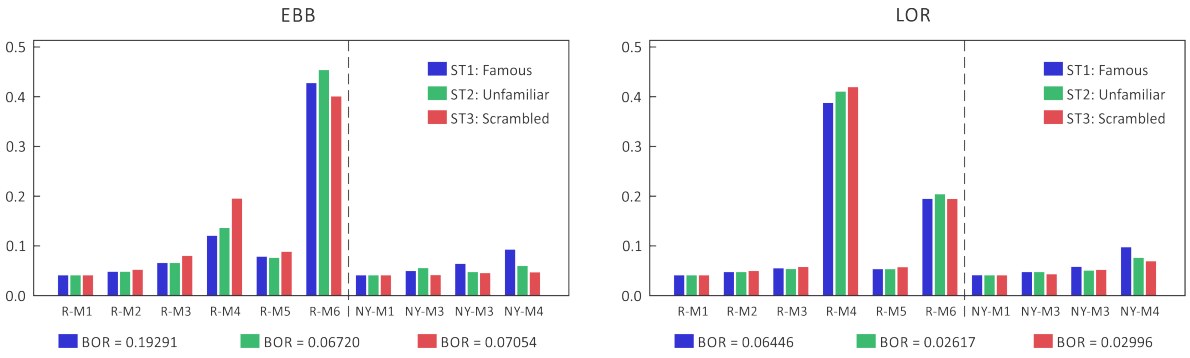

Figure 5.4: Random fixed analysis showing expected posterior model frequency, for EBB and LOR inverse solution techniques.

The EBB results show strong evidence in favor of the most complex model M6, with an appreciable increment of the exceedance probability between the simplest model M1 and the models M2 and M3. Moreover, models M4 and M6 including skull anisotropy show the highest probability evidence for the three different experiments, indicating that the skull modeling is a decisive factor in the ESI applications. Furthermore, the M5 model including WM anisotropy has the best performance compared against the isotropic models (M1, M2, and M3). NYM show the same behavior of RHM models, but with lower probability differences. Similarly, the LOR results show an increasing exceedance probability for the most complex models, but the best performance is for the model M4 including only skull anisotropy. All test have low BOR values indicating strong evidence in favor of the obtained results.

5.4.6 ESI visual stimulus results

We analyzed the stimulus-response for the most complex model M6 using EBB and LOR source estimations a single subject.

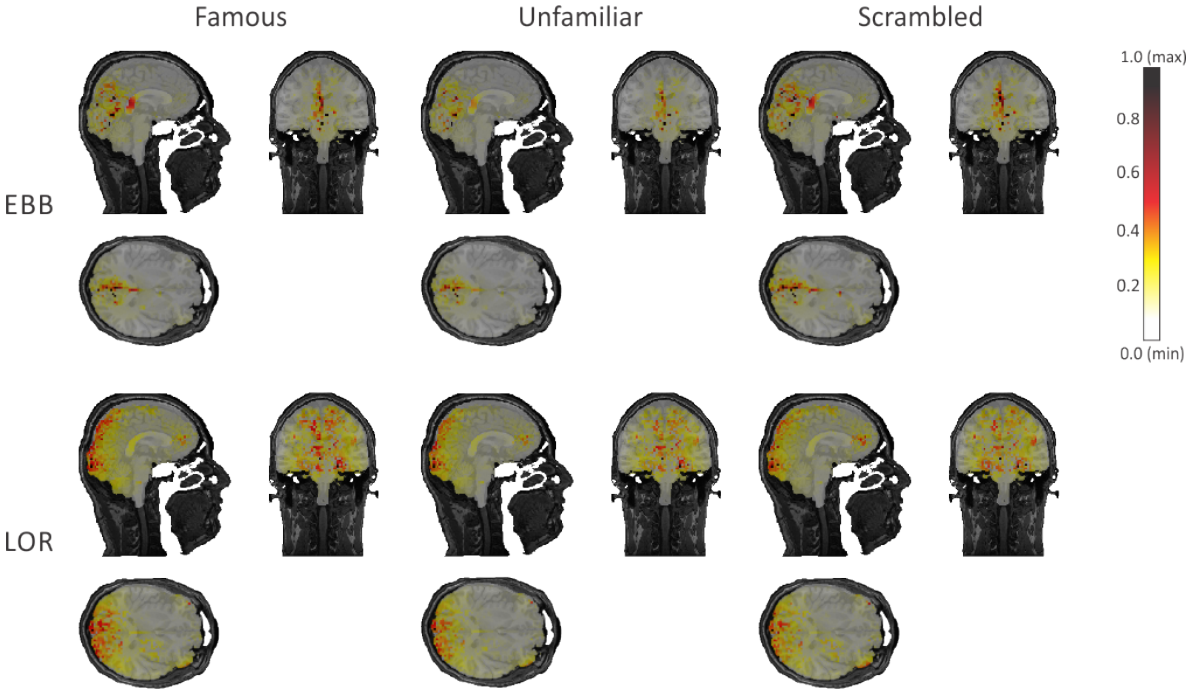

Figure 5.5: Stimulus response.

The figure 5.5 shows the maximum intensity projection maps for the three considered stimuli namely, Famous, Unfamiliar and Scrambled. Concerned to the ESI techniques, EBB shows a better energy distribution with more concentrated areas in the visual cortex areas, in comparison, LOR shows a spread energy distribution making more difficult the analysis of specific activation zones. Moreover, the figure shows appreciable differences in the energy distribution for the different considered stimulus, with less intensity in the Thalamus area for the Unfamiliar stimulus compared to the Famous stimulus for the EBB technique that cannot be appreciated with LOR.

5.4.7 Anisotropic modeling influence in the ESI task

We analyze the model complexity influence in the source localization using the EBB technique for three models namely, M1, M3 and M6, considering two different subjects, S8(top) and S9 (button) from the database. This test shows the effect of increasing the number of tissues (M1 to M3) and also the effect of include anisotropy in both, WM and skull areas (M3 to M6).

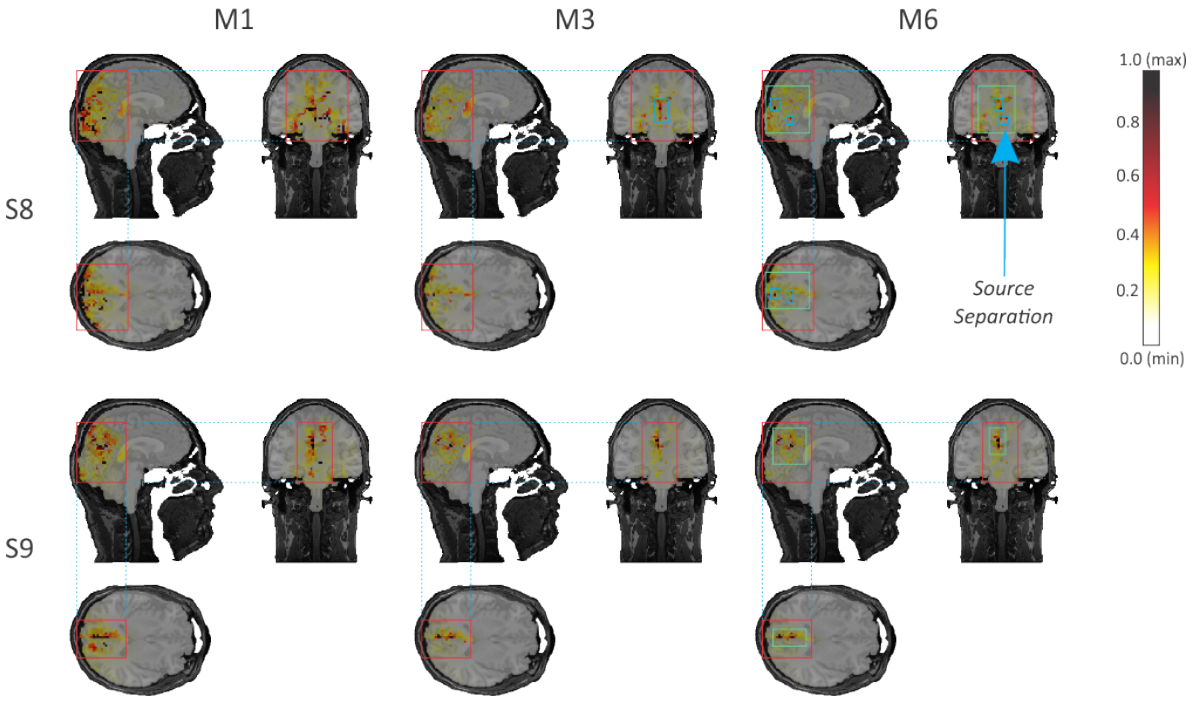

Figure 5.6: Model complexity.

Figure 5.6 shows a normalized maximum intensity projection for the considered models, where it can be appreciated that the energy is more spread in model M1 compared to model M3. Moreover, the inclusion of anisotropic skull and WM for the model M6 show not only a concentrated activation area but also possible spatial separation for individual activations in the visual cortex that appears as a mixed and single activation in the models M1 and M3. We used red squares to show the source activation zone for the model M1, and green squares for the concentrated area of activation in the model M6, additionally, we used blue squares to show the source energy separation between two different sources that are very near one to each other.

Moreover, the energy separation for more complex head models is consistent with similar analysis results [Liu et al., 2018].

Neglecting Skull anisotropy

We analyzed the considered ESI techniques for a single subject and the Unfamiliar stimulus ERP, taking into account the model M3 (5 isotropic layers) and M4 (5 layers anisotropic skull) for the RHM structural MRI dataset.

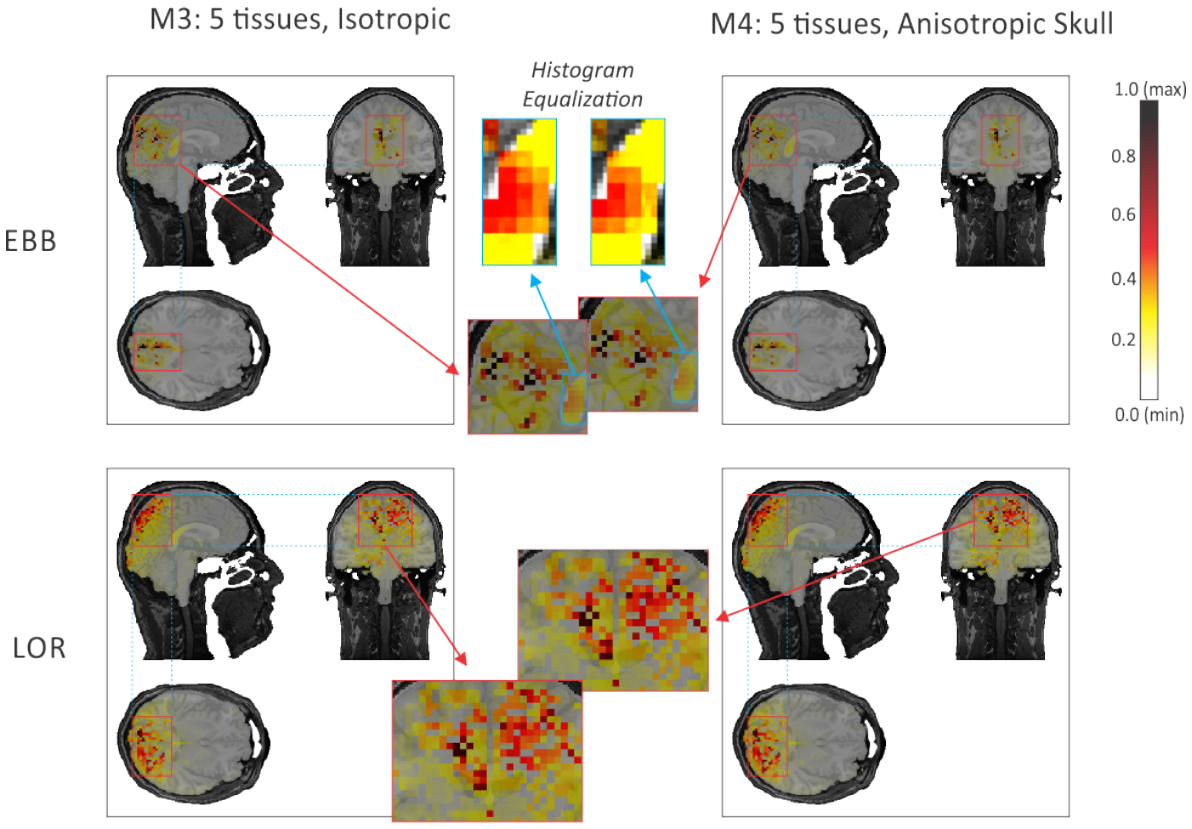

Figure 5.7: Influence of anisotropic skull in the EBB and LOR ESI techniques.

Fig 5.7 shows the maximal intensity projection for EBB (top) and LOR (button). We can appreciate a generalized energy reduction in the maximal intensity projection maps for the anisotropic skull model M4 compared against the isotropic model M3 using the EBB ESI technique. Furthermore, we calculate a histogram equalization to emphasize the contrast in the energy reduction effect for the specific zone indicated in

the middle of the figure. The same effect can be appreciated in the button part of the figure for the LOR technique. For both techniques, we select the area with larger brain activity. This effect can be appreciated in every subject under consideration, showing an average 15.06% reduction of the dipole magnitudes for EBB and 18.23% for the LOR technique in presence of skull anisotropic skull. Additionally, as expected, the results show a better energy distribution with concentrated activity using the EBB estimation.

5.4.8 Comparing with fMRI data

Finally, we compared the ESI results with fMRI registers for BOLD responses in a single subject.

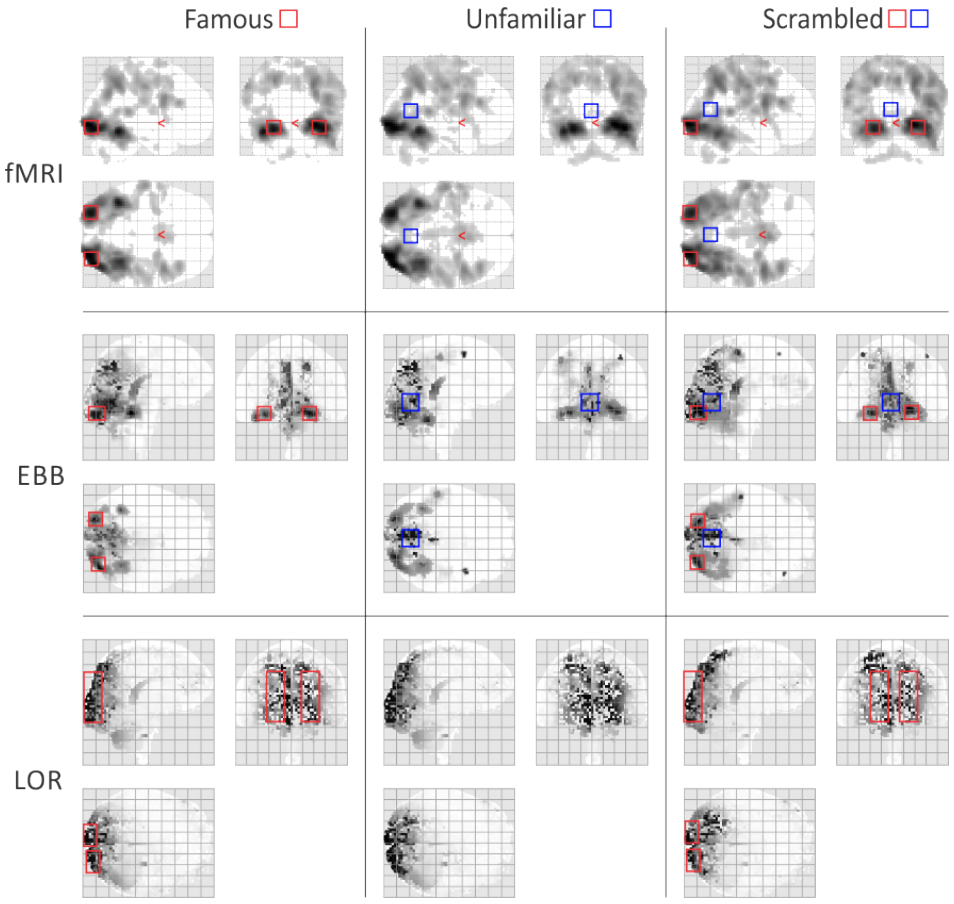

Figure 5.8: fMRI comparison.

We calculate maximum intensity projections for the three orthogonal directions

considering the fMRI registers and the EBB and LOR ESI techniques, in a single subject, for the three considered stimuli. We highlighted the most relevant zones of activation for the fMRI face visual stimuli suggested by [Henson et al., 2003], using red squares for the Famous stimuli, and blue squares for the Unfamiliar stimuli. Moreover, we highlighted the zones with high intensity near the suggested fMRI areas for the EBB results, showing a good correspondence between the fMRI data and the obtained results. However, EBB show spread activation areas with high intensity in zones differing from the fMRI data, with a visual energy cluster near the corpus callosum and in the posterior visual cortex. Moreover, LOR results show general consistency in the activation virtual cortex zone, but loosing discriminative spatial possibilities due to the spread energy distribution.

5.4.9 Population dependent forward modeling influence in the ESI task

We evaluate the patient-dependent head model influence in the ESI task for three different structural data, namely, the standardized MRI template (NY) (see section 5.4.1), a demographic population atlas (AT), and a set of 25 patient-specific MRI scans (PD).

MRI and EEG/ERP registers were acquired from 25 children within an age range between 5 to 16 years old, having two socio-cultural levels (high–medium and low–medium). All patients were randomly selected from the preschool, elementary, and secondary courses at a few private and public schools of Manizales city. For legal purposes, the children's parents agreed to participate in the research through a written permission. According to the children's historical data, the exclusion criteria were established for mental retardation, individuals with neurological antecedents (history of head trauma, epilepsy, and related) or referring psychiatric disorders (psychiatric hospitalization history, autism, and similar).

MRI strcutural data

Patient dependent/specific head model (PD): A set of T1-MRI scans were acquired from the same 25 children under study, employing a 1.5 T General Electric OPTIMA MR 360 scanner with the following parameters: $1mm^3$ voxel size, T_R=6, T_E=1.8, T_I=450, sagittal slices of 256×256. Three scans were performed for each child

with a posterior averaged stage to improve the MRI quality, obtaining a single MRI for each patient.

Atlas head model (AT): We built an anatomical head atlas from the 25 averaged MRI scans, employing the Diffeomorphic Anatomical Registration (DARTEL) algorithm generating a population dependent template [Goto et al., 2013] using the SPM Toolbox [Karl et al., 2007].

EEG/ERP

ERP's Data were obtained following an oddball experimental paradigm for cognitive evoked potentials with rare visual stimuli, where each evoked stimulus lasted 130 ms, while the time delay between the onsets of two consecutive stimuli was 1 s. During each stimulation, the subjects had to pay attention to the rare stimulus (termed *target*) and count their occurrence, ignoring the presence of remaining stimuli (*non–targets*). The non–target stimuli were displayed on 80% of the trials, whereas the target stimuli –on 20% of remaining trials, resulting in approximately 160 non–target stimuli and 40 target stimuli. The EEG recordings were collected using 19 electrodes symmetrically placed at the standard positions of the international 10-20 system, operating a single *(Cadwell) Easy III EEG amplifier*. Data were subsampled at 250 Hz and segmented in 1-s epochs, which were averaged separately over each subject and stimulation condition. As a result, two ERPs were obtained following the different stimulus conditions for each subject, namely, visual target (V-T) and visual non-target (V-nT).

Forward modeling and priors estimation

We obtained 5-layer segmentations for the AT and PD MRI data using *FreeSurfer* (`https://surfer.nmr.mgh.harvard.edu/`), considering skin, skull, CSF, GM and WM tissue compartments. Moreover, we calculate isotropic head models using conductivity isotropic values from Table 4.1. Further, we calculate forward solutions using the GFDARM algorithm, in a reciprocity space for the 19 coregistered EEG sensors. Additionally, we calculate GM mesh surfaces as priors holding 10.000 vertex, and corresponding to dipole source positions. The mesh was obtained applying morphological operators over the volumetric segmentation to obtain source spaces fully contained in the GM tissue compartment.

Bayesian model selection for group studies

We estimate *free-energy* values of the inverse solutions over subjects, corresponding with the ERP's of each stimulation condition namely, visual target (V-T), and visual non-target (V-nT). Further, we use Bayesian model selection for group studies following [Rigoux et al., 2014, Strobbe et al., 2014a] (see section 5.3.5), defining three different model grups for the three considered MRI data, namely NY, AT, and PD . Then, the log group Bayes factor, expected posterior probability and Bayesian omnibus (BOR) are estimated.

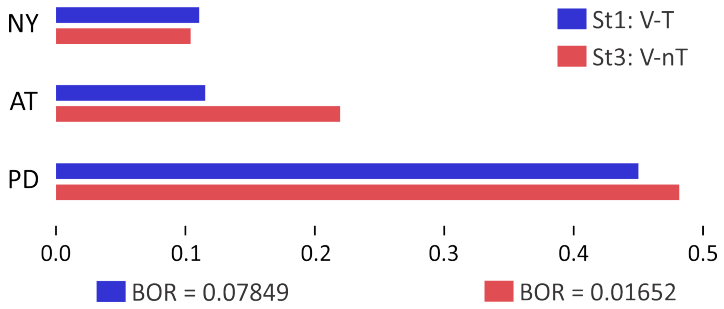

Figure 5.9: MSP results for Bayesian model selection expected posterior probability and Bayesian omnibus risk (BOR) for two different stimuli, namely visual target (V-T) and visual non-target (V-nT).

Figure 5.9 shows that the best model is the PD data achieving the highest expected posterior probability with high confidence results performing small BOR values for both tests V-T, and V-nT. Results are similar for NY and AT data considering the V-T stimulus, by contrast, AT outperforms NY data for the V-nT stimulus. Further, NY data results are very similar, with a low expected posterior probability, showing the low correlation with the considered population. Moreover, second best choice goes for the AT data set, depending on the population.

Figure 5.10 shows the ESI solution for a single patient. The ERP waveform shows a prominent temporo-occipital negative peak around 180 *ms*, which is mostly associated with visual processing. Moreover, the reconstructed activity localizes some components in the vicinity of the temporal lobe, covering the visual cortices for all the tested models. However, NY model spreads the brain activity, which makes that some activations appear in non-visual related areas. Besides, for the AT head model we can apreciate an activation of the middle temporal gyrus, associated with visual-related tasks [De Vos et al., 2012]. Additionally, for the PD head model, an activity patch

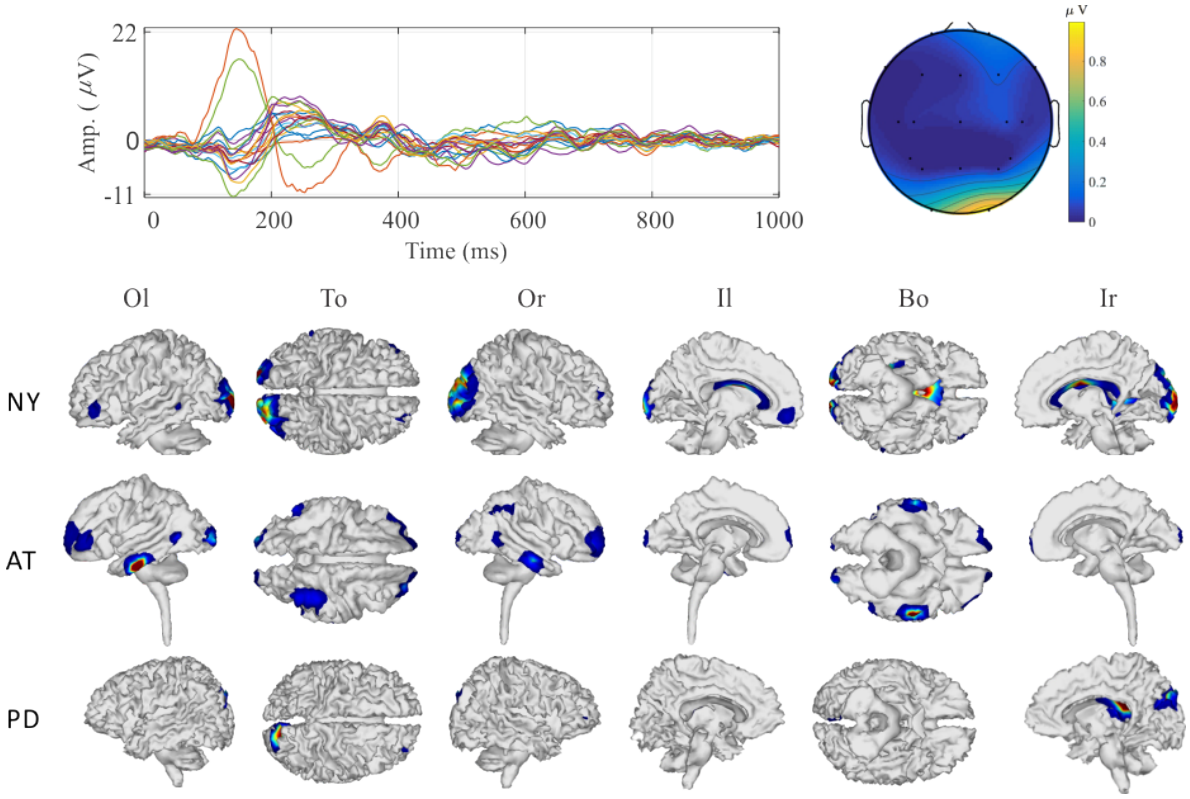

Figure 5.10: ESI solution for a representative subject. Figure shows the EEG-ERP (top-left), the scalp topographic map (top-right), and the ESI reconstructed activity. Views: Outside right (Or), Outside left (Ol), Top (To), Bottom (Bo), Inside right (Ir) and Inside left (Il).

appears over the posterior cingulate gyrus, which occurs when a high demand of visual processing/discrimination is required, suggesting that this particular head model enhances the reconstruction of neural activity.

5.5 Discussion

We present a Bayesian model selection framework, adapted to the GFDARM head modelling, which allows group studies to analyse the influence of the forward modelling in distributed ESI solutions, including anisotropy information for the skull and white matter tissue compartments. The framework is based on the log evidence for the

free-energy cost function, with an additional random effect analysis to estimate expected posterior model evidence in a group level following [Rigoux et al., 2014] (see section 5.3.5). Our solution includes volumetric priors for distributed inverse solutions (see section 5.2.2), taking advantage of the proposed GFDARM volumetric technique, and providing 3D activation maps that are comparable with functional neuroimaging techniques like fMRI. Moreover, our results show evidence in favour of more complex models including up to 5-tissue compartment, and anisotropy skull and WM information. These results are similar to the reported in [Strobbe et al., 2014a, Strobbe et al., 2014b]. To our knowledge, this is the first time that the anisotropic behaviour is analysed for a FDM based forward modelling including anisotropy, and using Bayesian model selection for group studies, or volumetric priors information. Finally, we analyse patient dependent and population dependent forward modelling in the ESI task using the BMS framework. Results show very favourable evidence for patient-specific head models, compared to population dependent atlas and generic head models.

5.5.1 Head models complexity and anisotropic modeling influence in the ESI task

We analyze the forward modeling complexity influence in the ESI task using two MRI based dataset, namely, RHM and the template NYM. We calculate GFDARM solutions in a reciprocity setup for the 70 electrodes configuration given in the multi-modal, multi-subject database [Wakeman et al., 2015]. Bayesian model selection for group studies using random effect analysis results (section 5.4.5, Figure 5.4) show concluding evidence in favor of most complex head models, showing an increasing posterior model frequency probability for the EBB inverse solution on the RHM dataset, thus, from M1 to M4 we can appreciate an ascending behaviour of the exceedance probability for the three different stimulus conditions. This behaviour is also similar for the NYH dataset, suggesting an across data tendency. Further, this behaviour remains for the LOR inverse solution technique with a lower increasing rate. Results are similar to the reported in [Strobbe et al., 2014a], where only analyze CSF inclusion for a template model without anisotropy modeling. Moreover, skull modeling seems to be determinant in the ESI solutions, as suggested also in [Montes et al., 2013, Vorwerk et al., 2014, Lanfer et al., 2012]. Based on the results, we suggest the inclusion of anisotropic skull modeling in forward calculations when using distributed ESI techniques for single layer

skull compartments. Moreover, model complexity is also an essential factor, and, based on our results, we suggest that at least 5-layer tissue compartments segmentation are needed to use head models for distributed ESI techniques, this result is similar to the suggested by [Strobbe et al., 2014a].

5.5.2 Volumetric priors in ESI solutions

Using volumetric priors information is possible to build 3D functional maps relating ESI distributed approaches. Results show in Figure 5.5, present differentiable activation patterns for the three different considered stimulus, namely, Familiar, Unfamiliar and Scrambled faces. Further, EBB show a better distribution of activation zones compared against LOR results, tending to concentrate in outer cortical zones of the brain, and also spreading the activation zones across large regions, decreasing the discrimination of specific brain areas [Harrison et al., 2007]. Furthermore, model complexity impact in the volumetric ESI maps seems to be important in the detailed analysis of particular activation zones in the brain. Initial results showing in Figure 5.6 suggest a separation between near activation zones, but further analysis is needed to conclude about this finding, despite the fact that results are similar to the reported in [Liu et al., 2018]. Additionally, we analyze the influence of neglecting the skull anisotropy in the ESI task, in specific Figure 5.7,We show relevant attenuations in the ESI energy for anisotropic skull, suggesting again that skull head modeling is crucial in the ESI task. Moreover, we obtained similar results for parametric inverse analysis (section 4.4.2, Figure 4.11), showing consistency in the results concerning the skull modeling. Finally, we compared the results with a fMRI analysis (Figure 5.8), showing good correspondence between EBB results and fMRI registers.

Based on our results, we presume that volumetric priors using more complex head models, and including anisotropy can go one step further in the ESI analysis, providing 3D spatial activations maps that can be directly compared with the existent functional neuroimaging analysis like fMRI.

5.5.3 Bayesian model selection for group studies

The Bayesian model comparison approach using free energy is a probabilistic framework based on log evidence, and we don't have direct information about how good the models are. However, the random effects analysis results showing exceedance probabilities estimates which model is more probable depending on the data. Advances

and successful results in this field supports the used technique [Rigoux et al., 2014, Penny, 2012, Stephan et al., 2009, Friston et al., 2007]. Additionally, results showing that model complexity better represents the analyzed data, and the evidence in favor of anisotropic modeling are consistent with findings in the forward modeling filed over the last three decades [Liu et al., 2018, Strobbe et al., 2014a, Montes et al., 2013, Wolters et al., 2006, Saleheen et al., 1997, De Munck, 1988]. By contrast, parametric inverse solution only analyze two forward models in the reciprocity space, and one must assume the most complex or better model. Results based on parametric inverse solution suggesting only differences between two fordward solutions and do not include specific EEG signals findings. In consequence, the Bayesian model selection for group studies presented in this work and adapted to the proposed GFDARM solution using volumetric priors is a relevant tool to analyse the influence of the structural head models with realistic functional EEG data.

5.5.4 Population dependent forward modeling

As a final test, we use BMS to analyse the dependency of the structural head modeling on the population, for a visual EEG/ERP's stimuli study. Three different structural isotropic data where analyzed, namely a generic NY (NYM), a population-dependent atlas (AT), and patient-specific head models (PD). Head modeling consider reciprocity GFDARM solutions for surface meshing priors (see section 5.4.9). Results show in Figure 5.9 exhibit relevant evidence in favor of patient-specific data for the two considered stimulus experiments. Moreover, results show that the population-dependent AT head model has better correspondence with the analyzed data compared against the generic head model NY. Moreover, Figure 5.9 illustrates good correspondence between the ERP's experiments and the activations zones. Furthermore, based in the results, we suggest using patient-specific head modeling for ESI analysis, and, as a second choice, population-dependent atlases that better represents the morphology of the analyzed subjects.

Chapter 6

Final Remarks

6.1 General Conclusions and Main Contributions

Development of a suitable EEG forward solution framework

The EEG forward solution framework presented in Chapter 3 include finite differences coefficients formulated for the conservative form of the generalized Poisson Eq 2.1, and transition layer analysis to fulfill the Newman flux and Dirichlet conditions (Eq 2.2 and Eq 2.3). Further, the proposed method include ghost-filling boundary analysis to deal with the homogeneous Newman flux boundary condition Eq 2.4, solving the forward problem only for the significant discrete potentials contained inside the irregular-boundary volume. Besides, a reciprocity space solution is introduced to solve the forward problem in the sensors domain. The presented method has anisotropic capabilities and voxelwise conductivity modeling, with direct adaptation to the available discrete neuroimage data. We refer to the proposed method as ***ghost-filling* finite difference anisotropic reciprocity method** (GFDARM). Moreover, results show high correspondence with the analytical spherical solution formulated by [De Munck et al., 1993], and improved accuracy in comparison with the state-of-the-art *Simbio* FEM solution [Vorwerk et al., 2018].

As a future work, we plan to analyze the proposed GFDARM technique against the anisotropic Simbio FEM solution.

Development of a conductivity head model framework extracted from neuroimages

We develop a forward realistic head modeling framework, using neuroimages, and including anisotropic estimation for the skull and white matter tissue compartments. In Chapter 4 we detailed the proposed methodology. Furthermore, our results show significant influence in the potential propagation from sources to sensors due to forward anisotropic modeling. Results indicate that neglecting anisotropic head information can induce considerable errors in the ESI task, where the impact of ignoring the skull anisotropy yields dipole localization errors larger than $20mm$. Similarly, we analyzed the influence of neglecting the white matter anisotropy, finding that the dipole localization errors can be larger than $8mm$, with an increasing impact in deep brain areas. Besides, we analyze the influence of multiple tissue definitions showing that ignoring other relevant tissue compartments in the head, as fat, muscle or blood vessels can induce dipole localization errors larger than $20mm$. Finally, computational performance results for Chapter 2 show considerable evidence on how the presented realistic head modeling framework using the proposed GFDARM outperforms the state-of-the-art *Simbio* FEM technique.

As a future work, we intend to analyze the influence of realistic three layer isotropic skull head modeling to compare against the 1-layer anisotropic definitions.

Development of a framework to analyze the influence of the forward modeling in the EEG source localization task

Finally, in Chapter 5 we present a framework to analyze the influence of the forward modeling in the EEG source localization task, using Bayesian model selection for group studies, and random-fixed analysis to quantify the forward model that better reproduce the available EEG registers using ERP's experiments. Our results show significant evidence in favor of more complex forward head modeling, including skull and white matter anisotropic estimations. Moreover, we analyze the influence of the forward modeling in the ESI task related to the dependency of the structural neuroimage based data to the group studied. Obtained results show evidence in favor of structural patient-specific data, and, as the second option, population dependent atlas data. As a final remark, is important to notice that we introduce a novel volumetric source priors method, allowing ESI analysis in a volumetric space solution. Results can be directly

compared against functional neuroimage based techniques like fMRI.

As a future work, we aim to study the patient-specific dependency including anisotropic modeling. Besides, we plan to analyze the volumetric priors framework with more complex ESI estimations like MSP.

6.2 Future work

Besides the method-specific analyses proposed above as future work, more general topics should also be consider:

Parallel implementation: We intend to develop a GPU based parallel implementation for the GFDARM technique to calculate lead-pairs in a single parallel assignment. We presume that this kind of deployment will allow realistic froward model calculation for hdEEG reciprocity configurations in a 10 minutes time space. However, memory allocation and computational capabilities must be deeply analyzed to fulfill the requirements of the proposed task.

Global sensitivity analyzis: We want to investigate the possibilities of a global sensitivity analysis using the GFDARM technique. However, based on the results provide by cite [Salman et al., 2013, Salman et al., 2016], a fast parallel implementation is needed to perform a significant amount of forward calculations in an affordable time window.

Patient-specific brain disorders head modeling: We also aspire to analyze the impact of realistic head modelling in specific brain diseases like epilepsy, Parkinson or brain tumors. In particular [Irimia et al., 2011] model a traumatic brain injury with more than 20 tissue conductivity considerations. Also, in [Martinez et al., 2017], the authors improve the epileptogenic zone estimation without including anisotropy. Thus, we wanted to use the GFDARM technique to improve the forward modeling, analyzing its impact in ESI estimation for general brain disorders.

6.3 Academic Discussion

Cuartas, Morales, E., Cardenas, Pena, D., Castellanos, Dominguez, G., et al. 2014. *Influence of anisotropic white matter modeling on EEG source localization.* 2014 36th Annual International Conference of the IEEE Engineering in Medicine and Biology Society, EMBC 2014, 2014:4920–4923.

Cuartas, Morales, E., Hallez, H., Vanrumste, B., Castellanos, Dominguez, G., et al. 2014. *Three-layer-isotropic skull conductivity representation in the EEG forward problem using spherical head models.* 2014 36th Annual International Conference of the IEEE Engineering in Medicine and Biology Society, EMBC 2014. 2014:4904–4907.

Cuartas, Morales, E., Martinez, Vargas, J., Cespedes, Villar, Y. C., Arteaga, Daza, L., Castellanos, Dominguez, G., et al. 2017. *Influence of population dependent forward models on distributed EEG source reconstruction.* Lecture Notes in Computer Science (including subseries Lecture Notes in Artificial Intelligence and Lecture Notes in Bioinformatics). 10337 LNCS.

Cuartas, Morales, E., Torrado, Carvajal, A., Hernandez, Tamames, J. A., Malpica, N., and Castellanos, Dominguez, G. 2017. *Influence of Anisotropic Blood Vessels Modeling on EEG Source Localization.* Lecture Notes in Computer Science (including subseries Lecture Notes in Artificial Intelligence and Lecture Notes in Bioinformatics). 10337 LNCS:384–393.

Cuartas, Moreales, E., Acosta-Medina, C., and Castellanos, Dominguez, G. 2015. *iLU Preconditioning of the Anisotropic-Finite-Difference Based Solution for the EEG Forward Problem.* Lecture Notes in Computer Science (including subseries Lecture Notes in Artificial Intelligence and Lecture Notes in Bioinformatics). pages 408–418.

Bibliography

[Akalin Acar et al., 2016] Akalin Acar, Z., Acar, C. E., and Makeig, S. (2016). Simultaneous head tissue conductivity and EEG source location estimation. *NeuroImage*, 124:168–180.

[Asenco et al., 1991] Asenco, F. J., Panizo, M., et al. (1991). Finite-Difference Inhomogeneous Operators in Anisotropic Dielectrics : General Case. *Jurnal of computational physics*, 95:387–399.

[Baillet et al., 2001] Baillet, S., Mosher, J. C., and Leahy, R. M. (2001). Sylvain Baillet, John C. Mosher, and Richard M. Leahy. *IEEE Signal Processing Magazine*, (November).

[Balafar et al., 2010] Balafar, M. A., Ramli, A. R., Saripan, M. I., Mashohor, S., et al. (2010). Review of brain MRI image segmentation methods. *Artificial Intelligence Review*, 33(3):261–274.

[Bashar et al., 2008a] Bashar, M. R., Li, Y., and Wen, P. (2008a). A Study of white matter and skull inhomogeneous anisotropic tissue conductivities on EEG forward head modeling. *2008 11th International Conference on Computer and Information Technology*, pages 7–13.

[Bashar et al., 2008b] Bashar, R., Li, Y., and Wen, P. (2008b). Effects of White Matter on EEG of Multi-layered Spherical Head Models. In *5th International Conference on Electrical and Computer Engineering*, volume 00, pages 59–64.

[Bashar et al., 2008c] Bashar, R., Li, Y., and Wen, P. (2008c). Influence of white matter inhomogeneous anisotropy on EEG forward computing. *Australasian physical & engineering sciences in medicine / supported by the Australasian College of Physical*

Scientists in Medicine and the Australasian Association of Physical Sciences in Medicine, 31(2):122–30.

[Basser et al., 1994] Basser, P. J., Mattiello, J., LeBihan, D., et al. (1994). MR diffusion tensor spectroscopy and imaging. *Biophysical Journal*, 66(1):259–267.

[Belardinelli et al., 2012] Belardinelli, P., Ortiz, E., et al. (2012). Source reconstruction accuracy of meg and eeg bayesian inversion approaches. *PloS one*, 7(12):e51985.

[Berger, 1934] Berger, H. (1934). Über das Elektrenkephalogramm des Menschen. *Deutsche Medizinische Wochenschrift*, 60(51):1947–1949.

[Bloss et al., 2016] Bloss, E. B., Cembrowski, M. S., Karsh, B., Colonell, J., Fetter, R. D., and Spruston, N. (2016). Structured Dendritic Inhibition Supports Branch-Selective Integration in CA1 Pyramidal Cells. *Neuron*, 89(5):1016–1030.

[Brain Initiative Working Group, 2014] Brain Initiative Working Group (2014). *Brain 2025: A Science Vision*.

[Britton et al., 2000] Britton, J., Jervis, B., and Grünewald, R. (2000). Extracting single trial event related potentials. *IEE Proceedings-Science, Measurement and Technology*, 147(6):382–388.

[Cardenas et al., 2013] Cardenas, Pena, D., Martinez, Vargas, J. D., Castellanos-Dominguez, G., et al. (2013). Local binary fitting energy solution by graph cuts for MRI segmentation. *Conf Proc IEEE Eng Med Biol Soc.*, 2013(2):5131–4.

[Castaño et al., 2015] Castaño, Candamil, S., Höhne, J., Martínez Vargas, J. D., An, X. W., Castellanos-Domínguez, G., Haufe, S., et al. (2015). Solving the EEG inverse problem based on space-time-frequency structured sparsity constraints. *NeuroImage*, 118:598–612.

[Clark et al., 1968] Clark, J., Plonsey, R., et al. (1968). The Extracellular Potential Field of the Single Active Nerve Fiber in a Volume Conductor. *Biophysical Journal*, 8(7):842–864.

[Cuartas et al., 2014a] Cuartas, Morales, E., Cardenas, Pena, D., Castellanos, Dominguez, G., et al. (2014a). Influence of anisotropic white matter modeling on

EEG source localization. *2014 36th Annual International Conference of the IEEE Engineering in Medicine and Biology Society, EMBC 2014*, 2014:4920–4923.

[Cuartas et al., 2014b] Cuartas, Morales, E., Hallez, H., Vanrumste, B., Castellanos, Dominguez, G., et al. (2014b). Three-layer-isotropic skull conductivity representation in the EEG forward problem using spherical head models. *2014 36th Annual International Conference of the IEEE Engineering in Medicine and Biology Society, EMBC 2014.*, 2014:4904–4907.

[Cuartas et al., 2017a] Cuartas, Morales, E., Martinez, Vargas, J., Cespedes, Villar, Y. C., Arteaga, Daza, L., Castellanos, Dominguez, G., et al. (2017a). Influence of population dependent forward models on distributed EEG source reconstruction. *Lecture Notes in Computer Science (including subseries Lecture Notes in Artificial Intelligence and Lecture Notes in Bioinformatics)*, 10337 LNCS.

[Cuartas et al., 2017b] Cuartas, Morales, E., Torrado, Carvajal, A., Hernandez, Tamames, J. A., Malpica, N., and Castellanos, Dominguez, G. (2017b). Influence of Anisotropic Blood Vessels Modeling on EEG Source Localization. *Lecture Notes in Computer Science (including subseries Lecture Notes in Artificial Intelligence and Lecture Notes in Bioinformatics)*, 10337 LNCS:384–393.

[Cuartas et al., 2015] Cuartas, M., Acosta-Medina, C., and Castellanos, Dominguez, G. (2015). iLU Preconditioning of the Anisotropic-Finite-Difference Based Solution for the EEG Forward Problem. pages 408–418.

[Dale et al., 1993] Dale, Anders, M., Sereno, Martin, I., and OTHERS (1993). Improved localizadon of cortical activity by combining eeg and meg with mri cortical surface reconstruction: a linear approach. *Journal of cognitive neuroscience*, 5(2):162–176.

[Dannhauer et al., 2011] Dannhauer, M., Lanfer, B., Wolters, C. H., and Knösche, T. R. (2011). Modeling of the human skull in EEG source analysis. *Human brain mapping*, 32(9):1383–99.

[De Munck, 1988] De Munck, J. C. (1988). The potential distribution in a layered anisotropic spheroidal volume conductor. *Journal of Applied Physics*, 64(2):464–470.

[De Munck, 1992] De Munck, J. C. (1992). A linear discretization of the volume conductor boundary integral. *IEEE Trans Biomed Eng*, 39:986–990.

[De Munck et al., 2000] De Munck, J. C., Faes, T. J., Heethaar, R. M., et al. (2000). The boundary element method in the forward and inverse problem of electrical impedance tomography. *IEEE transactions on bio-medical engineering*, 47(6):792–800.

[De Munck et al., 1993] De Munck, J. C., Peters, M. J., et al. (1993). A Fast Method to Compute the Potential in the Multisphere Model. *IEEE Transactions on Biomedical Engineering*, 40(11):1166–1174.

[De Vos et al., 2012] De Vos, M., Thorne, J. D., Yovel, G., Debener, S., et al. (2012). Let's face it, from trial to trial: Comparing procedures for N170 single-trial estimation. *NeuroImage*, 63(3):1196–1202.

[Drechsler et al., 2009] Drechsler, F., Wolters, C. H., Dierkes, T., Si, H., and Grasedyck, L. (2009). A full subtraction approach for finite element method based source analysis using constrained Delaunay tetrahedralisation. *NeuroImage*, 46(4):1055–1065.

[Duraiswami et al., 1998] Duraiswami, R., Chahine, G. L., and Sarkar, K. (1998). Efficient 2D and 3D electrical impedance tomography using dual reciprocity boundary element techniques. *Engineering Analysis with Boundary Elements*, 22(1):13–31.

[Engwer et al., 2017] Engwer, C., Vorwerk, J., Ludewig, J., and Wolters, C. H. (2017). A Discontinuous Galerkin Method to Solve the EEG Forward Problem Using the Subtraction Approach. *Siam J. Control Optim.*, 34(3):A1460–A1487.

[Ferguson et al., 1997] Ferguson, a. S., Stroink, G., et al. (1997). Factors affecting the accuracy of the boundary element method in the forward problem–I: Calculating surface potentials. *IEEE transactions on bio-medical engineering*, 44(11):1139–55.

[Fiederer et al., 2016] Fiederer, L. D. J., Vorwerk, J., Lucka, F., Dannhauer, M., Yang, S., D??mpelmann, M., Schulze-Bonhage, A., Aertsen, A., Speck, O., Wolters, C. H., and Ball, T. (2016). The role of blood vessels in high-resolution volume conductor head modeling of EEG. *NeuroImage*, 128:193–208.

[Fischl et al., 2002] Fischl, B., Salat, D. H., Busa, E., Albert, M., Dieterich, M., Haselgrove, C., Van Der Kouwe, A., Killiany, R., Kennedy, D., Klaveness, S., et al. (2002). Whole brain segmentation: automated labeling of neuroanatomical structures in the human brain. *Neuron*, 33(3):341–355.

[Friston et al., 2008] Friston, K., Harrison, L., Daunizeau, J., Kiebel, S., Phillips, C., Trujillo-Barreto, N., Henson, R., Flandin, G., and Mattout, J. (2008). Multiple sparse priors for the M/EEG inverse problem. *NeuroImage*, 39(3):1104–1120.

[Friston et al., 2007] Friston, K., Mattout, J., Trujillo-Barreto, N., Ashburner, J., and Penny, W. (2007). Variational free energy and the Laplace approximation. *NeuroImage*, 34(1):220–234.

[Fuchs et al., 2002] Fuchs, M., Kastner, J., Wagner, M., Hawes, S., and Ebersole, J. S. (2002). A standardized boundary element method volume conductor model. *Clinical Neurophysiology*, 113(5):702–712.

[Gabriel, 1993] Gabriel, C. (1993). Compilation of the Dielectric Properties of Body Tissues at RF and Microwave Frequencies. *Environmental Health*, AFOSR-TR96(June):271.

[Geddes et al., 1967] Geddes, L. A., Baker, L. E., et al. (1967). The specific resistance of biological material-A compendium of data for the biomedical engineer and physiologist. *Medical and biological engineering*, 5(3):271–293.

[Geselowitz, 1967] Geselowitz, D. B. (1967). On bioelectric potentials in an homogeneous volume conductor. *Biophysics Journal*, 7:1–11.

[Goto et al., 2013] Goto, M., Abe, O., Aoki, S., Hayashi, N., Miyati, T., Takao, H., Iwatsubo, T., Yamashita, F., Matsuda, H., Mori, H., et al. (2013). Diffeomorphic anatomical registration through exponentiated lie algebra provides reduced effect of scanner for cortex volumetry with atlas-based method in healthy subjects. *Neuroradiology*, 55(7):869–875.

[Grech et al., 2008] Grech, R., Cassar, T., Muscat, J., Camilleri, K. P., Fabri, S. G., Zervakis, M., Xanthopoulos, P., Sakkalis, V., and Vanrumste, B. (2008). Review on solving the inverse problem in EEG source analysis. *Journal of neuroengineering and rehabilitation*, 5:25.

[Gullmar et al., 2010] Gullmar, D., Haueisen, J., Reichenbach, J. R., et al. (2010). Influence of anisotropic electrical conductivity in white matter tissue on the EEG/MEG forward and inverse solution. A high-resolution whole head simulation study. *NeuroImage*, 51(1):145–163.

[Hallez, 2009] Hallez, H. (2009). *Incorporation of Anisotropic Conductivities in EEG Source Analysis*. PhD thesis.

[Hallez et al., 2009] Hallez, H., Staelens, S., and Lemahieu, I. (2009). Dipole estimation errors due to not incorporating anisotropic conductivities in realistic head models for EEG source analysis. *Physics in medicine and biology*, 54(20):6079–93.

[Hallez et al., 2007a] Hallez, H., Vanrumste, B., Delputte, S., van Hese, P., Assecondi, S., D'Asseler, Y., and Lemahieu, I. (2007a). Dipole estimation errors in EEG source localization due to not incorporating anisotropic conductivities of white matter in realistic head models.

[Hallez et al., 2007b] Hallez, H., Vanrumste, B., Grech, R., Muscat, J., De, W., Vergult, A., Asseler, Y. D., Camilleri, K. P., Fabri, S. G., Huffel, S. V., and Lemahieu, I. (2007b). Review on solving the forward problem in EEG source analysis. *Journal of NeuroEngineering and Rehabilitation*, 4.

[Hallez et al., 2005] Hallez, H., Vanrumste, B., Van Hese, P., D'Asseler, Y., Lemahieu, I., and Van de Walle, R. (2005). A finite difference method with reciprocity used to incorporate anisotropy in electroencephalogram dipole source localization. *Physics in medicine and biology*, 50(16):3787–806.

[Hallez et al., 2008] Hallez, H., Vanrumste, B., Van Hese, P., Delputte, S., and Lemahieu, I. (2008). Dipole estimation errors due to differences in modeling anisotropic conductivities in realistic head models for EEG source analysis. *Physics in medicine and biology*, 53(7):1877–94.

[Harrison et al., 2007] Harrison, L. M., Penny, W., Ashburner, J., Trujillo-Barreto, N., and Friston, K. (2007). Diffusion-based spatial priors for imaging. *NeuroImage*, 38(4):677–695.

[Haueisen, 2007] Haueisen, J. (2007). The influence of forward model conductivities on EEG/MEG source reconstruction. In *2007 Joint Meeting of the 6th International Symposium on Noninvasive Functional Source Imaging of the Brain and Heart and the International Conference on Functional Biomedical Imaging*, volume c, pages 18–19. Ieee.

[Haueisen et al., 1997] Haueisen, J., Ramon, C., Eiselt, M., Brauer, H., and Nowak, H. (1997). Influence of tissue resistivities on neuromagnetic fields and electric potentials

studied with a finite element model of the head. *IEEE transactions on bio-medical engineering*, 44(8):727–35.

[Haufe et al., 2016] Haufe, S., Ewald, A., et al. (2016). A Simulation Framework for Benchmarking EEG-Based Brain Connectivity Estimation Methodologies. *Brain Topography*.

[Haufe et al., 2015] Haufe, S., Huang, Y., and Parra, L. C. (2015). A highly detailed FEM volume conductor model based on the ICBM152 average head template for EEG source imaging and TCS targeting. *Conference proceedings : ... Annual International Conference of the IEEE Engineering in Medicine and Biology Society. IEEE Engineering in Medicine and Biology Society. Annual Conference*, 2015:5744–5747.

[Henry et al., 1918] Henry, G., Henry, Vandyke, C., et al. (1918). *Anatomy of the Human Body*. Lea and Febiger.

[Henson et al., 2003] Henson, R. N., Goshen-Gottstein, Y., Ganel, T., Otten, L. J., Quayle, A., Rugg, M. D., et al. (2003). Electrophysiological and haemodynamic correlates of face perception, recognition and priming. *Cerebral Cortex*, 13(7):793–805.

[Henson et al., 2009] Henson, R. N., Mattout, J., Phillips, C., and Friston, K. J. (2009). Selecting forward models for MEG source-reconstruction using model-evidence. *NeuroImage*, 46(1):168–76.

[Herculano, 2009] Herculano, Houzel, S. (2009). The human brain in numbers: a linearly scaled-up primate brain. *Frontiers in Human Neuroscience*, 3(November):1–11.

[Huang et al., 2016] Huang, Y., Parra, L. C., and Haufe, S. (2016). The New York Head - A precise standardized volume conductor model for EEG source localization and tES targeting. *NeuroImage*, 140:150–162.

[Irimia et al., 2011] Irimia, A., Chambers, M. C., Alger, J. R., Filippou, M., Prastawa, M. W., Wang, B., Hovda, D. A., Gerig, G., Toga, A. W., Kikinis, R., Vespa, P. M., and Van Horn, J. D. (2011). Comparison of Acute and Chronic Traumatic Brain Injury Using Semi-Automatic Multimodal Segmentation of MR Volumes. *Journal of Neurotrauma*, 28(11):2287–2306.

[Irimia et al., 2013] Irimia, A., Goh, S.-Y. M., Torgerson, C. M., Stein, N. R., Chambers, M. C., Vespa, P. M., and Van Horn, J. D. (2013). Electroencephalographic inverse localization of brain activity in acute traumatic brain injury as a guide to surgery, monitoring and treatment. *Clinical neurology and neurosurgery*, 115(10):2159–65.

[Irimia et al., 2012] Irimia, A., Van Horn, J. D., and Halgren, E. (2012). Source cancellation profiles of electroencephalography and magnetoencephalography. *NeuroImage*, 59(3):2464–74.

[IT'IS Foundation, 2016] IT'IS Foundation (2016). Tissue properties database v3.1. data retrieved from the Foundation for Research on Information Technologies in Society, https://www.itis.ethz.ch/virtual-population/tissue-properties/downloads/database-v3-1/.

[Janaszewski et al., 2010] Janaszewski, M., Couprie, M., and Babout, L. (2010). Hole filling in 3D volumetric objects. *Pattern Recognition*, 43(10):3548–3559.

[Jaskowski et al., 1999] Jaskowski, P., Verleger, R., et al. (1999). Amplitudes and latencies of single-trial erp's estimated by a maximum-likelihood method. *IEEE Transactions on biomedical engineering*, 46(8):987–993.

[Jenkinson et al., 2012] Jenkinson, M., Beckmann, C. F., Behrens, T. E., Woolrich, M. W., and Smith, S. M. (2012). FSL. *NeuroImage*, 62(2):782–790.

[Juan et al., 2015] Juan, José, V., Kinahan, P., et al. (2015). Positron Emission Tomography: Current Challenges and Opportunities for Technological Advances in Clinical and Preclinical Imaging Systems. *Annu Rev Biomed Eng*, 12(2):130–140.

[Karl et al., 2007] Karl, F., Ashburner., J., Kiebel., S., Nichols., T., Penny., W., et al. (2007). *Statistical Parametric Mapping: The Analysis of Functional Brain Images*. Elsevier.

[Kikinis et al., 2014] Kikinis, R., Pieper, S., Vosburgh, K., et al. (2014). 3d slicer: A platform for subject-specific image analysis, visualization, and clinical support. 3:277–289.

[Kilic et al., 2003] Kilic, S., Gencer, N., and Baykal, B. (2003). Comparison of methods for extracting of evoked potentials. In *Engineering in Medicine and Biology Society,*

2003. Proceedings of the 25th Annual International Conference of the IEEE, volume 3, pages 2495–2498. IEEE.

[Laboratory for Computational Neuroimaging and technology, 2013] Laboratory for Computational Neuroimaging, H.-M. h. s. and technology (2013). Freesurfer.

[Lagarias et al., 1998] Lagarias, J. C., Reeds, J. A., Wright, M. H., and Wright, P. E. (1998). Convergence Properties of the Nelder–Mead Simplex Method in Low Dimensions. *SIAM Journal on Optimization*, 9(1):112–147.

[Lanfer et al., 2012] Lanfer, B., Scherg, M., Dannhauer, M., Knösche, T. R., Burger, M., and Wolters, C. H. (2012). Influences of skull segmentation inaccuracies on EEG source analysis. *NeuroImage*, 62(1):418–31.

[Lange et al., 1997] Lange, D. H., Pratt, H., and Inbar, G. F. (1997). Modeling and estimation of single evoked brain potential components. *IEEE transactions on BioMedical Engineering*, 44(9):791–799.

[Lantz et al., 2011] Lantz, G., Grouiller, F., and Spinelli, L. (2011). Localisation of Focal Epileptic Activity in Children Using High Density EEG Source Imaging. *Epileptologie 2011*, 28:84–90.

[Le Bihan et al., 2012] Le Bihan, D., Johansen, Berg, H., et al. (2012). Diffusion MRI at 25: Exploring brain tissue structure and function. *NeuroImage*, 61(2):324–341.

[Le Bihan et al., 2001] Le Bihan, D., Mangin, J.-F., Poupon, C., Clark, C. A., Pappata, S., Molko, N., and Chabriat, H. (2001). Diffusion tensor imaging: Concepts and applications. *Journal of Magnetic Resonance Imaging*, 13(4):534–546.

[Lee et al., 2007] Lee, W. H., Kim, T.-S., Kim, Y. H., and Lee, S. Y. (2007). Mesh Quality Analysis of MRI Content-adaptive FE Head Models for Neuro-Electromagnetic Imaging. In *Proceedings of the 3rd International IEEE EMBS Conference on Neural Engineering*, pages 248–251.

[Li and Yan, 2009] Li, J. and Yan, D. (2009). Solving the EEG Forward Problem by FDM and FEM. *2009 2nd International Conference on Biomedical Engineering and Informatics*, 0(3):1–4.

[Li et al., 2018] Li, Z., Qiao, Z., Tang, T., et al. (2018). *Numerical Solution of Differential Equations*. Cambridge University Press.

[Lin et al., 2006] Lin, F.-h., Belliveau, J. W., Dale, A. M., and Ha, M. S. (2006). Distributed Current Estimates Using Cortical Orientation Constraints. *Human Brain Mapping*, 27:1–13.

[Lin et al., 2017] Lin, Z., Zhang, Q., et al. (2017). High order finite volume solutions of the steady state advection diffusion equation with nonlinear Robin boundary conditions. *Journal of Computational Physics*, 345(May):358–372.

[Liu et al., 2005] Liu, J., Zhu, S., Yao, Y., Zhang, Z., and He, B. (2005). Finite element modeling of human head from MRI. *Conference proceedings : ... Annual International Conference of the IEEE Engineering in Medicine and Biology Society. IEEE Engineering in Medicine and Biology Society. Conference*, 3:2539–42.

[Liu et al., 2017] Liu, Q., Farahibozorg, S., Porcaro, C., Wenderoth, N., and Mantini, D. (2017). Detecting large-scale networks in the human brain using high-density electroencephalography. *Human Brain Mapping*, 4643(June):4631–4643.

[Liu et al., 2018] Liu, Q., Ganzetti, M., Wenderoth, N., and Mantini, D. (2018). Detecting Large-Scale Brain Networks Using EEG: Impact of Electrode Density, Head Modeling and Source Localization. *Frontiers in Neuroinformatics*, 12(March):1–11.

[López et al., 2014] López, J., Litvak, V., Espinosa, J., Friston, K., and Barnes, G. R. (2014). Algorithmic procedures for bayesian meg/eeg source reconstruction in spm. *NeuroImage*, 84:476–487.

[López et al., 2012] López, J., Penny, W. D., Espinosa, J., and Barnes, G. R. (2012). A general bayesian treatment for meg source reconstruction incorporating lead field uncertainty. *NeuroImage*, 60(2):1194–1204.

[Malmivuo et al., 1995] Malmivuo, J., Plonsey, R., et al. (1995). *Principles and applications of bioelectric and biomagnetic field*.

[Malony et al., 2011] Malony, A., Salman, A., Turovets, S., Tucker, D., Volkov, V., Li, K., Song, J., Biersdorff, S., Davey, C., Hoge, C., and Hammond, D. (2011). Computational modeling of human head electromagnetics for source localization of milliscale brain dynamics. 163:329–35.

[Marin et al., 1998] Marin, G., Guerin, C., Baillet, S., Garnero, L., and Meunier, G. (1998). Influence of skull anisotropy for the forward and inverse problem in eeg:

Simulation studies using fem on realistic head models. *Human Brain Mapping*, 6(4):250–269.

[Marino et al., 2016] Marino, M., Liu, Q., Brem, S., Wenderoth, N., Mantini, D., et al. (2016). Medical image registration Automated detection and labeling of high-density EEG electrodes from structural MR images. *Journal of Neural Engineering*, 13(5):056003.

[Martinez et al., 2017] Martinez, Vargas, J. D., Strobbe, G., Vonck, K., van Mierlo, P., and Castellanos, Dominguez, G. (2017). Improved localization of seizure onset zones using spatiotemporal constraints and time-varying source connectivity. *Frontiers in Neuroscience*, 11(APR).

[Martínez Vargas et al., 2016] Martínez Vargas, J. D., López, J. D., Baker, A., Castellanos-Dominguez, G., Woolrich, M. W., and Barnes, G. (2016). Non-linear parameter estimates from non-stationary meg data. *Frontiers in Neuroscience*, 10.

[Maxwell, 1873] Maxwell, J. C. (1873). *Summary for Policymakers*, volume 1.

[Meijs et al., 1989] Meijs, J. W. H., Weier, O. W., Peters, M. J., and van Oosterom, A. (1989). On the Numerical Accuracy of the Boundary Element Method. *IEEE TRANSACTIONS ON BIOMEDICAL ENGINEERING*, 36(October):1038–1049.

[Michel et al., 2012] Michel, C. M., Murray, M. M., et al. (2012). Towards the utilization of EEG as a brain imaging tool. *NeuroImage*, 61(2):371–385.

[Michel et al., 2004] Michel, C. M., Murray, M. M., Lantz, G., Gonzalez, S., Spinelli, L., and Grave De Peralta, R. (2004). EEG source imaging. *Clinical Neurophysiology*, 115(10):2195–2222.

[Michel et al., 2016] Michel, E., Hernandez, D., and Lee, S. Y. (2016). Electrical conductivity and permittivity maps of brain tissues derived from water content based on T1 -weighted acquisition. *Magnetic resonance in medicine*, 00:n/a–n/a.

[Mohr et al., 2003] Mohr, M., Vanrumste, B., et al. (2003). Comparing iterative solvers for linear systems associated with the finite difference discretisation of the forward problem in EEG source analysis. *Medical & biological engineering & computing*, 41:75–84.

[Montes et al., 2016] Montes, R. V., Hallez, H., Mierlo, P. V., and Staelens, S. (2016). Influence of skull modeling on EEG source localization : Inhomogeneities , geometry and noise sensitivity. *Brain Topography*, 1(27):95–111.

[Montes et al., 2013] Montes, V., van Mierlo, P., Strobbe, G., Staelens, S., Vandenberghe, S., and Hallez, H. (2013). Influence of Skull Modeling Approaches on EEG Source Localization. *Brain topography*.

[Nelder et al., 1965] Nelder, J. A., Mead, R., et al. (1965). A Simplex Method for Function Minimization. *The Computer Journal*, 7(4):308–313.

[Nicholson, 1965] Nicholson, P. W. (1965). Specific impedance of cerebral white matter. *Experimental Neurology*, 13(4):386–401.

[Oostenveld et al., 2011] Oostenveld, R., Fries, P., Maris, E., and Schoffelen, J. M. (2011). FieldTrip: Open source software for advanced analysis of MEG, EEG, and invasive electrophysiological data. *Computational Intelligence and Neuroscience*, 2011.

[Pai et al., 2005] Pai, D., Jiang, J., Hua, J., Duan, Y., Muzik, O., and Lu, S. (2005). Segmentation of Brain Structures Using PDE- Driven Surface Growing. In *Fuzzy Information Processing Society, 2005. NAFIPS 2005. Annual Meeting of the North American*, pages 424–428.

[Palagan et al., 2011] Palagan, C., ECE, R., Coll., E., Tirunelveli, and India Leena, T. (2011). Brain Structure Segmentation of Magnetic Resonance Imaging Using T Mixture Algorithm. *Electronics Computer Technology (ICECT), 2011 3rd International Conference on*, 3:446–450.

[Panizo et al., 1977] Panizo, M., Castellanos, A., and Rivas, J. (1977). Finite-difference operators in inhomogeneous anisotropic media. *Journal of Applied Physics*, 48(3):1054.

[Penny, 2012] Penny, W. D. (2012). Comparing dynamic causal models using AIC, BIC and free energy. *NeuroImage*, 59(1):319–330.

[Penny et al., 2004] Penny, W. D., Stephan, K. E., et al. (2004). Comparing dynamic causal models. *Neuroimage*, 22(3):1157–1172.

[Petersen et al., 2012] Petersen, K. B., Pedersen, M. S., et al. (2012). *The Matrix Cookbook*.

[Phillips et al., 2002] Phillips, C., Rugg, M. D., and Friston, K. J. (2002). Anatomically Informed Basis Functions for EEG Source Localization: Combining Functional and Anatomical Constraints. *NeuroImage*, 16(3):678–695.

[Plonsey, 1963] Plonsey, R. (1963). Reciprocity Applied to Volume Conductors and the ECG. *IRE Transactions on Bio-Medical Electronics*, 10(1):9–12.

[Pohlmeier et al., 1997] Pohlmeier, R., Buchner, H., Knou, G., Jcker, A. R., Beckmann, R., and Pesch, J. (1997). The Influence of Skull - Conductivity Misspecification on Inverse Source Localization in Realistically Shaped Finite Element Head Models. *Brain Topography*, 9(3):157–162.

[Rahmouni et al., 2017] Rahmouni, L., Mitharwal, R., and Andriulli, F. P. (2017). Two volume integral equations for the inhomogeneous and anisotropic forward problem in electroencephalography. *Journal of Computational Physics*, 348(July):732–743.

[Ramière et al., 2007] Ramière, I., Angot, P., and Belliard, M. (2007). A general fictitious domain method with immersed jumps and multilevel nested structured meshes. *Journal of Computational Physics*, 225(2):1347–1387.

[Ramon et al., 2006] Ramon, C., Haueisen, J., and Schimpf, P. H. (2006). Influence of head models on neuromagnetic fields and inverse source localizations. *Biomedical engineering online*, 5:55.

[Ramon et al., 2011] Ramon, C., Holmes, Mark, D., et al. (2011). Noninvasive Epileptic Seizure Localization from Stochastic Behavior of Short Duration Interictal High Density Scalp EEG Data. *Brain topography*.

[Rigoux et al., 2014] Rigoux, L., Stephan, K. E., Friston, K. J., and Daunizeau, J. (2014). Bayesian model selection for group studies - Revisited. *NeuroImage*, 84:971–985.

[Rush et al., 1968] Rush, S., Driscoll, D. A., et al. (1968). Current distribution in the brain from surface electrodes. *Anesthesia and Analgesia*, 47(6):717–723.

[Rush et al., 1969] Rush, S., Driscoll, D. A., et al. (1969). EEG electrode sensitivity - an application of reciprocity. *IEEE Transactions on Biomedical Engineering*, 16(1):15–22.

[Saleheen et al., 1997] Saleheen, H. I., Ng, K. T., et al. (1997). New Finite Difference Formulations for General Inhomogeneous Anisotropic Bioelectric Problems. *IEEE transactions on biomedical engineering*, 44(9):800–809.

[Saleheen et al., 1998] Saleheen, H. I., Ng, K. T., et al. (1998). A new three-dimensional finite-difference bidomain formulation for inhomogeneous anisotropic cardiac tissues. *IEEE transactions on biomedical engineering*, 45(1):15–25.

[Salman et al., 2013] Salman, A., Malony, A., Turovets, S., Volkov, V., Ozog, D., and Tucker, D. (2013). Next-generation human brain neuroimaging and the role of high-performance computing. *2013 International Conference on High Performance Computing & Simulation (HPCS)*, 1:234–242.

[Salman et al., 2016] Salman, A., Malony, A., Turovets, S., Volkov, V., Ozog, D., and Tucker, D. (2016). Concurrency in electrical neuroinformatics: Parallel computation for studying the volume conduction of brain electrical fields in human head tissues. *Concurrency Computation*, 28(7):2213–2236.

[Sarvas, 1987] Sarvas, J. (1987). Basic mathematical and electromagnetic concepts of the biomagnetic inverse problem. *Physics in medicine and biology*, 32(1):11–22.

[Schimpf et al., 2002] Schimpf, P. H., Ramon, C., and Haueisen, J. (2002). Dipole models for the EEG and MEG. *IEEE Transactions on Biomedical Engineering*, 49(5):409–418.

[Shackleton D et al., 2003] Shackleton D, P., Kasteleijn, D, G., and Craen A, J. (2003). Living with epilepsy: long-term prognosis and psychosocial outcomes. *Neurology*, pages 64–70.

[Stenroos et al., 2012] Stenroos, M., Sarvas, J., et al. (2012). Bioelectromagnetic forward problem: isolated source approach revis(it)ed. *Physics in medicine and biology*, 57(11):3517–35.

[Stephan et al., 2009] Stephan, K. E., Penny, W. D., Daunizeau, J., Moran, R. J., and Friston, K. J. (2009). Bayesian model selection for group studies. *NeuroImage*, 46(4):1004–1017.

[Stevenson et al., 2014] Stevenson, C., Brookes, M., López, J. D., Troebinger, L., Mattout, J., Penny, W., Morris, P., Hillebrand, A., Henson, R., and Barnes, G. (2014). Does function fit structure? A ground truth for non-invasive neuroimaging. *NeuroImage*, 94:89–95.

[Storti et al., 2012] Storti, S. F., Formaggio, E., Franchini, E., Bongiovanni, L. G., Cerini, R., Fiaschi, A., Michel, C. M., and Manganotti, P. (2012). A multimodal imaging approach to the evaluation of post-traumatic epilepsy. *Magnetic Resonance Materials in Physics, Biology and Medicine*, 25(5):345–360.

[Strobbe, 2015] Strobbe, G. (2015). *Advanced Forward Models for EEG Source Imaging*. PhD thesis.

[Strobbe et al., 2014a] Strobbe, G., van Mierlo, P., De Vos, M., Mijović, B., Hallez, H., Van Huffel, S., López, J. D., and Vandenberghe, S. (2014a). Bayesian model selection of template forward models for EEG source reconstruction. *NeuroImage*, 93 Pt 1:11–22.

[Strobbe et al., 2014b] Strobbe, G., van Mierlo, P., De Vos, M., Mijović, B., Hallez, H., Van Huffel, S., López, J. D., and Vandenberghe, S. (2014b). Multiple sparse volumetric priors for distributed EEG source reconstruction. *NeuroImage*, 100:715–24.

[Tadel et al., 2011] Tadel, F., Baillet, S., Mosher, J. C., Pantazis, D., and Leahy, R. M. (2011). Brainstorm: A user-friendly application for MEG/EEG analysis. *Computational Intelligence and Neuroscience*, 2011.

[Titto et al., 2004] Titto, M, A., Puthusserypady, S., et al. (2004). Embedding EEG data on 3D head modeled using MRI data. *Conference proceedings : ... Annual International Conference of the IEEE Engineering in Medicine and Biology Society. IEEE Engineering in Medicine and Biology Society. Conference*, 3:1833–7.

[Torrado et al., 2016] Torrado, Carvajal, A., Herraiz, J. L., Hernandez-Tamames, J. A., San Jose-Estepar, R., Eryaman, Y., Rozenholc, Y., Adalsteinsson, E., Wald, L. L., and Malpica, N. (2016). Multi-atlas and label fusion approach for patient-specific MRI based skull estimation. *Magnetic Resonance in Medicine*, 75(4):1797–1807.

[Torrado et al., 2014] Torrado, Carvajal, A. H.-T. J., Herraiz, J. L., Eryaman, Y., Turk, E. A., R, S. J. E., Rozenholc, Y., Adalsteinsson, E., Wald, L. L., and Malpica, N.

(2014). High-Field MRI Planing Patient-Specific Tissue Model Segmentation Skull Segmentation in MRI. In *ISMRM 2014*.

[Trans Cranial Technologies Ltd., 2012] Trans Cranial Technologies Ltd. (2012). 10 / 20 System Positioning Manual. Technical Report 1.

[Tuch et al., 2001] Tuch, D. S., Wedeen, V. J., Dale, a. M., George, J. S., Belliveau, J. W., et al. (2001). Conductivity tensor mapping of the human brain using diffusion tensor MRI. *Proceedings of the National Academy of Sciences of the United States of America*, 98(20):697–701.

[Turovets et al., 2014] Turovets, S., Volkov, V., Zherdetsky, A., Prakonina, A., and Malony, A. D. (2014). A 3D finite-difference BiCG iterative solver with the Fourier-Jacobi preconditioner for the anisotropic EIT/EEG forward problem. *Computational and mathematical methods in medicine*, 2014:426902.

[Vallagh et al., 2007] Vallagh, S., Clerc, M., et al. (2007). CONDUCTIVITY ESTIMATION FOR EEG : WHAT IS RELEVANT? In *Proceedings of NFSI & ICFBI*, pages 369–372.

[Van Hoey et al., 2000] Van Hoey, G., Vanrumste, B., D'Havé, M., Van De Walle, R., Lemahieu, I., Boon, P., et al. (2000). Influence of measurement noise and electrode mislocalisation on EEG dipole-source localisation. *Medical and Biological Engineering and Computing*, 38(3):287–296.

[Vanrumste et al., 1998] Vanrumste, B., Hoey, G. V., Boon, P., Havk, M. D., and Lemahieu, I. (1998). INVERSE CALCULATIONS IN EEG SOURCE ANALYSIS APPLYING THE FINITE DIFFERENCE METHOD , RECIPROCITY AND LEAD FIELDS. *Proceedings of the 20th Annual International Conference of the IEEE Engineering in Medicine and Biology Society*, 20(4):2112–2115.

[Vanrumste et al., 2001a] Vanrumste, B., Hoey, G. V., Walle, R. V. D., Boon, P., Lemahieu, I., Hese, P. V., Hav, M. D., Pintelaan, D., and Ghent, B. (2001a). THE REALISTIC VERSUS THE SPHERICAL HEAD MODEL IN EEG DIPOLE SOURCE ANALYSIS IN THE PRESENCE OF NOISE. In *Proceedings of the 23rd Annual EMBS International Conference*, pages 25–28.

[Vanrumste et al., 2000] Vanrumste, B., Van Hoey, G., Van de Walle, R., D'Havé, M., Lemahieu, I., and Boon, P. (2000). Dipole location errors in electroencephalogram

source analysis due to volume conductor model errors. *Medical & biological engineering & computing*, 38(5):528–34.

[Vanrumste et al., 2001b] Vanrumste, B., Van Hoey, G., Van de Walle, R., D'Havé, M. R., Lemahieu, I. a., and Boon, P. a. (2001b). The validation of the finite difference method and reciprocity for solving the inverse problem in EEG dipole source analysis. *Brain topography*, 14(2):83–92.

[Van't Ent et al., 2001] Van't Ent, D., De Munck, J. C., and Kaas, A. L. (2001). A fast method to derive realistic BEM models for E/MEG source reconstruction. *IEEE Transactions on Biomedical Engineering*, 48(12):1434–1443.

[Vatta et al., 2010] Vatta, F., Meneghini, F., Esposito, F., Mininel, S., and Di Salle, F. (2010). Realistic and spherical head modeling for EEG forward problem solution: A comparative cortex-based analysis. *Computational Intelligence and Neuroscience*, 2010.

[Voges et al., 2011] Voges, N., Blanchard, S., Wendling, F., Clerc, M., and Be, C. (2011). Modeling of the Neurovascular Coupling in Epileptic Discharges. *Brain Topography*, 25(2):136–156.

[Volkov et al., 2009] Volkov, V., Zherdetsky, A., Turovets, S., and Malony, A. (2009). A 3D Vector-Additive Iterative Solver for the Anisotropic Inhomogeneous Poisson Equation in the Forward EEG problem. *Springer-Verlag Berlin Heidelberg*, pages 511–520.

[Vorwerk et al., 2014] Vorwerk, J., Cho, J.-H., Rampp, S., Hamer, H., Knösche, T. R., and Wolters, C. H. (2014). A guideline for head volume conductor modeling in EEG and MEG. *NeuroImage*, 100:590–607.

[Vorwerk et al., 2018] Vorwerk, J., Oostenveld, R., Piastra, M. C., Magyari, L., and Wolters, C. H. (2018). The FieldTrip-SimBio pipeline for EEG forward solutions. *Biomedical engineering online*, 17(1):37.

[Waberski et al., 2000] Waberski, T. D., Gobbelé, R., Herrendorf, G., Steinhoff, B. J., Kolle, R., Fuchs, M., Paulus, W., and Buchner, H. (2000). Source reconstruction of mesial-temporal epileptiform activity: comparison of inverse techniques. *Epilepsia*, 41(12):1574–83.

[Wakeman et al., 2015] Wakeman, D. G., Henson, R. N., et al. (2015). A multi-subject, multi-modal human neuroimaging dataset. *Scientific Data*, 2:150001.

[Wang et al., 2008] Wang, P., Wang, H., et al. (2008). A Modified FCM Algorithm for MRI Brain Image Segmentation. *2008 International Seminar on Future BioMedical Information Engineering*, (3):26–29.

[Warfield et al., 2004] Warfield, S. K., Zou, K. H., and Wells, W. M. (2004). Simultaneous truth and performance level estimation (staple): an algorithm for the validation of image segmentation. *Medical Imaging, IEEE Transactions on*, 23(7):903–921.

[Wendel et al., 2009] Wendel, K., Väisänen, O., Malmivuo, J., Gencer, N. G., Vanrumste, B., Durka, P., Magjarević, R., Supek, S., Pascu, M. L., Fontenelle, H., and Grave de Peralta Menendez, R. (2009). EEG/MEG source imaging: methods, challenges, and open issues. *Computational intelligence and neuroscience*, 2009:656092.

[Westin et al., 1999] Westin, C.-F., Maier, S., and Khidhir, B. (1999). Image processing for diffusion tensor magnetic resonance imaging. *Int. Conf. on Medical Image Computing and Computer-assited Interventions*, pages 441–452.

[Whalen et al., 2008] Whalen, C., Maclin, E. L., Fabiani, M., and Gratton, G. (2008). Validation of a method for coregistering scalp recording locations with 3D structural MR images. *Human brain mapping*, 29(11):1288–301.

[Wipf et al., 2010] Wipf, D. P., Owen, J. P., et al. (2010). Robust bayesian estimation of the location, orientation, and time course of multiple correlated neural sources using meg. *NeuroImage*, 49(1):641–655.

[Wolters, 2003] Wolters, C. H. (2003). *Influence of Tissue Conductivity Inhomogeneity and Anisotropy on EEG/MEG based Source Localization in the Human Brain*. PhD thesis.

[Wolters et al., 2006] Wolters, C. H., Anwander, A., Tricoche, X., Weinstein, D., Koch, M. A., and Macleod, R. S. (2006). Influence of tissue conductivity anisotropy on EEG / MEG field and return current computation in a realistic head model : A simulation and visualization study using high-resolution finite element modeling. *NeuroImage*, 30:813 – 826.

[Wolters et al., 2007a] Wolters, C. H., Köstler, H., Möller, C., Härdtlein, J., and Anwander, A. (2007a). Numerical approaches for dipole modeling in finite element method based source analysis. *International Congress Series*, 1300:189–192.

[Wolters et al., 2007b] Wolters, C. H., Kostler, H., Moller, C., Hardtlein, J., Grasedyck, L., and Hackbusch, W. (2007b). Numerical Mathematics of the Subtraction Method for the Modeling of a Current Dipole in EEG Source Reconstruction Using Finite Element Head Models. 30(1):24–45.

[Wolters et al., 2002] Wolters, C. H., Kuhn, M., Anwander, A., and Reitzinger, S. (2002). A parallel algebraic multigrid solver for finite element method based source localization in the human brain. *Computing and Visualization in Science*, pages 165–177.

[Wolters et al., 2000] Wolters, C, H., Hartmann, U., Koch, M., Kruggel, F., Burkhardt, S., Basermann, A., , and J., D. T. (2000). NEW METHODS FOR IMPROVED AND ACCELERATED FE-VOLUME CONDUCTOR MODELLING IN EEG/MEG-SOURCE RECONSTRUCTION.

[Wtorek et al., 2005] Wtorek, J., Polin, A., et al. (2005). The Contribution of Blood-Flow-Induced Conductivity Changes to Measured Impedance. 52(1):41–49.

[Yazdani et al., 2015] Yazdani, S., Yusof, R., Karimian, A., Pashna, M., and Hematian, A. (2015). Image Segmentation Methods and Applications in MRI Brain Images. *IETE Technical Review*, 32(6):413–427.

[Ziegler et al., 2014] Ziegler, E., Chellappa, S. L., Gaggioni, G., Ly, J. Q., Vandewalle, G., André, E., Geuzaine, C., and Phillips, C. (2014). A finite-element reciprocity solution for EEG forward modeling with realistic individual head models. *NeuroImage*, 103:542–551.